TUDelft

A techno-economic calculation method for the implementation of an autonomous solar and storage system to electrify Vopak's storage terminals

C.J.W. Linck

A techno-economic calculation method for the implementation of an autonomous solar and storage system to electrify Vopak's storage terminals

by

C.J.W. Linck

to obtain the degree of Master of Science
at the Delft University of Technology,

Student number: 4452356
Project date: October 28, 2022
Thesis committee: Prof. dr. ir. A. van Wijk   TU Delft
                    Prof. dr. ir. Z. Lukszo   TU Delft
                    Dr. ir. R. Santbergen   TU Delft
                    Dr. ir. N. Li   TU Delft
                    Dr. W. van der Zon   Vopak

Preface

I started my academic career at the TU Delft with a bachelor's in Civil Engineering. However, when orientating for the choice of my master I discovered that I want to be part of the most significant change that our world needs to overcome: the energy transition. This inspired me to pursue the master, Sustainable Energy Technology, which, when looking back, was the best choice I could have made. Understanding the technical, economic and social dynamics that we as individuals, industries, countries and the world have to undertake is incredible. One key takeaway is that the solution will be a mix of energy sources and technologies. This made conducting my research over the last couple of months extra valuable, as it allowed me to understand one of many solutions.

The last eight months have been a very knowledgeable roller coaster. The endless hours of researching, (re)writing, conducting meetings, and discussing to all the ups and downs I encountered with programming, have resulted in a piece of work that I am very proud of. First and foremost, I would like to thank my supervisor, Ad van Wijk for guiding me in the right direction in times when I didn't know where and how to steer. Providing me with comforting feedback when necessary and insights into his work as a hydrogen expert (which had nothing to do with my topic but was very interesting). Secondly, I want to thank Rudi Santbergen and Zofia Lukszo for their expertise and guidance during my thesis. Thirdly, a special thanks to Na Li, for providing a clear framework for the sizing approach by asking thought-provoking questions about what I wanted to achieve in my research and for the additional guidance in structuring my thesis better.

Lastly, I am grateful to Vopak for supporting me during my research and providing me with all the tools necessary to complete my thesis. Especially, I want to thank the captain of the Vopak ship, Willem van der Zon, for his confidence in me and his endless guidance, knowledge, and structural feedback. Most of all, he made my time at Vopak an enjoyable and fun one. Furthermore, a big thank you to my colleagues of Global Operations, who made my time at Vopak very pleasant. A word of gratitude goes out to all my friends I have met during my academic career, which made it a fruitful one. Most importantly, I thank my family for their unconditional support throughout my studies.

C.J.W. Linck
Delft, October 2022

Abstract

Vopak has the vision to become climate neutral by 2050 (Scope 1 and 2 emissions). Currently, over 99% of its CO_2 emissions originate from storage terminal activities. Action must be taken to reduce these emissions by converting the current (fossil fuel-based) generation of electricity to sustainable energy. This study aims to research how we can develop a methodology to evaluate the cost-effectiveness of an autonomous solar and storage system to electrify Vopak's storage terminals? The objective of the method is to develop a system that is clean, reliable, autonomous, and payable (cheap). The selected autonomous system comprises a photovoltaic (PV) system, a battery energy storage system (BESS) and a hybrid inverter to satisfy the energy load of the storage terminal.

The developed method is a techno-economic model using three interlinked components. First, a PV model uses meteorological data and specific technical characteristics to simulate different PV systems. Second, based on the cost of different components of the PV system and BESS, a grid-search system selection method is used to determine the lowest-cost sizing of an autonomous PV and battery system. Third, the sizing of the system is used to calculate the levelized cost of solar plus storage (LCOSS).

The method is evaluated for three selected storage terminals located in different climates. The lowest cost developed system for Vopak Fujairah Horizon terminal (desert climate), which has a LCOSS of 0.33 [$/kWh]. For Vopak Terminal Laurenshaven (maritime climate), a LCOSS of 0.96 [$/kWh] is calculated. Vopak Panama (tropical climate) has a designed system with a LCOSS of 0.53 [$/kWh]. The calculated LCOSS shows that these autonomous systems are not cost-effective, as they are 3 to 14 times more expensive than average energy prices from the grid for the storage terminal locations. A sensitivity analysis of the system costs and the weighted average cost of capital shows that a 50% decrease in battery costs results in a 38% decrease in the LCOSS. Furthermore, a decrease of 2% of the WACC has the same effect as a total system cost reduction of 10%–15%. Ultimately, enabling the system to use its dumped energy by selling it to the grid shows the most significant reduction in the LCOSS.

This study clarifies that the cost-effectiveness of an autonomous PV and battery system strongly depends on the climate and seasonal variation of the location as it affects the energy yield of the PV-generating technology and the sizing of the system. Furthermore, the battery system costs are currently two to three times more expensive than a PV system; therefore, to size the lowest-cost system, the sizing strategy rather increases the (cheaper) PV system size to satisfy the load than install an additional battery. This results in oversized PV systems generating a large amount of unused energy. A solution is to enable the system to sell its unused electricity to the grid. An alternative solution would be to add a secondary "clean" energy source, such as a hydrogen generator, to combat these oversized systems and thus reduce the lifetime system costs.

Keywords Techno-economic model, sizing method, photovoltaic modelling, battery energy storage system, levelized cost of solar plus storage

Contents

Nomenclature

Abbreviations

Abbreviation	Definition
AADAT	Azimuth-altitude dual-axis tracker
AGM	absorbent glass mat
BESS	Battery energy storage system
BOS	Balance of system
CSP	Concentrated solar power
DHI	Diffused horizontal irradiance
DNI	Direct normal Irradiance
DOE	U.S. Department of Energy
GCR	Ground coverage ratio
GHI	Global horizontal irradiance
HTSAT	Horizontal tilted single-axis solar tracker
HSAT	Horizontal single-axis solar tracker
IAM	Incidence angle modifier
LCO	Lithium cobalt oxide
LFP	Lithium iron phosphate
LMO	Lithium manganese oxide
NMC	Lithium nickel manganese oxide
NREL	National renewable energy laboratory
POA	Plane-of-array
PV	Photovoltaic
RFB	Redox flow battery
SIB	Sodium-ion battery
SNL	Sandia National Laboratories
STC	Standard test conditions
TMY	Typical meteorological year
TRL	Technology readiness level
TTDAT	Tip-tilt dual-axis tracker
VHF	Vopak Horizon Fujairah
VRF	Vanadium redox flow
VRLA	Valve-regulated lead-acid
VTL	Vopak Terminal Laurenshaven
VTSAT	Vertical single-axis solar tracker
VSAT	Vertical single-axis solar tracker
WACC	Weighted average cost of capital

Symbols

Symbol	Definition	Unit
a	Empirically determined coefficients used to predict module back surface temperature	[-]
a_{lim}	Lower limit of the state of charge of the BESS	[-]
A_s	Sun's altitude	[°]
b	Empirically determined coefficients used to predict module back surface temperature	[-]
b_{lim}	Upper limit of the state of charge of the BESS	[-]
$CAPEX$	Capital expenditure	[$]
$CAPEX_{battery}$	Capital expenditure of the BESS	[$]
$CAPEX_{pv}$	Capital expenditure of the PV system	[$]
$CAPEX_{total}$	Capital expenditure of the PV system and BESS	[$]
C_{bat}	Battery cost of the BESS	[$]
$C_{decom,bat}$	Decommissioning cost of the BESS	[$]
$C_{decom,pv}$	Decommissioning cost of the PV system	[$]
$C_{decom,total}$	Decommissioning cost of the PV system and BESS	[$]
$Cost_{system}$	CAPEX and OPEX of PV system and BESS	[$]
C_{rep}	Replacement cost of the BESS	[$]
d	Minimum spacing between PV panels	[m]
E	Solar irradiance incident on module surface	[W/m^2]
E_o	Reference solar irradiance on module	[W/m^2]
$E_{max}^{battery}$	Maximum energy capacity of the battery	[MWh]
E_{dumped}	Energy dumped by the system	[MWh]
E_{excess}	Excess energy	[MWh]
E_{load}	Energy load of the storage terminal	[MWh]
E_{opt}	Optimal azimuth for a fixed-axis system	[°]
E_{pv}	Energy generated by the PV system	[MWh]
$E_{pv,used}$	Energy used by the combined PV and battery system	[MWh]
E_s	Sun's azimuth	[°]
F	Financial obligations of the PV system and BESS	[$]
G	Discounted energy sent to the grid	[MWh]
G_{DNI}	Direct normal irradiance	[W/m^2]
G_{DHI}	Diffused horizontal irradiance	[W/m^2]
G_{GHI}	Global orizontal irradiance	[W/m^2]
C_{grid}	Cost of using energy from the grid	[$]
l	Battery lifetime	[years]
$LCOSS$	Levelized cost of solar-plus-storage	[$/kWh]
L_{EW}	CHECK Distance between two solar panels	[m]
L_i	Individual system losses	[%]
L_{pv}	Length dimension of a PV panel	[m]
L_{total}	Total system losses	[%]
$OPEX$	Operational expenditure	[$]
$OPEX_{pv}$	Operational expenditure of the PV system	[$]
$OPEX_{battery}$	Operational expenditure of the BESS	[$]
$OPEX_{total}$	Operational expenditure of the PV system and BESS	[$]
P_{ac}	AC power output	[W]
$P_{battery}$	Power of the BESS	[MW]
P_{charge}	Power charged to the BESS	[W]
P_{dc}	DC power output	[W]
P_{dc0}	Nameplate rating	[W]
$P_{discharge}$	Power discharged from the BESS	[W]
P_{pv}	Power of the PV system	[MW]
r	Discount rate	[%]

Symbol	Definition	Unit
T_a	Ambient air temperature	[℃]
T_c	Cell temperature inside module	[℃]
T_m	Measured back-surface module temperature	[℃]
T_{ref}	Cell reference temperature under STC	[℃]
α	Cost factor to distinguish between different PV technologies	[-]
β	Scaling factor based on the PV size	[-]
γ	Temperature coefficient	[1/℃]
ΔT	Temperature difference between the cell and the module back surface at an irradiance level of 1000 W/m_2	[℃]
η_{EU}	EU weighted efficiency for an inverter	[%]
η_{pv}	Efficiency of the PV module	[%]
κ	Annual cost reduction of the battery	[%]
λ	Number of times the battery needs to be replaced	[-]
v_w	Wind speed measured at 10m height	[m/s]
φ	Normalisation factor of workers' wages for different countries	[-]
ω	Average yearly wage of a worker in a country	[$]
ω_c	Correction angle	[°]
ω_{ID}	Ideal tracking angle	[°]
ω_{IDC}	Corrected angle for back-tracking	[°]
w	Width dimension of a PV panel	[m]
ω_{opt}	Optimal surface tilt angle for a fixed-axis system	[°]

List of Figures

List of Tables

<div align="right">

1

</div>

<div align="right">

Introduction

</div>

1.1. Background information

Following the Paris Agreement, the Netherlands adopted the Climate Act in 2019, therefore the Netherlands must reduce its greenhouse gas (GHG) emission by 95% compared to 1990, to become climate neutral by 2050. Furthermore, the Netherlands has an interim target to reduce its emissions by 40% by 2030 compared to 1990. This impacts all industries, who therefore need to evaluate and plan their transition to a sustainable future. This will change the energy landscape in the coming decades.

Industrial emissions are categorized into three scopes. Scope 1 emissions are direct greenhouse gas (GHG) emissions from sources owned or controlled by the reporting entity. The GHG emissions from the generation of purchased electricity, steam, and heating/cooling are Scope 2 emissions because, as a user of the energy, the consuming party is responsible. Scope 3 emissions are those from sources not owned and not directly controlled by the reporting company. However, they are related to the company's activities.

Vopak, the world's leading independent tank storage company, is strongly driven by its "Energy Intensive Industry" customers, which predominantly produce high levels of CO_2 emissions. Vopak's emissions are Scope 3, so Vopak must contribute to the customer's reduction plans. Vopak's relationship with its clients is visually presented in Figure 1.1. Furthermore, carbon prices continue to increase, making it extremely costly for companies to operate as they do. Additionally, pressure from the "Milieudefensie" demands that the 30 largest CO_2 emitting companies of the Netherlands (which includes Vopak) develop a climate plan.

The above-mentioned developments, the Climate Act, Scope 3 emissions from its customers, rising carbon prices, and increasing pressure from environmental activists, have led Vopak to commit to a considerable emission reduction pathway. By 2030, Vopak wants to reduce its CO_2 emissions by at least 30% (vs 2021, Scope 1 and 2 emissions) and become climate neutral by 2050 (Scope 1 and 2). According to Willem van der Zon, environmental advisor of Vopak, over 99% of Vopak's Scope 1 and 2 emissions originate from storage terminal activities. This will influence Vopak's daily energy operations at its storage terminals.
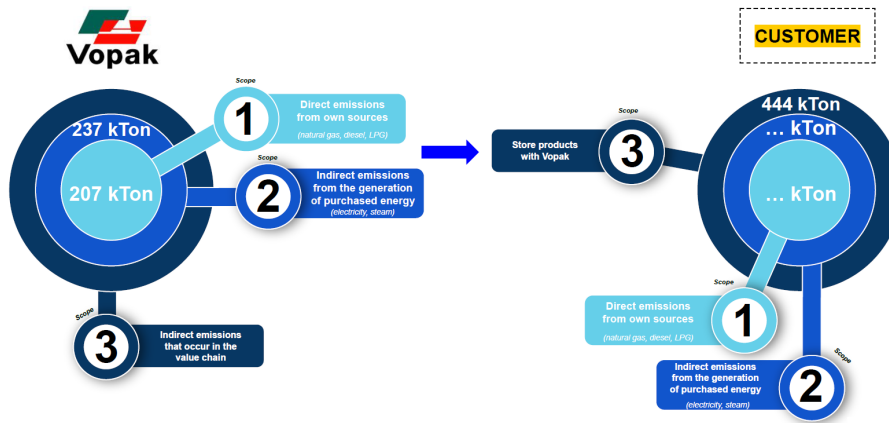
Figure 1.1: Visual representation of the relationship between Vopak
and its customers for scope 1, 2, 3 emissions (Vopak, 2022)

1.2. Vopak: Storage terminals

Vopak is a tank storage provider specializing in storing and handling bulk liquid chemicals, gases, and oil products. These products are stored at 79 strategic locations worldwide in storage terminals. A storage terminal is an industrial area with large tanks for holding liquid or gas. These terminals are often located near the coast, so ships and tankers can quickly (un)load their products. Figure 1.2 provides a photograph of one of Vopak's storage terminals. All these storage terminals have different energy demand characteristics due to the size of the terminal and the products they store. Some products must be constantly heated and others kept under a certain pressure. Furthermore, the storage business is extremely volatile because it is driven by the supply and demand of these products; therefore, the operating hours are extremely inconsistent. Additionally, some locations do not have the opportunity to take energy from the country's grid and must therefore generate their own energy.

Figure 1.2: Europoort, Vopak's largest storage terminal in the world (Vopak, 2022)

1.3. Research gap

Like Vopak, many companies are currently struggling to find cost-effective solutions to achieve their CO_2 ambitions. Furthermore, companies operating globally are in need of solutions which have the potential to be implemented at different locations worldwide. As mentioned above, most of Vopak's CO_2 emissions come from the storage terminals that Vopak operates globally. Currently fossil fuels power these storage terminals, producing high levels of CO_2. For these storage terminals to reduce its CO_2 emissions, there are different measures and solutions possible.

This study facilitates progress in this field by researching one possible solution: the implementation of an autonomous solar and storage system to power their storage terminals. For a solution to be

implemented, it is essential to understand the cost-effectiveness for a storage terminal. However, in literature research is often focused on cost-efficient systems but in the private-sector decisions are cost-driven with efficiency as a secondary objective. Furthermore, limited research provides transparency into system possibilities, e.g. if a more efficient system is desired by the government, what sizing needs to be realized. Therefore, a method is needed that provides insight into the cost-effectiveness of an autonomous solar and storage system.

1.4. Solar and storage systems

This study explored two types of solar and storage systems: concentrated solar power (CSP) and a PV and battery energy storage system. Ultimately, based on the literature, concentrated solar power is not considered in the continuation of this research because only a select few storage terminals can meet the system requirements. For CSP to be cost-effective, the system needs a large area to harness the significant amounts of solar energy for storage. Furthermore, CSP must be implemented on a large scale (100 MW or more) to be competitive with a PV and battery system. Additionally, according to Müller-Steinhagen and Trieb (2004), for CSP to be economically viable at a location, it requires a minimum direct normal irradiance (DNI) of 1,800 $[KWh/m^2/year]$ according to Müller-Steinhagen and Trieb (2004). An analysis of the different elements of CSP, the main technical challenges, and a comparison of the different CSP systems are presented in Appendix A.1. However, a PV system and battery energy storage system (BESS) is not restricted by such constraints and can be implemented as a solar and storage system. Therefore, the remainder of this study focuses on PV systems and BESSs.

1.5. Aim and research questions

To understand the cost-effectiveness of implementing a PV and battery energy storage system to power its storage terminals, a techno-economic model is developed. This study aims to develop a flexible and transparent method which calculates the solar energy generated for different photovoltaic (PV) systems and uses a flexible sizing approach to size a PV and battery energy storage system based on the lowest system cost. To compare similar systems an economic analysis is conducted. The method is verified by studying three storage terminals, one in Fujairah (UAE), the other in Laurenshaven (Netherlands) and one in Panama. Hence the main research question is:

What is a methodology that can evaluate the cost-effectiveness of an autonomous PV and battery energy storage system to electrify Vopak's storage terminals?

The following sub-questions are addressed consecutively to understand whether a solar and storage system is technically capable and cost-effective to electrify Vopak's storage terminals.

- How can a flexible sizing approach be developed for an autonomous PV and battery system?
- How is the economics of an autonomous PV and battery system influenced by the costs and the weighted average cost of capital?
- To what extent is an autonomous PV and battery system economically viable for a storage terminal in the United Arab Emirates, the Netherlands, and Panama?

1.6. Structure

The study has the following structure. Chapter 2 explains the proposed system based on selected technologies from the literature and describes the designed techno-economic model (TEM). Subsequently, Chapter 3 describes the three selected locations used for the case study. Chapter 4 provides an analysis of the results from the model for these three locations. A discussion of these results, the methodology, and the models are provided in Chapter 5. Finally, in Chapter 6 a conclusion and recommendations about this study is given. Appendix A evaluates different PV and storage technologies from the literature. Appendix B provides the assumed inputs and data for the model (per location). The output from the models is presented in Appendix C.

2

Methodology

This chapter describes the methodology developed to evaluate the cost-effectiveness of implementing a PV system and BESS. Section 2.1 describes the proposed system. Subsequently, an overview of existing TEMs is given and the proposed TEM of this study is explained in Section 2.2. Section 2.3 explains the PV model. The different cost components of the system required for the system sizing are described in Section 2.4. The approach applied to size the system is shown in Section 2.5. Finally, Section 2.6 describes the calculation of the levelized cost of solar plus storage (LCOSS). The assumed data (e.g. assumptions for the PV model) and other relevant parameters used for the models are provided in Appendix B.

2.1. System description

The system comprises four main components: (1) the PV system, (2) the BESS, (3) the inverter, and (4) the load of the storage terminal. This system is not integrated with the grid and is therefore autonomous.

Firstly, the PV system is used to absorb solar energy and convert it to electricity. Different types of PV technologies are available. Appendix A.2 reviews the different PV technologies based on the literature. This review explores the economic and technical characteristics of different cell materials, analyzes the influence of using a monofacial or bifacial module, and researches the available PV tracking systems. Based on this study, the following PV technologies are selected as options in the PV system. Both monocrystalline and polycrystalline cell materials are analyzed as system options. These cell materials are (relatively) cheap, extremely mature, and have been widely implemented. Bifacial modules are being implemented increasingly often, and a significant market share of 35% is predicted by 2030 (Metz et al., 2017a). Therefore, a comparison between a monofacial and bifacial PV system is included as an option in the PV system. Many different tracking systems are available. The PV system simulates two types of tracking systems: a fixed-axis system and a horizontal single-axis tracker (HSAT) system. This is because the fixed-axis system is the most used with a standard PV system configuration. A single-axis tracker system is also added as a tracking option because the additional energy gain can be extremely beneficial despite the additional cost. The HSAT system is selected as the single-axis tracker type due to its simple construction, and it is the most cost-effective single-axis tracker (Weimar, 2020). The HSAT uses a mechanical tracking system that tracks the Sun from east to west throughout the day by rotating around one axis parallel to the ground. A dual-axis tracker was not added as a system option because it has a significantly higher additional cost and is only effective at high latitudes.

Secondly, a BESS is used to store excess energy and provide energy when insufficient solar energy is available to satisfy the load, for example, during the night or the winter. Different types of BESS are available; these are investigated and compared based on specific criteria: technology readiness level (TRL), large-scale industrial applicability, and costs. The research and analysis are provided in Appendix A.3. A final selection comprised two types of BESSs to use in the system because these batteries satisfy other important criteria as well: the future cost perspective, environmental aspects such as toxicity, and the technical combination of a (relatively) long cycle life and storage duration. The

selected batteries are a vanadium-vanadium redox flow (VRF) and a Li-ion battery, with storage durations of 4 and 8 hours. These batteries were chosen because they are both extremely technologically mature; therefore, considerable (cost) data is available, which is helpful for the analysis. These two batteries also offer insight into two different battery technologies (redox flow and electrochemical). The literature frequently uses battery systems with storage durations of 4 and 8 hours to present the impact of increasing a battery's energy-to-power ratio. Therefore, the system also uses this storage duration as input for the batteries. Figure 2.1 presents an overview of the different technology configurations for the PV and BESS.
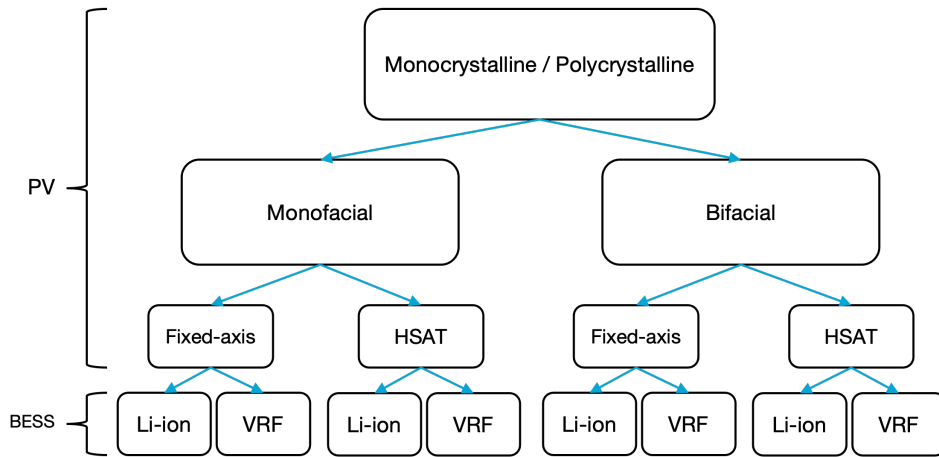
Figure 2.1: Overview of the selected PV and battery technologies for the system

Thirdly, an inverter is needed so that the electrical energy generated by the PV system and the BESS satisfies the load. For this system, it is assumed that the storage terminals operate using a hybrid inverter that can manage direct PV conversion and charging/discharging of the BESS. A hybrid inverter is selected because it is a cost-effective and efficient choice, ensuring high efficiency and requiring no installation of an additional battery inverter or charger (Schopfer et al., 2018).

Fourthly, an important aspect of the system is the energy load of the storage terminal. The energy load is the energy used to operate the storage terminals. Most of the daily energy demand is needed for pumping activities involving liquid and gas products. Figure 2.2 shows the configuration of the proposed autonomous system.
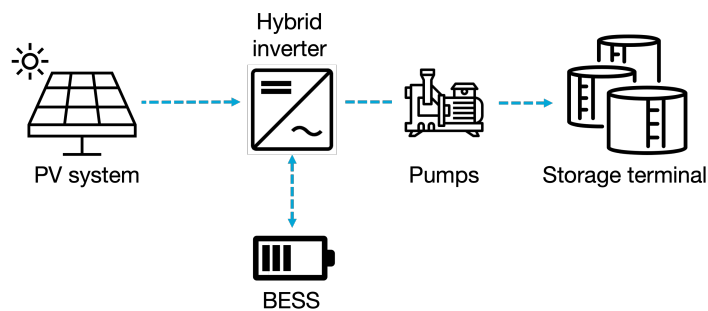
Figure 2.2: Overview of the proposed system

2.2. Techno-economic model

Different approaches are available to develop the proposed system. Section 2.2.1 provides a review of existing TEMs based on the literature. Subsequently, the proposed TEM for this study is described in Section 2.2.2.

2.2.1. Existing techno-economic models

Previous studies show that existing TEMs can be categorized into optimization and simulation models, depending on whether the PV and battery system capacity are optimization variables or simulated as fixed parameters (Han et al., 2022). The three main aspects of the TEM are reviewed: (1) different calculation techniques for a PV system, (2) sizing approaches, and (3) methods used for an economic analysis.

Several methods are available to model different PV systems. A previous study (Kolhe, 2009) used a complete analytical methodology to calculate solar radiation on a tilted PV array. Several studies use software such as PVGIS, PVsyst, and PVcase to calculate the energy output of a PV system. Fiedler and Matas (2022) used HOMER Grid software, which enabled detailed modelling, including all relevant boundary conditions for holiday homes in Sweden. Another study was conducted by (Nkuriyingoma et al., 2022), which selected PV*SOL as software, which performs simulations and calculates the accrued cash flow of the system. Research conducted by Bandyopadhyay et al. (2020) used MATLAB to model the irradiance for different tilted angles.

Different methods are used to determine the sizing of the PV system and BESS. Simplified rule-of-thumb methods are often used for smaller systems, such as that by Smets et al. (2016). An alternative method is using optimization techniques. A study by Taslimi et al. (2021) used mixed-integer linear programming (MILP) for two objective functions comprising total cost and loss of power supply probability (LPSP), which aimed to determine the optimal model and size of the PV modules. A multi-objective optimization was also used by Bandyopadhyay et al. (2020). A recent study (Kosmadakis et al., 2019) sized the system based on the probability of the system output due to meteorological variations.

For the TEM, different economic analyses of the system can be conducted. Based on the literature, the most common are as follows: net present value (NPV), which provides insight into the present value of cash inflows and outflows in a period, the internal rate of return (IRR), which is calculated to make NPV zero and used to estimate the profitability of an investment, investment cost, cost needed to launch the project, and the levelized cost of energy (LCOE), a measure of the average cost of electricity generation over a period.

The following can be concluded from the different methods. Firstly, it is useful to use programming as a simulation technique to understand different PV technologies and receive an estimate of their energy outputs for a specific location. Programming offers a practical approach to fully understand the operation of specific PV system component. Secondly, despite MILP showing extremely accurate results for sizing a system, it is complicated to understand due to the minimal transparency of the configuration options. The designed sizing approach must add transparency and accuracy so that the storage terminal operator can understand the possibilities. Finally, LCOE is the preferred choice due to its widespread adoption; therefore, the results can be easily compared with those in the literature (Aldersey-Williams & Rubert, 2019). Furthermore, it enables the comparison of different lifetime system costs. These factors are considered for the proposed model, as explained in Section 2.2.2.

2.2.2. Proposed techno-economic model

The proposed TEM calculates the energy output for different PV technologies, sizes a PV and battery system, and conducts an economic analysis. In this study, this techno-economic model is called the Linck model. The model is designed to be practical and user-friendly. A person with no engineering background can use the model if the necessary parameters are provided. The model's calculation output provides an estimate of the system's reality. The model is designed to be universal, meaning that it can be used for any location worldwide. The goal of the system is to be CRAP:

Clean - The system does not produce CO_2 during power generation.
Reliable - The system always satisfies the load of the storage terminal.
Autonomous - The system does not need grid exchange to satisfy the load.
Payable - The system is the lowest-cost option available.

The Linck model comprises three sub-models. The first sub-model is the PV model, which simulates different types of PV systems. This is necessary to understand how much energy a particular PV system produces every hour at a specific location. This model uses "Python" (2021) because this provides a set of functions for simulating the performance of complex PV energy system components. The second model is a sizing model, which uses the energy output data from the PV model and the corresponding total system costs of a PV and BESS to size the system based on the lowest cost. Conversely, literature which uses MILP shows highly accurate results but is often complicated to understand for non-engineers. This model uses a transparent and flexible sizing approach based on a grid-search system selection method. Finally, the output from the sizing model determines the LCOSS. This is the same as the LCOE, as previously mentioned, but emphasizes that the LCOE comprises the combined solar and storage system. Figure 2.3 shows a simple overview of the Linck model.

Photovoltaic model

Output:
8 different AC PV power outputs

[MWh/MW$_p$]

Sizing model

Output:
PV system size (P$_{pv}$)
[MW]

BESS size (P$_{battery}$)
[MWh]

LCOSS

Output:
LCOSS

[$kWh]
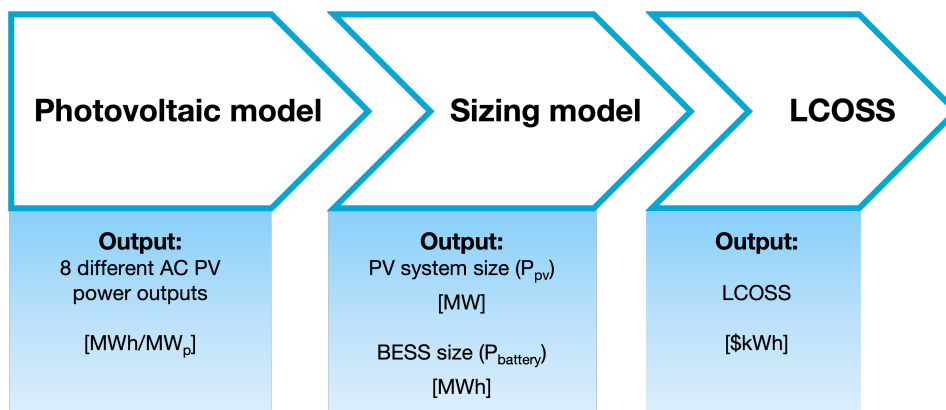
Figure 2.3: Overview of the Linck model

2.3. Photovoltaic model

As explained in Section 2.2.2, the first part of the Linck model is the PV model. The PV model is used to calculate the power output of different PV systems. As mentioned in Section 2.1, this model simulates a fixed-axis and a HSAT system with a monofacial or bifacial module and a monocrystalline or polycrystalline cell material. The eight different types of PV system are listed below:

- Monocrystalline – monofacial – fixed-axis
- Monocrystalline – bifacial – fixed-axis
- Monocrystalline – monofacial – HSAT
- Monocrystalline – bifacial – HSAT
- Polycrystalline – monofacial – fixed-axis
- Polycrystalline – bifacial – fixed-axis
- Polycrystalline – monofacial – HSAT
- Polycrystalline – bifacial – HSAT

Figure 2.4 presents a flowchart explaining the steps involved in calculating the AC power output of the different PV systems. The PV model uses location and meteorological data, PV panel data, and predetermined PV system design parameters as inputs; these inputs are presented on the left side of the figure. The calculation of the PV system is realized in six chronological steps for both a fixed-axis and a HSAT system; this is summarized below and shown in the figure. The six steps are further explained in detail in Sections 2.3.1 to 2.3.6.

1. Extract location and meteorological data
2. Calculate the optimal surface tilt and surface azimuth of the fixed-axis and HSAT system
3. Calculate the irradiance (monofacial and bifacial) on the module of the different PV systems
4. Calculate the operating temperature of the PV cells of the different PV systems
5. Calculate the DC power output of the different PV systems
6. Calculate the AC power output including system and inverter losses of the different PV systems
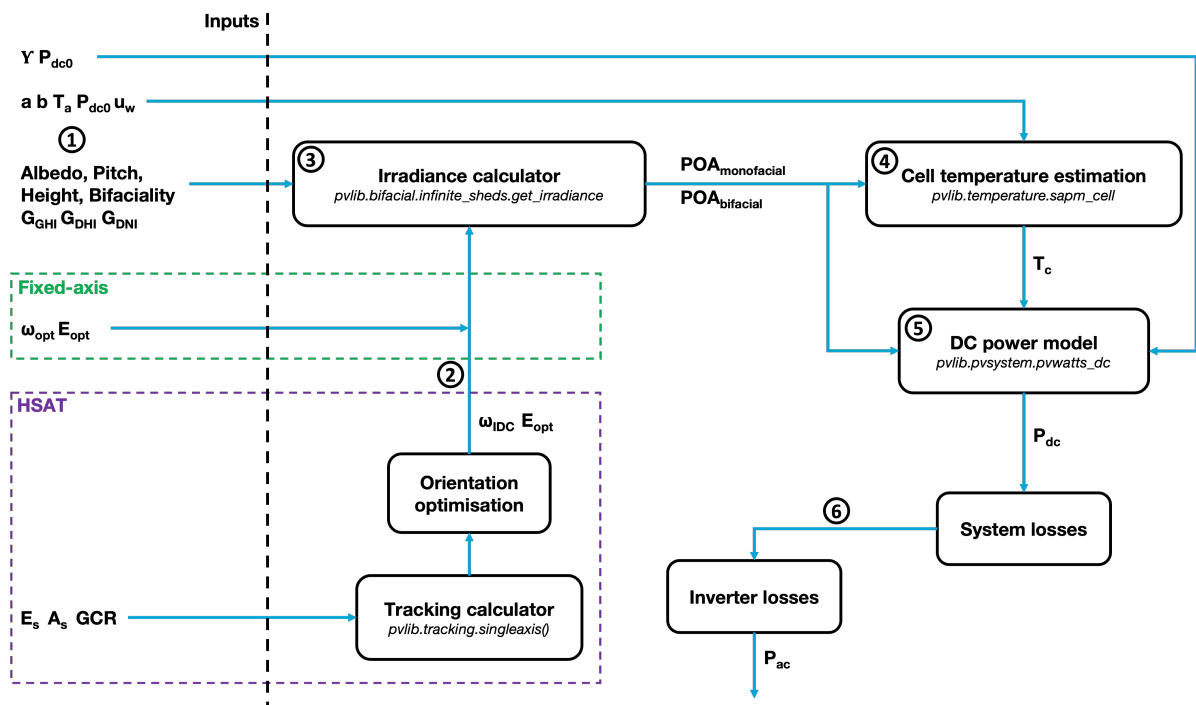
Figure 2.4: Flowchart explaining the steps involved in calculating the AC power output of a PV module; left are the different inputs, and the numbers 1 to 6 present the chronological calculation steps of the PV model

The model uses "Python" (2021) version 3.9.7. Most of the PV components are modelled using the *pvlib* Python package (Holmgren et al., 2018). This Python package is a community-supported open-source tool providing functions and classes for modelling solar PV energy systems.

2.3.1. Location and meteorological data
Meteonorm (2014) provides hourly resolution of meteorological data for a certain location. Meteonorm uses monthly values (station, imported, and interpolated data) to calculate hourly or per-minute values of a "typical meteorological year" (TMY) based on a stochastic model. For temperature, humidity, wind speed, and precipitation, it uses the periods 1961–1990, 2000–2009, and 1991–2010 for solar radiation. The location coordinates in terms of latitude and longitude are used to determine the Sun's position throughout the year. The model uses two main parameters indicating the Sun's position, the azimuth (E_s), and altitude (A_s). The main meteorological inputs used in this PV model are as follows: (a) ambient temperature (T_a), (b) wind speed (v_w), (c) DNI (G_{DNI}), (d) Diffused Horizontal Irradiance (G_{DHI}), (e) Global Horizontal Irradiance (G_{GHI}).

2.3.2. Optimal surface tilt and surface azimuth
The PV systems are modelled for locations in the northern hemisphere; therefore, the systems are all north-south orientated, facing south. The optimal surface tilt (ω_{opt}) and surface azimuth (E_{opt}) values for a fixed-axis system are received from "PVGIS" (2022) for a certain location. For a HSAT, the optimal surface tilt and azimuth change accordingly when tracking the Sun. However, when multiple trackers are placed in a limited area, the problem of mutual shading arises. Shade reduces the electric power output and increases the risk of hot spots (Lorenzo et al., 2011). Hence, the back-tracking strategy is implemented. This comprises moving the surface angles away from the ideal values (when all the receiver surfaces are perpendicular to the Sun), just enough for the shadow borderline to pass outside the border of the neighbouring tracker. Figure 2.5 shows the difference between ideal tracking for shadowing and when back-tracking is implemented. The influence of back-tracking on the tilt angle of the PV panel is shown with the correction angle, ω_c. This is calculated using Equations 2.1 and 2.2, where ω_{ID} is the ideal tracking angle and ω_{IDC} is the corrected angle for back-tracking. As shown, when back-tracking is implemented, a smaller tilt angle is used to ensure that one panel does not form shadows on the other. The necessity of back-tracking is influenced by the spacing between the PV trackers. The chosen spacing is presented as the ratio of the PV array area to the total ground area, called the ground coverage ratio (GCR), shown in Eq. 2.3. Specifically, this is the ratio of the total width of the PV installation to the distance between two PV panels (L_{EW}). The calculation method to determine L_{EW} is explained in Section 2.4.1.

$$\omega_{\text{C}} = \omega_{\text{ID}} - \omega_{\text{IDC}} \tag{2.1}$$

$$\cos \omega_{\text{C}} = L_{\text{EW}} \cos \omega_{\text{ID}} \tag{2.2}$$

$$\text{GCR} = \frac{1}{L_{\text{EW}}} \tag{2.3}$$

(a) Ideal tracking for shadowing **(b)** Back-tracking
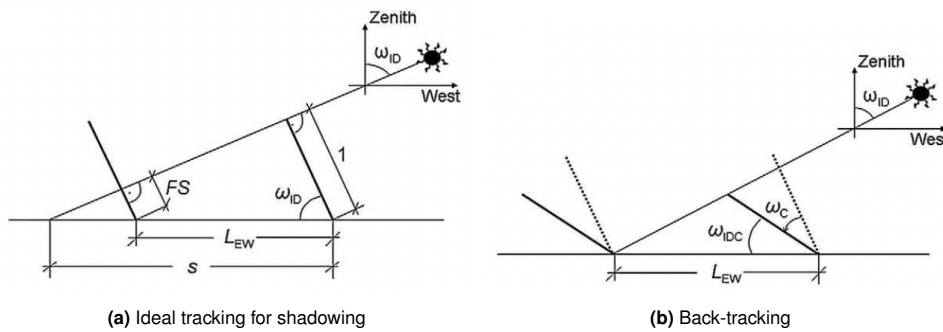
Figure 2.5: The difference between ideal tracking and back-tracking of a horizontal single-axis tracking system; the difference is shown with the correction angle, ω_c (Lorenzo et al., 2011)

Implementing the $pvlib.tracking.singleaxis$ function determines the rotational angle of a single-axis tracker when given the solar zenith and azimuth angle at a specific time instant. Based on the calculation method from Lorenzo et al. (2011) and additional information about the GCR, the maximum rotation angle of the tracker, and the axis tilt (the slope of the PV system is assumed flat), the function calculates the optimal angle of the tracker, ω_{IDC}, every hour. Figure 2.6 visualizes the ω_{IDC}, angle of incidence (AOI), surface tilt angle, and Sun altitude angle during a day. During the day, ω_{IDC} follows the Sun from east to west. Therefore, positive angles are anti-clockwise and negative clockwise. The AOI is the angle between the normal of the PV module surface and the vector of the incoming radiation. When the tracking system is active, the AOI strongly decreases and remains minimal, indicating that the tracker is tracking the Sun during Sun hours. The AOI is not zero due to the use of back-tracking. The Sun's altitude indicates where the Sun is during the day. The surface tilt is the time series output of this tracking model, used to calculate the irradiance for a tracking system, as explained in Section 2.3.3.
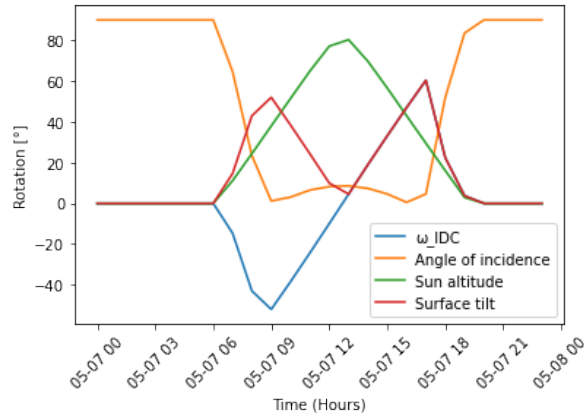
Figure 2.6: The optimal rotational angle with back-tracking (ω_{IDC}), the Sun's altitude, the angle-of-incidence and the surface tilt for a HSAT system with back-tracking

2.3.3. Monofacial and bifacial irradiance

The monofacial and bifacial irradiance needs to be calculated for the different PV systems. The irradiance of a module is affected by many uncertainties, such as conversion efficiency, reflection from the ground, and shade cast by module framing and system structures, causing an electrical mismatch. Modelling of a monofacial and bifacial PV module is similar but with the additional step of calculating the back-side irradiance. The bifacial irradiance is given by the front irradiance (POA_{front}) and back irradiance (POA_{back}) with bifaciality factor B, as shown by Eq. 2.4. Factors k_{shade} and $k_{transmit}$ account for losses due to shading and transmission around and through the module. For monofacial irradiance, only the POA_{front} is used.

$$POA_{\text{Bifacial}} = POA_{\text{front}} + POA_{\text{back}}B\left(1 + K_{\text{shade}}\right)\left(1 + K_{\text{transmit}}\right) \tag{2.4}$$

The infinite sheds irradiance model is used to model the PV panels' plane-of-array (POA) irradiance. The PV model exploits the function $pvlib.bifacial.infinite\_sheds.get\_irradiance$. It assumes that the PV system comprises parallel, evenly spaced rows on a level, horizontal surface. The model calculates irradiance at a location from the ends of any rows, thus assuming the rows are infinitely long. Furthermore, the model assumes diffuse irradiance from the sky is isotropic and that module surfaces do not allow irradiance to transmit through the module to the ground through gaps between cells. The model accounts for the following effects:

- Restricted view of the sky and ground from module surfaces due to nearby rows
- Restricted view of the sky from the ground due to nearby rows
- Shading of module surfaces by nearby rows
- Shading of back cells of a module by mounting structure and by module features

The front and back surfaces comprise direct irradiance with an incidence angle modifier (IAM) and diffuse irradiance, as shown in Eq. 2.5. The IAM is implemented to account for the optical losses if the solar AOI on the array surface exceeds zero. The diffuse component of the irradiance comprises sky and ground reflection (Eq 2.6).

$$POA_{\text{front, back row}} = POA_{\text{direct,row}} IAM + POA_{\text{diffuse,row}} \tag{2.5}$$

$$POA_{\text{diffuse, row}} = POA_{sky,row} + POA_{gnd,row} \tag{2.6}$$

To calculate the direct and diffuse components, the model identifies and calculates the shadows projected in row-to-row dimensions by the PV array using the PV array dimensions, orientation, and Sun's position (Marion et al., 2017). Therefore, the model needs specific PV system design inputs: the height of the centre point of the row above the ground, the distance between rows (pitch), the GCR, and the ground albedo. The dimensions are divided into n segments to identify whether the segment is shaded or unshaded. The model assumes no direct irradiance occurs in the shaded fraction. The diffuse component is calculated using the Perez et al. (1987) diffuse irradiance model for tilted surfaces and the view factor for both the sky and ground. The view factor of the sky from the ground was estimated using the zero-height rack configuration because no effect was observed when varying the rack height (with the width of the Sun neglected). The view factors from the sky and ground on the PV surfaces use linear approximations and weighted averages to consider the effect of nearby rows (A. Mikofski et al., 2019). For a further description of the calculation method, see the paper "Bifacial Performance Modeling in Large Arrays", written by A. Mikofski et al. (2019).

The $POA_{back,row}$ is calculated by treating it as a surface tilted by the addition of the front surface, the azimuth is rotated 180° around the zenith from the front surface. For example, the front surface is tilted by 30° with an azimuth of 270°; this means that the back surface is tilted at 150° with an azimuth of 90°. Finally, the optimal surface tilt and surface azimuth values for fixed and HSAT systems (2.3.2) are necessary to calculate the POA. The POA difference between monofacial and bifacial modules using a fixed-tilt and single-axis horizontal tracker in Fujairah, UAE, is presented in Figure 2.7. When comparing the POA of the HSAT and fixed systems, a higher POA is measured when the Sun is low (early morning/end of the day) because the tracker can change the tilt angle. Evidently, the difference between monofacial and bifacial is shown with the higher POA measured during sunlight hours because the additional irradiance can be absorbed by the back side of the system.
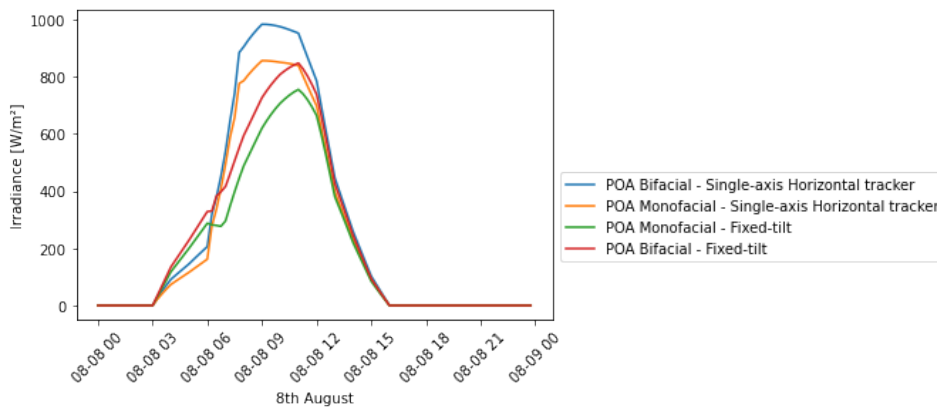
Figure 2.7: POA for Monofacial/Bifacial - Fixed/HSAT in Fujairah, UAE

2.3.4. Thermal model

A thermal model is required to estimate the PV module operating temperature to predict the annual solar energy production. An empirically based model was developed by King et al. (2004) from Sandia National Laboratories (SNL), which is still used today. This is described in Eq. 2.7. According to King et al. (2004), the model is adaptable and adequate for system engineering and design purposes. It has an operating accuracy of approximately 5 °C, resulting in uncertainties of this magnitude having less

than a 3% effect on the power output from the module. It uses local environmental conditions: irradiance, ambient temperature, wind speed, and two empirically determined coefficients (a, b). These were determined using thousands of temperatures recorded over several days with the module operating near thermal equilibrium. The coefficients are determined by the mounting configuration, the module construction, location, and height where wind speed is measured (King et al., 2004). The wind direction is not incorporated in the empirically based model due to the unnecessary complexity, which tends to average annually. In this PV model, the module type "Glass/cell/glass" with "Open rack" mount is modelled, thus a = -3.47, b = 0.0594 with ΔT = 3 °C. The coefficients for different PV configurations are provided in Appendix B.2.

$$T_m = E \cdot \left\{ e^{a+b \cdot v_w} \right\} + T_a, \tag{2.7}$$

where
$T_m =$ Back-surface module temperature $(°\mathrm{C})$,
$T_a =$ Ambient air temperature $(°\mathrm{C})$,
$E =$ Solar irradiance incident on module surface $\left(\mathrm{W/m^2}\right)$,
$v_w =$ Wind speed measured at standard 10m height $(\mathrm{m/s})$,
$a =$ Empirically-determined coefficient establishing the upper limit for module temperature
  at low wind speeds and high solar irradiance,
$b =$ Empirically-determined coefficient establishing the rate at which module temperature,
  drops as wind speed increases.

The cell temperature inside the module is related to the module back-surface temperature through a relationship provided in Eq. 2.8. It assumes one-dimensional thermal heat conduction through the module materials behind the cell. The cell temperature is calculated using the measured back-surface temperature of the module and the predetermined temperature difference between the back surface and the cell.

$$T_c = T_m + \frac{E}{E_o} \cdot \Delta T, \tag{2.8}$$

where
$T_m =$ Measured back-surface module temperature $(°\mathrm{C})$,
$T_c =$ Cell temperature inside module $(°\mathrm{C})$,
$E =$ Solar irradiance incident on module surface $\left(\mathrm{W/m^2}\right)$,
$E_o =$ Reference solar irradiance on module $\left(1000 \ \mathrm{W/m^2}\right)$,
$\Delta T =$ Temperature difference between the cell and the module back surface at an
  irradiance level of $1000 \ \mathrm{W/m^2}$.

Figure 2.8 shows the effect of solar irradiance on the cell temperature for this model. This indicates that the cell temperature is significantly higher during the daytime when the module produces power than at night time. This is logical because a PV module typically converts 20% of the light to electricity, and the rest causes the module temperature to increase.
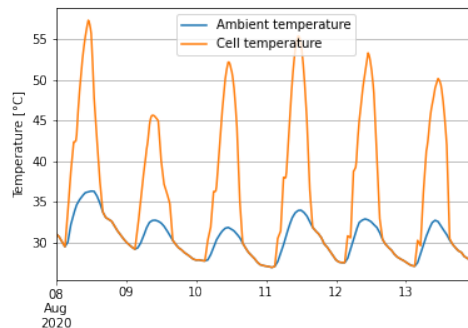
Figure 2.8: Cell temperature and ambient temperature of a monofacial fixed-axis PV panel in Fujairah, UAE

2.3.5. DC Power array

The relationship from A. P. Dobos (2014) is used, as shown in Eq. 2.10, to compute the DC power array. One goal of this analysis is to distinguish between different types of PV modules: monofacial vs bifacial and monocrystalline vs polycrystalline. This model uses four different PV modules from the manufacturer, Canadian Solar. For this analysis, a rated power (P_{rated}) of 400 [W] is chosen for all PV modules. Thus, P_{dc0} is needed for Eq. 2.10 to distinguish between the different PV panels and their corresponding nameplate rating. The module dimensions are normalized based on the PV panel dimensions according to the relationship shown in Eq. 2.9.

$$P_{dc0} = \frac{\eta_{pv}}{100} E_o L_{pv} W_{pv}, \tag{2.9}$$

where
η_{pv} = Efficiency of the PV module (%),
L_{pv} = The length dimension of a monofacial mono-crystalline PV panel (m),
W_{pv} = The width dimension of a monofacial mono-crystalline PV panel (m).

$$P_{dc} = \frac{E}{1000} P_{dc0}(1 + \gamma(T_{cell} - T_{ref})), \tag{2.10}$$

where
E = Solar irradiance incident on module surface $\left(\mathrm{W/m^2}\right)$,
T_c = Cell temperature inside module $(°\mathrm{C})$,
T_{ref} = Cell reference temperature, under standard test conditions (STC), which is 25 °C,
P_{dc0} = Nameplate DC rating (W),
γ = The temperature coefficient $(1/C)$.

2.3.6. System and inverter losses

There are two losses that need to be taken into account. Firstly, the system losses that have not explicitly been modelled are considered as percentages of the DC power. The individual losses (L_i) differ between locations. Appendix B.3 presents these values per location. The total system losses (L_{total}) are calculated using Eq. 2.11.

$$L_{total}(\%) = 100 \left[1 - \prod_i \left(1 - \frac{L_i}{100} \right) \right] \tag{2.11}$$

Secondly, the inverter losses that are associated with converting P_{dc} to AC power (P_{ac}). An average inverter efficiency of 0.95 is used, based on the EU-weighted efficiency relationship in Eq. 2.12. The necessary efficiency values for a higher DC voltage corresponding to the ratio of power output to rated power are taken from Figure 2.9.

$$\eta_{EU} = 0.03\eta_5 + 0.06\eta_{10} + 0.13\eta_{20} + 0.10\eta_{30} + 0.48\eta_{50} + 0.20\eta_{100} \tag{2.12}$$
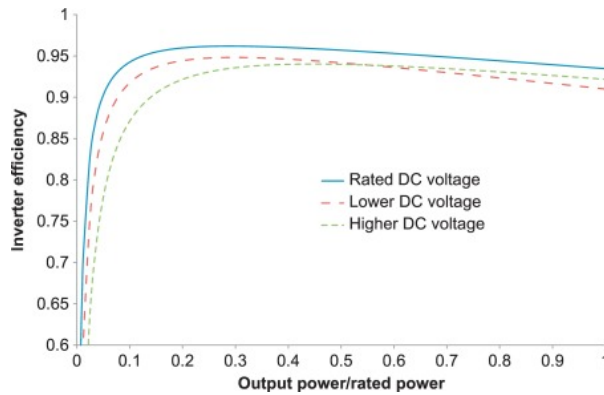
Figure 2.9: DC-to-AC inverter efficiency for rated, lower, and higher DC voltage (Baumgartner, 2017)

The effect of losses on the final P_{ac} is shown in Figure 2.10. This figure illustrates the effects of system and inverter losses, which result in a lower final AC power output.
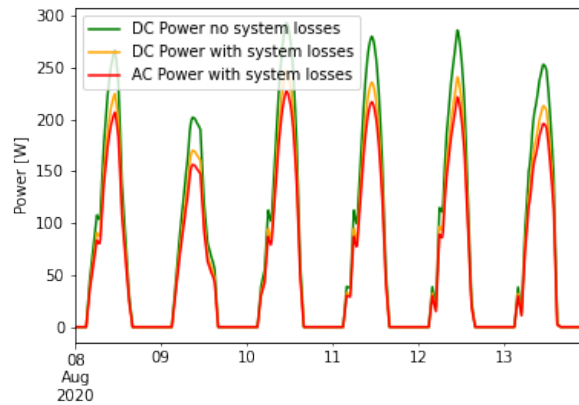
Figure 2.10: A 400W PV module with no, DC and inverter losses for a monocrystalline monofacial fixed PV panel in Fujairah, UAE

2.4. System cost calculation

This section describes the system costs, which comprise three main components, the PV system, the BESS, and the inverter. Section 2.4.1 describes the cost components of a PV system, which include the inverter costs. The cost component of the BESS is provided in Section 2.4.2. Finally, the total system cost used for the sizing approach is described in Section 2.4.3. The system costs are all the costs during the system lifetime. Some costs are incurred as initial investments and others during the system lifetime. The monetary value decreases due to interest accrual and inflation over time; therefore, these costs must be discounted. Discounting provides insight for investors regarding how much the investment will be worth in the future. The discount factor, r, based on the weighted average cost of capital ($WACC$), is initiated to account for this discounting. This single number represents the rate at which a company is expected to pay its debt to finance its equity. The method used by Vopak to calculate the $WACC$ is confidential and differs per country. The lifetime of this system (N) is assumed to be 25 years. The costs are all based on benchmark costs from the US in 2020.

2.4.1. Cost components of a PV system

The cost of the PV system comprises three components. The capital expenditure cost ($CAPEX_{pv}$ [$]) is also known as the initial investment costs of the PV system. The operational expenditure ($OPEX_{pv}$ [$]) is the system's annual operating cost. The cost of decommissioning ($C_{decom,pv}$ [$]) the PV system is the associated cost when it reaches the end of its lifetime and must be removed.

Capital expenditure cost of a PV system

The capital expenditure of a PV system ($CAPEX_{pv}$ [$]) depends on multiple components with a specific cost range, which can be divided into three categories: hardware costs, soft costs – labour, and soft costs – others. The designed systems vary in size between 10–100 MW; therefore, the assumed cost of a 10 MW PV system is taken as a starting point. A visualization of the assumed investment costs for a 10 MW PV installation is shown in Figure 2.11. The investment cost is 870–1,210 [$/kW]. The wide variation is mainly due to the developer overhead and price difference of the inverter. The developer overhead costs strongly depend on the business and staff expenses included in the CAPEX. These are assumed to be low because Vopak is a co-developer. Furthermore, if a high-end inverter (e.g. a DC power optimizer three-phase string inverter) is selected rather than a low-end inverter (e.g. a standard three-phase string inverter), the costs are higher. This system uses a hybrid inverter, assuming the costs are the average of those of a high- and low-end inverter. An overview of the different cost elements with corresponding ranges is provided in Appendix B.5. For this system, an average capital expenditure of 960 [$/kW] is used for a fixed-axis PV system with a monofacial polycrystalline module, including the costs of a hybrid inverter. The investment costs for different PV systems and locations depend on four elements: (a) the labour costs in different countries, (b) the module selected, (c) the

system size, and (d) the chosen tracking system.
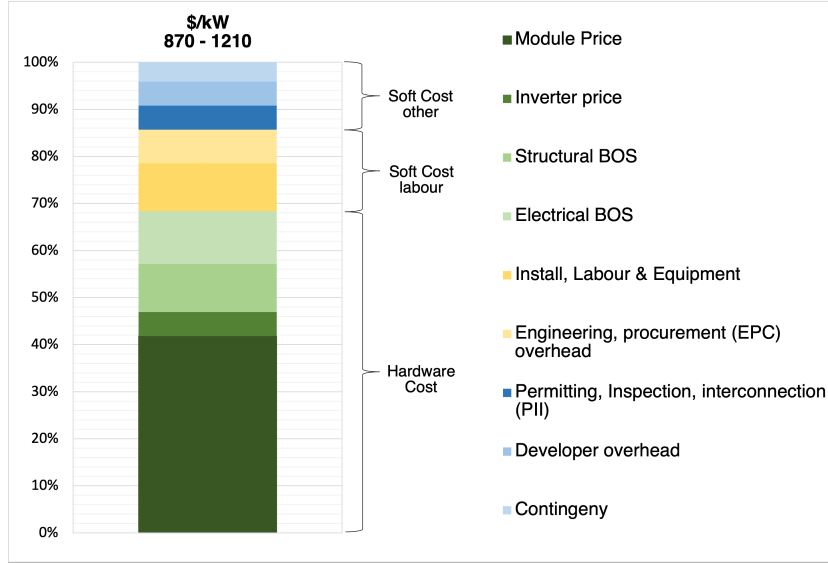
Figure 2.11: A breakdown of the different cost components of the capital expenditure for a fixed monofacial mono-crystalline 10 MW PV system (NREL et al., 2020)

Labour costs differ between countries, which causes a difference in the soft costs of labour (SCL). Therefore, benchmarking is performed based on the workers' wages at a location by the dimensionless factor φ for SCL. As shown in Eq. 2.13, φ comprises the normalization of workers' wages by taking the average yearly wage of the country of interest ([$]) and the average income of the US ($\omega_{U.S.}$ [$]), as these costs are based on the US.

$$\varphi_i(-) = \frac{\omega_i}{\omega_{U.S.}} \tag{2.13}$$

The factor α is implemented to distinguish between the module cost of monocrystalline/polycrystalline and monofacial/bifacial. The normalization is based on the average costs of a monofacial monocrystalline PV panel. Table 2.1 presents the different module types with corresponding α values. These factors are retrieved by taking the average values from the research conducted on PV technologies (see Appendix A).

Table 2.1: Module type cost factor

Module type	α
Monofacial - polycrystalline	0.88
Monofacial - monocrystalline	1.00
Bifacial - polycrystalline	0.95
Bifacial - monocrystalline	1.22

The system size is an important factor influencing the system costs, which are caused by economies of scale driven by hardware, labour, and related markups. As the system becomes larger, the costs per kW decrease (NREL et al., 2020). Based on the estimated cost for different PV sizes from NREL et al. (2020), equation 2.14 is formed. This is visualised in Appendix B.5. Where β is the scaling factor based on the PV size.

$$\beta(-) = \frac{1617 \cdot PV_{size}^{-0.127}}{1140} \tag{2.14}$$

$Cost_{rest}$ is the cost associated with the PV system except for SCL and the module cost ($Cost_{module}$). For simplicity, it is assumed that all the solar panel hardware originates from China, as China possesses over 80% of the PV manufacturing market (IEA, 2022). By combining these three factors, the capital expenditure of a fixed-axis PV system is given by Eq. 2.15.

$$CAPEX_{fixed}^{pv}(\$/kW) = (Cost_{module} \cdot \alpha + SCL \cdot \varphi + Cost_{rest}) \cdot \beta \tag{2.15}$$

The analysis presented in Appendix A indicates a cost difference between a fixed-axis system and a single-axis tracking system. On average, a single-axis tracking system costs 15% more than a fixed-tilt system. The capital expenditure of a HSAT system is calculated using Eq. 2.16.

$$CAPEX_{HSAT}^{pv}(\$/kW) = 1.15 \cdot CAPEX_{fixed}^{pv} \tag{2.16}$$

Operational expenditure of PV

The operation and maintenance (O&M) costs are also known as operational expenditure (OPEX). According to Sandia Laboratories (2015), the $OPEX_{pv}$ typically accounts for 1% to 5% of an MW-class plant's total $\$/kW_{DC}$ expenditure. Costs range roughly between \$10/kW-year and \$45/kW-year. For larger systems (1 MW and larger) O&M costs range between 10–25 [\$/kW-year]. Appendix B.6 presents the relevant elements that affect the O&M costs with a description, cost range, and selected $OPEX_{pv}^{loc}$ per location. The cost structure of $OPEX_{pv}^{loc}$ is visualized in Figure 2.12.
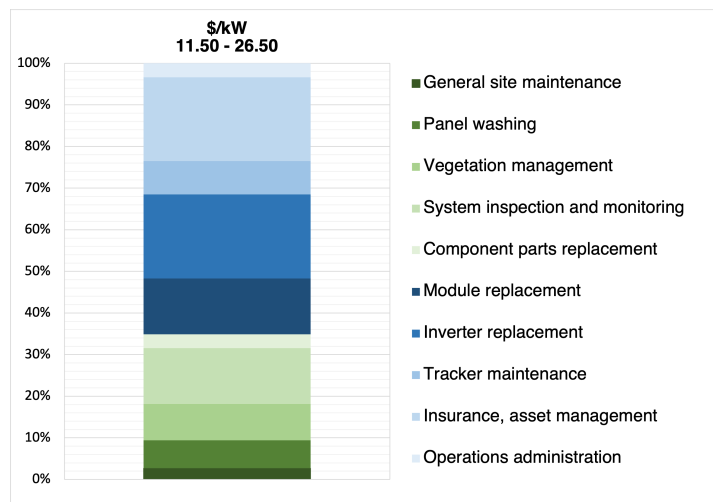
Figure 2.12: A split of the different components of the O&M cost of a PV system (Andino García et al., 2021; Feldman et al., 2020; Sandia Laboratories, 2015)

So far, the cost of land or the annual cost to rent the land has not been mentioned in the O&M breakdown. The cost of land [\$/kW] depends on two components. Firstly, the financial and ownership construction of the storage terminal determine the annual cost to rent [$\$/m^2$]. Secondly, the power density of the PV system [m^2/kW] which depends on the system size. The size of the PV system is determined by the GCR, which depends on the spacing between the rows of modules (d) and the width (ω) of the module, as depicted in Figure 2.13.
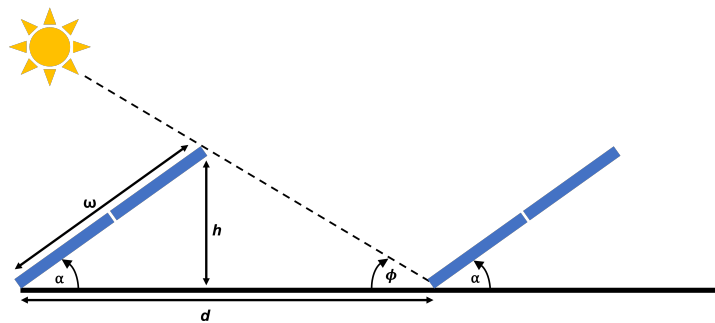
Figure 2.13: Schematic representation to determine the minimum spacing between rows of PV modules

According to the design guidelines from Chakraborty et al. (2015), a rule of thumb for the minimum spacing (pitch) is given by Eq. 2.18.

$$d(m) = 3 * w * \sin(\alpha) + w * \cos(\alpha) \tag{2.17}$$

The designed PV system comprises two attached modules; thus, the panel width (ω) is twice the width of one panel. The PV systems use four different types of modules from Canadian Solar, each with slightly different dimensions. Each panel has a rated power output of 0.4 $[kW]$. For example, if ω is 4 [m], and the length of one panel (L_{pv}) is 1 [m], the resulting power module per meter row becomes 0.8 $[kW \cdot m^{-1}]$. Thus the power density $[m^2/kW]$ is calculated by dividing the minimum spacing by the power module per meter row. Ultimately, the cost of land [$/kW] is retrieved by Eq. 2.18.

$$\textit{Cost of land (\$/kW)} = \textit{Annual cost to rent} * \textit{Power density} \tag{2.18}$$

The final $OPEX_{pv}$ is calculated using Eq. 2.19.

$$\textit{OPEX}_{pv}(\$/\text{kW}) = \textit{OPEX}_{pv}^{loc} + \textit{Cost of land} \tag{2.19}$$

Decommission cost of PV
The decommissioning costs ($C_{decom,pv}$ [$/kW]) of a PV system are the retirement costs of the system at the end of its lifetime. The cost includes removing the PV array, removing the balance of the system equipment, and restoring the land or infrastructure to its original condition or preparing it for a new use, according to Barbosa (2020). Four scenarios are available for decommissioning the PV system (Curtis et al., 2021):

- Decommissioning at the end of its economic life
- Extending the lifetime with increasing O&M costs followed by decommission
- Refurbishing the PV system by correcting any deficiencies followed by decommission
- Re-powering the PV system with new modules and inverters

This system is assumed to be fully decommissioned at the end of its economic life. However, at the end of its lifetime, components of the PV system can be reused, recycled, or even sold. This is known as the residual value. Components such as PV modules, the balance of the system components (inverters, transformers, wires etc.), and scrap metals can fully compensate for or reduce the real decommissioning cost of the system. Table 2.2 indicates that the decommissioning cost are between 5–83 [$/kW] based on different sources; an average value of 39 [$/kW] is used as $C_{decom,pv}$.

Table 2.2: An overview of the real decommissioning costs, including subtraction of the residual value; n/s means not specified

Size (MW)	Decommissioning cost ($)	Residual value ($)	Real decommissioning cost ($/kW)	Source
11	1,284,155	371,341	83	(Bolen & Libby, 2018)
2	60,200	n/s	30	(Kolbeck, 2022)
1	18,300 - 110,000	0 - 120,000	5	(Boelens et al., 2022)
1	21,700 - 56,300	n/s	39	(MPUC, 2018)

The decommissioning costs are incurred at the end of its lifetime. Therefore, the decommissioning costs are discounted to the value in the last year. This is shown in Eq. 2.20.

$$C_{decom,pv}(\$/kW) = \frac{C_{decom,pv}^{year=0}}{(1+r)^{N+1}} \tag{2.20}$$

2.4.2. Cost components of a battery energy storage system
As explained in Section 2.1, the storage system comprises four battery types: Li-ion batteries with storage durations of 4 and 8 hours and VRF batteries with storage durations of 4 and 8 hours. The battery system cost comprises the capital expenditure of the battery during the system lifetime, including replacement costs ($CAPEX_{bat}$ [$]), OPEX of the battery ($OPEX_{bat}$ [$]), and decommissioning costs of the battery ($C_{decom,bat}$ [$]).

Capital expenditure of the battery system

The capital expenditure of a battery system comprises two elements: the initial capital expenditure at the start of the project and the replacement of the storage block of the battery during the system lifetime. The initial capital expenditures ($CAPEX_{bat,initial}$ [$/kWh]) depend on the storage duration and the scale of the system. For simplification, it is assumed that the supply chain and shipping costs of the BESS are the same for all countries. A battery comprises components determined by the energy capacity [kWh] and other parts based on the power capacity [kW] of the battery. Appendix B.6 shows the cost range of the battery components for both batteries for a discharge/charge of 4 and 8 hours. Figures 2.14 and 2.15 show the average of each cost component of the battery used for the $CAPEX_{bat,initial}$, broken down in $/kWh and $/kW. The storage block and storage balance of the system comprise the storage system. An energy storage system is built by including the power equipment, controls communication, and system integration components. For the full installation, project development and engineering, procurement construction (EPC) costs must be added. The installed capital costs for the BESS in terms of $/kWh decrease with storage duration, and costs in $/kW thus increase. This inverse behaviour highlights the importance of distinguishing the two types of battery capacity when discussing the cost of energy storage.

Figure 2.14, show that the installed capital costs in terms of $/kWh have a stronger decrease with increasing storage duration for the VRF battery than the Li-ion battery. This is because in VRF batteries, the power and energy capacity are designed separately. The power [kW] of the system is determined by the size of the electrodes and the number of cells in a stack, whereas the energy storage capacity [kWh] is determined by the concentration and volume of the electrolyte. Therefore, energy and power can easily be adjusted for longer storage duration. As a result, only the cost of the energy component need to increase for a longer storage duration. Whilst, the Li-ion battery has a traditional battery design, where the stored energy is directly related to the amount of electrode material. To increase the energy capacity of these battery systems, the power capacity needs to increase by adding more cells. Therefore, to increase the storage duration, both power and energy components need to increase; thus, only minimal cost reduction can be realised.

Based on the cost performance report from the DOE (2020), the relationship between the battery size and the initial capital expenditure for a battery system can be visualized for storage durations of 4 and 8 hours for both batteries; see Appendix B.6. The corresponding trend line is used to determine the $CAPEX_{bat,initial}$ of the four different batteries.
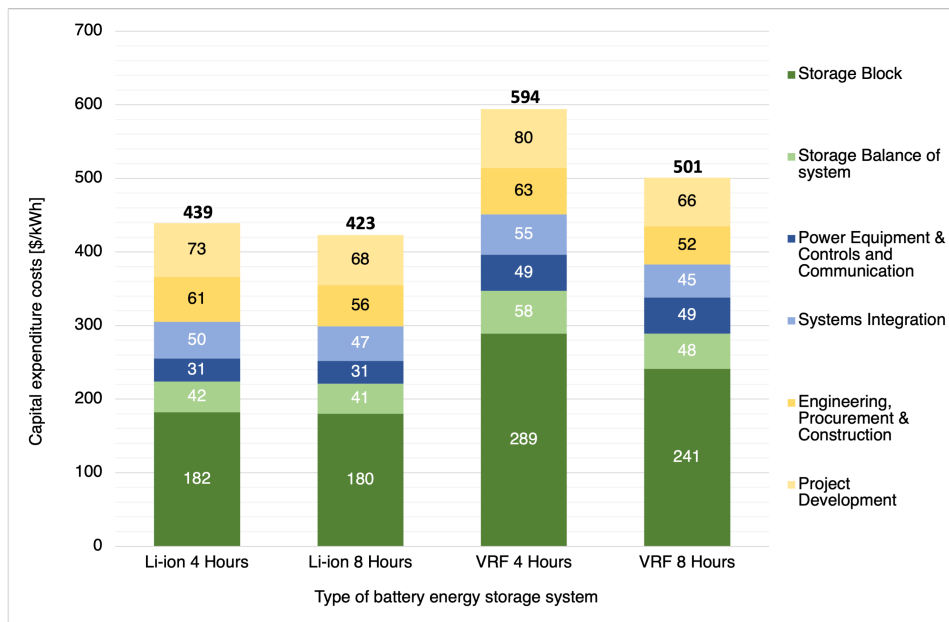
Figure 2.14: Cost breakdown of the $CAPEX_{bat,initial}$ in [$/kWh] based on values from DOE (2020)
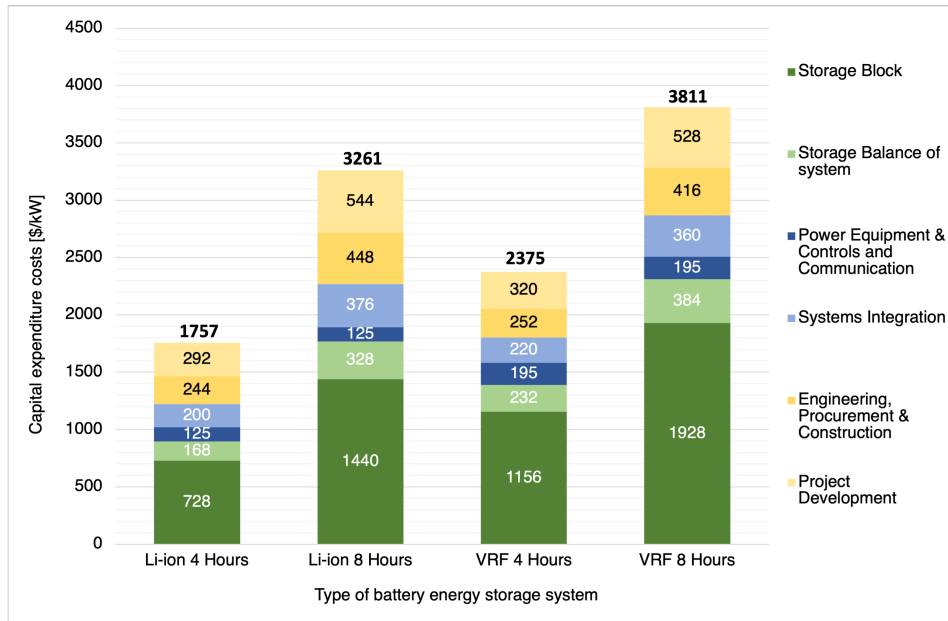
Figure 2.15: Cost breakdown of the $CAPEX_{bat,initial}$ in [\$/kW] based on values from DOE (2020)

The batteries must be replaced during the system lifetime, resulting in a replacement cost ($CAPEX_{bat,rep}$). The battery costs are expected to decrease during the system lifetime due to the learning rate and scale-up. The battery's cycle life determines the replacement of the battery. If a battery has a longer cycle life, the battery needs to be replaced less often. The replacement costs in this study assume that the battery operates one cycle per day. Eq. 2.22 is taken from Y. Xu et al. (2022) to account for the discounted replacement cost of the battery. Where C_{bat} is the storage block cost of the system, this is estimated as 40% of the CAPEX for Li-ion and 50% for VRF, according to Y. Xu et al. (2022). Based on the projected CAPEX decrease from Mongird et al. (2020), an annual cost reduction in installation cost is given as a percentage κ; λ is the λth time needed to replace the batteries, and l is the battery lifetime. It is assumed that the cycle life remains constant during the entire system lifetime.

$$CAPEX_{bat,rep}(\$/kWh) = \sum_{\lambda=1}^{N} \frac{C_{bat}(1-\kappa)^{\lambda l}}{(1+r)^{\lambda l}} \tag{2.21}$$

The total capital expenditure of the battery ($CAPEX_{bat}$ [\$]) is the sum of the initial capital expenditure of the battery system and the replacement cost during the system lifetime. This is expressed in Eq. 2.22.

$$CAPEX_{bat}(\$/kWh) = CAPEX_{bat,initial} + CAPEX_{bat,rep} \tag{2.22}$$

Operational expenditure of the battery system
The operational expenditure of the battery system ($OPEX_{bat}$ [\$/kW-year]) is estimated between 3–16 [\$/kW-year] (PNNL et al., 2019). Table 2.3 shows the cost estimation for the four different types of battery storage systems, from DOE,2020. The average is taken from these O&M values for the $OPEX_{bat}$ [\$/kW-year]. The O&M costs required to rent land are not included because the size of the battery system is assumed to be negligible compared to the size required for the PV system. The dimensions of large-scale industrial batteries (MW) are roughly the size of a couple of containers.

Table 2.3: O&M costs for a PV system (DOE, 2020)

Battery type (storage duration)	O&M cost ($/kW - year)
Li-ion (4 hours)	3.96 - 4.84
Li-ion (8 hours)	7.30 - 8.92
VRF (4 hours)	6.11 - 7.47
VRF (8 hours)	9.70 - 11.86

Decommission cost of the battery system

The decommissioning costs of the battery ($C_{decom,bat}$ [$/kWh]) comprise two cost components. The first is the costs [$/kWh] associated with the disconnection, disassembly, removal, and site restoration. These costs can vary widely depending on the location (in the built or outside the built environment), how far the materials must be transported, and whether site remediation is necessary. This study uses the average transport costs and average costs to disconnect and disassemble a BESS from Viswanathan et al. (2022); these costs are estimated to be 10.50 [$/kWh] for all batteries.

The second is the net costs [$/kWh] associated with recycling and disposal of the components minus the recouped sale of materials. These costs differ for the two storage batteries. In this analysis, the net recycling and disposal costs are based on the method proposed by Viswanathan et al. (2022). This is achieved by constituting a reversal of the initial engineering, procurement, and construction costs minus the money recouped from the material of the battery modules during recycling. Li-ion batteries have very low recycling and disposal costs, driven by the high demand for Li-ion batteries due to their use in electric vehicles and consumers' electronics, which requires the extraction of lithium as well as other valuable metals. The costs for Li-ion batteries with different storage durations are identical because the technical architectures of electrochemical batteries are the same. The costs associated with recycling and disposal of a vanadium redox flow battery are higher. This is because few systems have reached the end of their life and passed through a recycling process. These costs are lower for a VRF with a longer storage duration (8 hours) because the system has a higher energy storage capacity and thus more vanadium, which can later be sold for a system with roughly the same power component costs (as the 4-hour VRF). The estimated decommissioning costs for the two batteries are presented in Table 2.4.

Table 2.4: Overview of the two cost components of the total decommissioning costs for a VRF and Li-ion battery (Viswanathan et al., 2022)

Battery type	Li-ion		VRF	
Storage duration (hours)	4	8	4	8
Disconnection, disassembly, removal, and site restoration costs ($/kWh)	10.50	10.50	10.50	10.50
Net recycling & disposal costs ($/kWh)	2.65	2.65	36.50	29.98
Decommissioning costs ($/kWh)	**13.15**	**13.15**	**47.00**	**40.48**

The decommissioning cost is incurred at the end of the system's lifetime. Therefore, these costs are discounted to the value in the last year. This is shown in Eq. 2.23.

$$C_{decom,bat}(\$/kWh) = \frac{C_{decom,bat}}{(1+r)^{N+1}} \tag{2.23}$$

2.4.3. Total system cost

The total system costs ($Cost_{system}$ [$]) of the PV system and BESS, are described in this Section. When a PV system and a battery system are combined, the two systems become DC- or AC-coupled. This model is based on DC-coupling because it is more efficient for systems where PV energy is mainly stored and used later and it has self-restarting capabilities (NREL et al., 2020). DC-coupling adds an estimated 1% to the total system costs (Ardani et al., 2016). According to (NREL et al., 2020), the combined electrical balance of system (BOS) costs for PV and battery systems are reduced by an estimated 10% due to the removal of duplicate parts. Additionally, the installation labour costs are reduced on average by 10% because duplicate work is removed. Additionally, costs are reduced

related to site preparation, overhead, profit, and hardware (sharing of hardware such as transformers, switchgears, and controls). The combined cost reduction for this system is estimated as 20% (NREL et al., 2020). The total CAPEX ($CAPEX_{total}$ [$]) of the system is shown in Eq. 2.24, where the capacity of the PV system is $Capacity_{pv}$ [kW] and $Capacity_{bat}$ [kWh] is the capacity of the BESS.

$$CAPEX_{total}(\$) = 0.80 * (CAPEX_{pv} * Capacity_{pv} + CAPEX_{bat} * Capacity_{bat}) \tag{2.24}$$

For simplification, $OPEX_{total}$ is used for the sum of the discounted OPEX of the PV and BESS, and $C_{decom,total}$ refers to the total decommissioning costs of the PV and BESS. This is shown in Eq. 2.25 and 2.26.

$$OPEX_{total}(\$) = OPEX_{pv} * Capacity_{pv} + OPEX_{bat} * \frac{Capacity_{bat}}{Storageduration} \tag{2.25}$$

$$C_{decom,total}(\$) = \frac{C_{decom,pv}}{(1+r)^{N+1}} * Capacity_{pv} + \frac{C_{decom,bat}}{(1+r)^{N+1}} * Capacity_{bat} \tag{2.26}$$

When an investment is made, lifetime financial costs are incurred. The discounted financial cost (F [$]) comprises mandatory financial debt payment and corporate tax. The mandatory financial debt payments comprise annual debt payments and the annual interest on the debt. The annual debt payments depend on how much of the investment is financed with equity and how much is debt. The amount of debt and the total number of years agreed to pay back the debt determine the annual debt payment. The annual interest rate on debt is based on the long-term annual interest value of the storage terminal location. Corporate tax is the annual tax that must be paid based on taxable income and depreciation. The $Cost_{system}$ is summarized in Eq. 2.27.

$$Cost_{system}(\$) = CAPEX_{total} + C_{decom,total} + \sum_{n=1}^{N} \frac{OPEX_{total}}{(1+r_n)^n} + \sum_{n=1}^{N} \frac{F_n}{(1+r_n)^n} \tag{2.27}$$

2.5. Sizing model
This section explains the sizing approach of the Linck model. As mentioned, the PV model output provides insight into the energy yield ([MWh/MW$_p$]) a PV system generates throughout the year. The goal of this sizing model is to calculate the size of the PV system [MW] and the BESS [MWh] for an autonomous system. As mentioned, the goal of the system is to be CRAP. Thus, the sized system must always satisfy the load without requiring additional energy from the grid to be reliable and autonomous. Furthermore, the system must be sized correctly to achieve the lowest system cost. Section 2.5.1 describes the inputs necessary for the sizing model. The sizing problem and implemented energy management strategy are explained in Section 2.5.2. Finally, the implemented sizing approach is described in Section 2.5.3.

2.5.1. Inputs
The sizing approach uses two inputs. The first is the hourly AC energy output ($P_{ac,pv}$ [MWh/MW$_p$]) of the eight different PV systems, as explained in Section 2.3. The second is the hourly load requirement of Vopak's storage terminal [MWh]. As mentioned, Vopak operates storage terminals in and outside the Netherlands and uses different methods to store load data. For storage terminals in the Netherlands, the energy usage has been monitored every hour since 2018. To create a "worst case" load scenario, the maximum load is taken for every hour between 2018-2021. For storage terminals outside the Netherlands, Vopak only has data available when pumps are active (number of hours). The pumps are needed to handle chemicals, gases, and oil products. Most of the energy demand of a terminal is determined by the operations of the pumps, thus this provides a realistic estimate of the energy demand of storage terminals outside the Netherlands. By combining data for when a specific pump is active with the power usage of a pump [MW], the storage terminal load [MWh] is estimated.

2.5.2. Problem formulation
A sizing model is necessary to determine the CRAP system size of a PV and battery. Too large a battery will increase the initial investment cost (but also have a longer battery lifetime). Conversely, a smaller battery size results in an unmet load (E_{unmet} [MWh]) as insufficient stored energy is available

to power the load during non-sunlight hours (Narayan et al., 2019). Likewise, a smaller PV size results in a high load loss. However, too large a PV size results in high dumped surplus energy (E_{dump} [MWh]), which wastes energy and increases the system cost. An energy management strategy is developed to understand how the autonomous system works to determine how the PV and battery energy flows through the system.

Figure 2.16 shows a flowchart of the energy management system. The algorithm used for energy management is simulated for every time step, t (1 hour). As shown in the flowchart, at the start of every time step, the excess energy (E_{excess}) is calculated using Eq. 2.28. Here, the energy of the PV system, E_{pv}, is the product of the PV size ($P_{pv,size}$ [MW]) and $P_{ac,pv}$ [MWh/MW$_p$]. E_{load} [MWh] is the energy load of the storage terminal.

$$E_{excess} = E_{pv} - E_{load} \tag{2.28}$$

If $E_{excess} > 0$, the load is fully met, and the excess energy is used to charge the battery. If the battery is full, it is assumed that the overproduced energy is dumped. If $E_{excess} < 0$, and $E_{battery} > E_{battery,min}$ the additional battery energy is used to feed the load. If insufficient energy remains in the battery, the energy demand of the load is unmet. If the system is connected to the grid, the grid will supply the necessary energy to satisfy the load. However, this system is autonomous; therefore, if this occurs, the energy load of the storage terminal is not satisfied. For simplification, it is assumed that the battery has a self-discharge rate of zero.
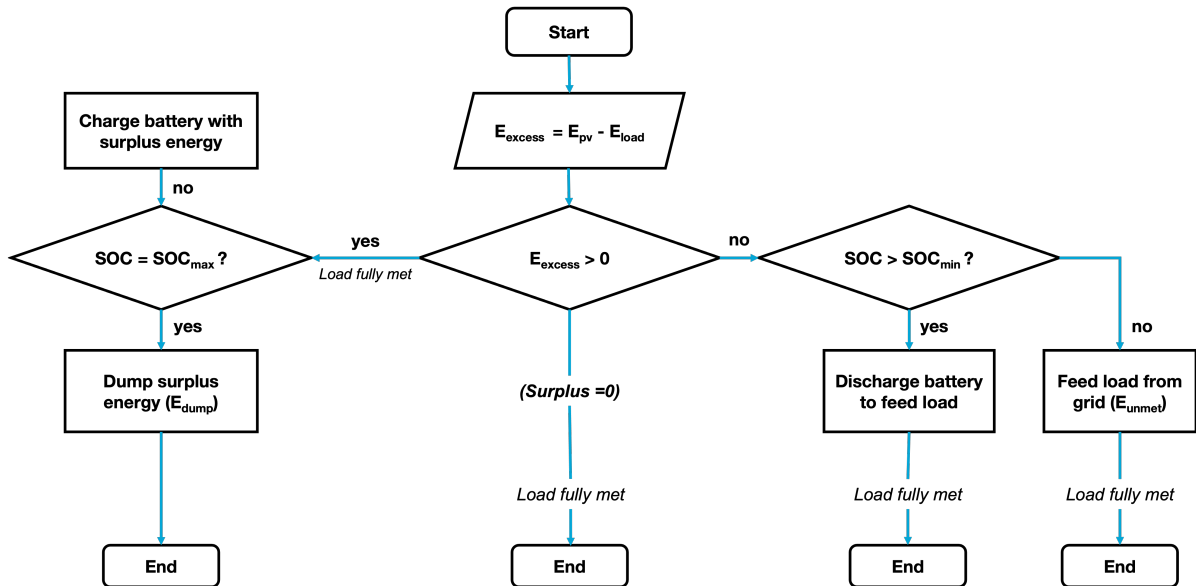
Figure 2.16: Flowchart explaining the energy management strategy used for the system; this represents the algorithm every time step t

Decision variables

Two variables determine the system performance for the sizing: P_{pv} [MW] and $E_{battery}$ [MWh]. These variables influence how much energy is unmet or dumped and the total system costs.

$$\text{Decision variables} = \begin{cases} P_{pv} \text{ (MW)} \\ E_{battery} \text{ (MWh)} \end{cases} \tag{2.29}$$

Objective function

The objective of the system is to be CRAP. Therefore, the objective is to size the cheapest system; thus, the system costs ($Cost_{system}$) must be minimized, as described in Section 2.4.3. Summarized, the single-objective function is

$$\text{Objective functions} = \text{Minimize: } Cost_{\text{system}}(\$) \tag{2.30}$$

Constraints
Certain constraints are needed for the system to be sized as desired. For the system to be reliable and autonomous, the sizing approach aims to determine the PV and battery size for a system that always meets the energy load without interaction with the grid; this is realized by adding the following energy balance constraints. Furthermore, the following battery constraints are needed to ensure that the BESS operates accordingly.

Energy balance constraint:

$$E_t^{pv} + E_t^{unmet} = E_t^{load} + E_t^{battery} + E_t^{dumped} \quad \forall t \in \{1, 2, \ldots, T\} \tag{2.31}$$

$$E_t^{unmet} = 0 \quad \forall t \in \{1, 2, \ldots, T\} \tag{2.32}$$

Where E_t^{pv} [kWh] is the PV energy output at time t; E_t^{unmet} [kWh] is the unmet energy load at time t; E_t^{load} [kWh] is the load energy at time t; $E_t^{battery}$ [kWh] is the battery energy at time t; and E_t^{dumped} [kWh] is the PV energy that is dumped at time t.

Battery constraints:

$$E_t^{battery} = E_{t-1}^{battery} + \eta P_t^{charge} - (1/\eta) P_t^{discharge} \quad \forall t \in \{1, 2, \ldots, T\} \tag{2.33}$$

$$a_{lim} E_{max}^{battery} \leq E_t^{battery} \leq b_{lim} E_{max}^{battery} \quad \forall t \in \{1, 2, \ldots, T\} \tag{2.34}$$

$$E_{initial}^{battery} = 0.5 E_{max}^{battery} \quad \forall t \in \{1, 2, \ldots, T\} \tag{2.35}$$

$$0 \leq P_t^{charge} \leq P_{max}^{battery} y_t \quad \forall t \in \{1, 2, \ldots, T\} \tag{2.36}$$

$$0 \leq P_t^{discharge} \leq P_{max}^{battery} (1 - y_t) \quad \forall t \in \{1, 2, \ldots, T\} \tag{2.37}$$

$$y_t \in {0, 1} \quad \forall t \in \{1, 2, \ldots, T\} \tag{2.38}$$

The charge and discharge process of the battery is described in Eq. 2.33, where Eq. 2.34 ensures that the state of charge (SOC) remains within certain limits. The lower limit is given by a_{lim}, and b_{lim} is the upper limit. In this problem, it is assumed that the initial battery energy starts with a SOC of 50%, as shown in Eq. 2.35. This percentage is selected because it is between the minimum and maximum limits of the battery energy. Equations 2.36 to 2.37 ensure that the battery is charged/discharged within its power limits, with y_t as a binary variable to ensure that charging and discharging of the battery cannot occur simultaneously.

2.5.3. Grid-search system selection method for sizing
Different optimization techniques are available to size a system with high accuracy. The most widely used is (non-)linear programming, which has many advantages but there is minimal transparency in how the optimal solutions are found, for example this can result in undesired local minimum values. Local minimum is the lowest point at nearby points but larger than a more distant point. For Vopak, it is important to understand how the sizing of the system offers certain possibilities, such as an efficient, autonomous, or cheap system. The goal of this sizing method is to explore the sizing capabilities of a certain system. Ultimately, the grid-search system selection method is chosen because it offers the user flexibility, inclusiveness, and transparency (FIT) when sizing the system.

The sizing method is inclusive because it includes a full overview of all output values for all PV and battery configurations. This method creates a multidimensional grid of points based on the boundaries of varying input variables and chosen step size. The input variables are the PV and battery system size. The step size determine the number of input variables need to be evaluated within the boundaries. The boundaries differ for every system, for example, 0–25 [MW] or 10–20 [MW]. The grid boundaries

are determined by first modelling for a large grid with a large step size, such as Δ = 1. This produces an approximation of the system size limits. Subsequently, by decreasing the step size, the model calculates the system more accurately. This model uses a step size of Δ = 0.1, a smaller step size results in a significantly longer running time with an additional accuracy not needed by Vopak. Every point calculates the output values of the amount of dumped energy, unmet energy, and system cost, as described by the energy management system; see Section 2.5.2. An example of the relationship between the PV and battery system sizes and the output values is visualized in Figure 2.17.

(a) Energy unmet   **(b)** Energy dumped   **(c)** System Cost
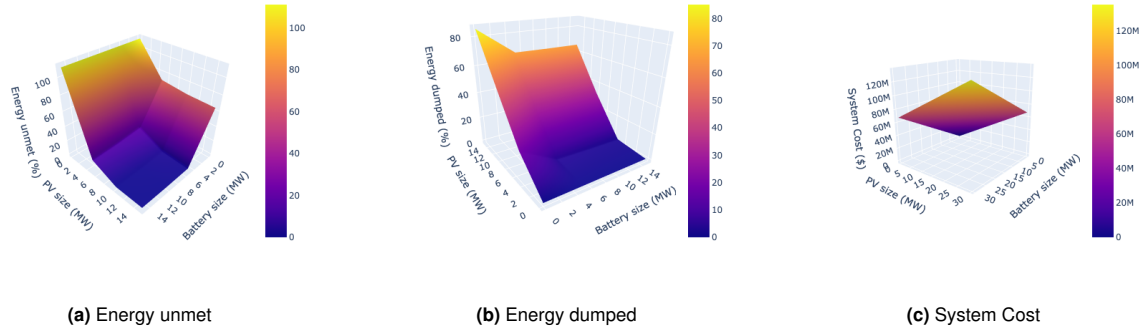
Figure 2.17: Output from energy management system for all grid points

The sizing method is also transparent as the user can (easily) assess the system configurations when a certain constraint is added. The constraint for the CRAP system is $E_{unmet} \approx 0$, the model searches through all the outputs from the grid to select the values corresponding to the constraint. Thereafter, the method search the autonomous system for the lowest system costs.

Finally, the method is flexible when other indicators are considered in selecting the system size. The method can show the trade-off between indicators, when a certain constraint is implemented. In this study, an indicator that could affect the decision-making of the system is the percentage of energy dumped (E_{dumped} [kWh]). This indicator can be important because, in the future, the system could benefit from selling surplus energy to the grid, a policy may be enforced that limits the amount of dumped energy generated, or the decision-maker may want a system with higher efficiency. This influences the system sizing choice, despite costs being the most important criteria. This method provides insight into this trade-off between minimizing the system cost ($Cost_{system}$ [$]) to ensure a cheap system and minimizing the amount of energy dumped (E_{dumped} [kWh]) for an "efficient" system. An example of a trade-off output is presented in Figure 2.18.
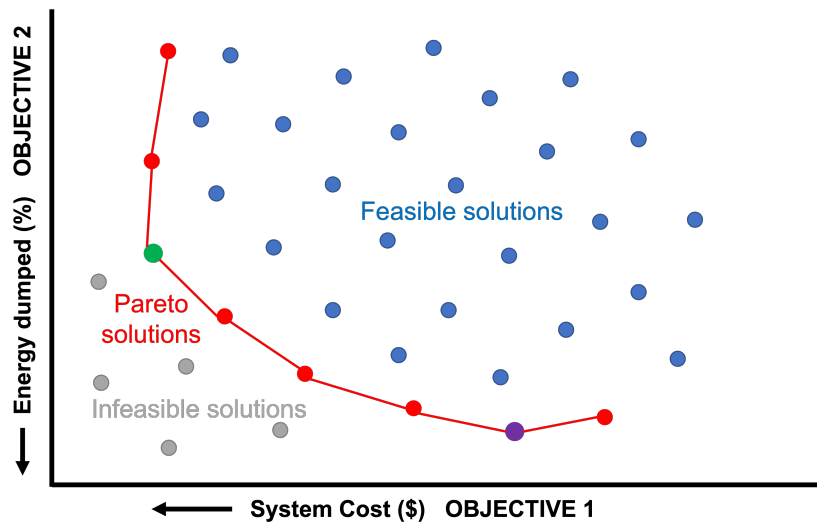
Figure 2.18: Visual representation of Pareto-optimal solutions

Here, the red dots are the set of trade-off solutions, generally known as Pareto-optimal solutions. According to Xin (2013), these solutions are optimal because no other solutions in the design space can "dominate" them when considering all the objectives. The red line can be drawn from these results, which shows the Pareto frontier. The blue dots show other feasible solutions, and the grey dots are infeasible solutions as these do not satisfy the constraint. Based on Figure 2.18, two extreme values exist. The purple dot is the most "efficient" system (lowest amount of PV energy dumped), and the green dot is the cheapest system. However, for example, when a limit is enforced on the amount of dumped energy, a different Pareto solution is chosen. As mentioned in this model, the goal is to determine the lowest-cost configuration. In this case, the sizing represented by the green dot is chosen.

As mentioned, the model will be used to find the battery size of a lithium-ion and vanadium redox flow battery. Table 2.5 shows the properties for both batteries which are used as inputs for the model. It is assumed that both batteries have a negligible self-discharge rate.

Table 2.5: Battery properties used for the optimization model from Table A.19 and DOE (2020)

Battery type	Vanadium Redox flow battery	Lithium-ion battery	Unit
a (lower limit)	10	20	%
b (upper limit)	95	95	%
Cycle life	5200	2000	Cycles
Charge/discharge efficiency	85	95	%
Charge/discharge hours	4 & 8	4 & 8	Hours

2.6. System economics

The system economics is evaluated by calculating the levelized cost of solar plus storage (LCOSS). The LCOSS [$/kWh] is a similar concept to the payback time for an energy system. However, rather than calculating how much time is needed to recover the initial investment, the LCOSS determines how much money is needed per unit of electricity [kWh]. The LCOSS is a valuable tool because it combines fixed and variable costs into a single measurement for simple analysis (Namovicz, 2013). The value of the LCOSS enables comparison of different systems of unequal project size, life spans, return, capacities, and capital costs and risks. This is critical when deciding whether a system is viable to implement.

The LCOSS [$/kWh] is calculated by evaluating the costs endured during the lifetime of the system and how much of the generated energy is used by the system. The total system costs of the PV and battery system ($Cost_{system}$ [$]) are described in Section 2.4.3. The amount of energy the system generates and eventually uses is provided by $E_{pv,used}$. This is equal to the load of the storage terminal because the system is autonomous and thus unused energy is dumped. This energy needs to be discounted, even though it is assumed to produce constant revenues in the future. However, these revenues due to the time value of money decrease i.e. revenue today is more worth then the future revenues. The calculation of the LCOSS is shown in Eq. 2.39.

$$LCOSS(\$/kWh) = \frac{Cost_{system}}{\sum_{n=1}^{N} \frac{E_{pv,used}}{(1+r_n)^n}} \tag{2.39}$$

3

Case study: Location selection

In this chapter, the case study for different storage terminals is described to verify the method described in Chapter 2. Vopak has 79 storage terminals worldwide. The following terminals are chosen: Vopak Horizon Fujairah, Vopak Terminal Laurenshaven and Vopak Panama. Firstly, these storage terminals are located in three different climates: desert, maritime and tropical. This will show the influence certain meteorological conditions have on a system. Secondly, the storage terminals are different in size and thus have a different energy load. This will provide insight into the scale of a certain system. Thirdly, the storage terminals all store, transport, and distribute petroleum-based products. Therefore the operating method is similar for all locations. Fourthly, all the storage terminals are located near the coast and suffer from the same marine conditions. Fifthly, all the storage terminals own land suitable for a large PV and battery system. Figure 3.1 shows the three chosen storage terminals.

In the following sections, background information and an explanation of the meteorological conditions of the location are provided per storage terminal. In Section 3.1, a description of Vopak Horizon Fujairah is given, followed by an explanation of Vopak Terminal Laurenshaven in Section 3.2 and finally Vopak Panama is described in Section 3.3. Location specific (assumed) data and other relevant parameters used for the model can be found in Appendix B.

Vopak Panama
Tropical climate
Storage capacity: 0.38m cbm
Annual load: 7.709 MWh

Vopak Terminal Laurenshaven
Maritime climate
Storage capacity: 0.9m cbm
Annual load: 2.547 MWh

Vopak Horizon Fujairah
Desert climate
Storage capacity: 2.6m cbm
Annual load: 73.609 MWh
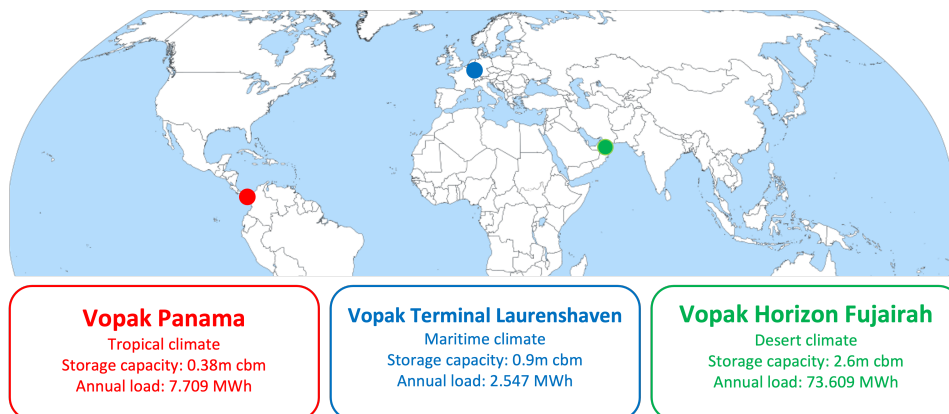
Figure 3.1: The three selected terminals on a world map with key terminal data

3.1. Vopak Horizon Fujairah

Vopak Horizon Fujairah (VHF) is an oil hub terminal defined as a regional storage and transport centre. It is Vopak's second largest storage terminal in the world. It is located at the mouth of the Strait of Hormuz on the Eastern side of United Arab Emirates (UAE) in Fujairah, with a GPS location of 25 °12'30.8"N and 45 °21'16.4"E. The terminal has about 2.6 million cubic meters of storage capacity with 73 storage tanks, six jetties and one single-point mooring buoy. The VHF has an annual load of 73,609 [MWh], with an average hourly demand of 8.51 [MWh]. VHF has ample area available for a PV and battery system, which Vopak already owns.

The climate in Fujairah is classified as a desert climate. This is reflected in the general climate conditions shown in Figure 3.2. The climate graph is from Meteoblue (2022), which is based on 30 years of hourly weather simulations and indicates typical climate patterns and expected conditions for precipitation, temperature and wind speed in Fujairah, UAE. The figure shows that Fujairah has a broad temperature range throughout the year. Furthermore, Fujairah suffers from a minimal rainy season between December and March, with 96% of the time no rainfall. The average wind is between 2 to 4 m/s. Table 3.1 mentions minimum and maximum data with corresponding technical criteria.

Fujairah is located in a desert climate and thus experiences dust storms. A study was conducted by Nazzal et al. (2019), who observed the number of hours per year in which dust storms affect visibility. The observation used data from 2010-2017 from Fujairah International Airport (I.A.), roughly 10km from Vopak Horizon Fujairah Terminal. Thus it can be assumed that conditions are more or less the same. From 69,364 measured hours, the results indicate that 0.13% represent severe dust storms and 90% of the time, blowing dust was reported. The data shows that the designed system needs to handle dust blowing for most of the year with (severe) dust storms for several hours (11-12 hours) per year. The dust conditions will affect the maintenance and system losses of the system.

Due to the severity of the dust conditions, a tracking system will not be included as a system option. Dust storms increase the risk of moving components and mechanical complexity, and this will cause damage and malfunctions to the system. Thus a fixed-axis tracking system is an optimal choice for the PV system in Fujairah due to the maintenance sensitivity of the system.
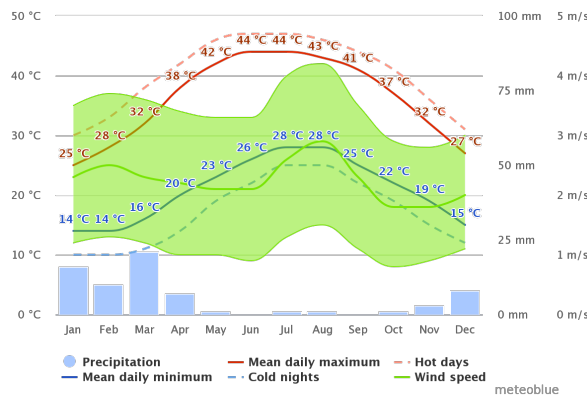
Figure 3.2: Average climate data of monthly temperature, wind and rainfall in Fujairah (Meteoblue, 2022)

Table 3.1: Summary of the minimum and maximum climate type values with corresponding criteria (Meteoblue, 2022)

Climate type	Minimum	Maximum	Criteria
Temperature (°C) (K)	10 (283)	47 (320)	System has an operational temperature between 283-320K
Wind speed (m/s)	0.3	17.2	System can resist a wind speed of 17.2 m/s
Rainfall (mm) (days)	0 (349)	50-100 (0.1)	System can handle a heavy rainfall for 3 hours/year

3.2. Vopak Terminal Laurenshaven

Vopak Terminal Laurenshaven (VTL) is part of Vopak Energy Terminals Netherlands and is located in the Botlek port area in the Port of Rotterdam with GPS coordinates 51°53'05.1"N 4°15'42.2"E. The terminal specialises in storing and transhipment gas, oil and diesel with a direct connection with Vopak Terminal Europoort. The terminal has a capacity of 0.9 million cubic meters with 15 tanks, one mooring point, three berths for barges and a direct pipeline to the Vopak Terminal Europoort. VTL has an annual load of 2,547 [MWh], with an average hourly demand of 0.29 [MWh]. VTL owns the land necessary for installing a PV and battery system. Therefore, no extra cost will be added for renting the land.

The climate at Vopak Terminal Laurenshaven (VTL) in the Netherlands is classified as an oceanic or maritime climate. This is a typical climate for the west coast in higher middle latitudes of Europe. Generalised as mild winters and cool summers (relative to their latitude). Furthermore, the temperature range is relatively broad, with a clear seasonal variation throughout the year. This maritime climate is reflected in the general climate conditions shown in Figure 3.3. The weather data shows that, on average, 50% of the time precipitation takes place, of which 40% of the time rain falls between 2-10mm. From the average temperature curve, there is a summer period of four months, from June to September, with average winds between 5-7 m/s. The minimum and maximum data with corresponding technical criteria are mentioned in Table 3.2.
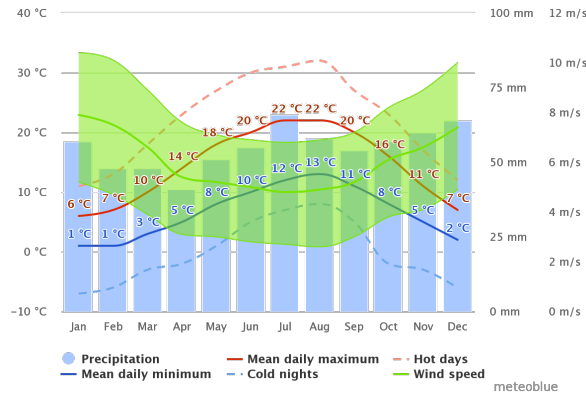
Figure 3.3: Average climate data of monthly temperature, wind and rainfall at Vopak Terminal Laurenshaven (Meteoblue, 2022)

Table 3.2: Summary of the minimum and maximum climate values with corresponding criteria for Panama (Meteoblue, 2022)

Climate type	Minimum	Maximum	Criteria
Temperature (°C) (K)	-5 (268)	32 (305)	System has an operational temperature between 268-303K
Wind speed (m/s)	1.6	17.2	System can resist a wind speed of 17.2 m/s
Rainfall (mm) (days)	0 (202.9)	50-100 (0.1)	System can handle rainfall for 45% of the year

3.3. Vopak Panama

Vopak Panama is an oil and gas terminal located at the Caribbean coast of Panama, with GPS coordinates 9°23'42.5"N 79°49'16.0"W. Vopak Panama terminal has a storage capacity of 0.38 million cubic meters with 9 tanks, 4 pipelines, an offshore jetty with 6 marine loading arms. These tanks were built to handle and store Very Low Sulfur Fuel Oil and Low Sulfur Marine Gas Oil. The Vopak Panama has an annual load of 7,709 [MWh], with an average daily usage of 0.88 [MWh].

The climate of Panama is classified as a hot and humid tropical climate with a long rainy season from May to January. The seasonal rainfall distribution is different on Panama's Atlantic and Pacific sides. The Caribbean coast, where Vopak Panama is located, receives more heavy rainfall than the Pacific region throughout the year. The level of rainfall throughout the year is reflected in the typical climate patterns and expected conditions for precipitation, temperature and wind speed for the terminal location in Panama, as shown in Figure 3.4. Furthermore, the climate data shows that it has a relatively constant temperature throughout the year, around 25 °C, with average winds between 2 and 4 m/s. The minimum and maximum data with corresponding technical criteria are mentioned in Table 3.3.
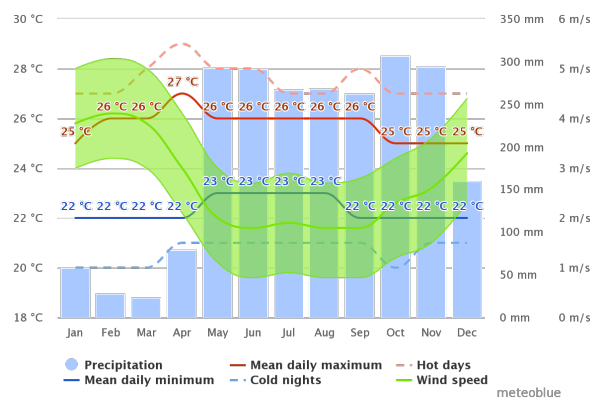
Figure 3.4: Average climate data of monthly temperature, wind and rainfall at Vopak Panama (Meteoblue, 2022)

Table 3.3: Summary of the minimum and maximum climate values with corresponding criteria for Panama (Meteoblue, 2022)

Climate type	Minimum	Maximum	Criteria
Temperature (°C) (K)	20 (293)	30 (303)	System has an operational temperature between 293-303K
Wind speed (m/s)	0.3	8.0	System can resist a wind speed of 8.0 m/s
Rainfall (mm) (days)	0 (92.6)	>100 (0.2)	System can handle rainfall for 75% of the year

3.4. Levelized cost of energy of the PV system

This section evaluates the impact of a location's climate on the cost-effectiveness of a stand-alone PV system. The cost-effectiveness is evaluated by calculating the levelized cost of energy (LCOE) of the stand-alone PV system. The LCOE resembles the LCOSS (explained in Section 2.6), except the system costs are evaluated only for the PV system. The LCOE of a PV system comprises the costs incurred during the lifetime of the PV system. These costs comprise the capital expenditure of the PV system ($CAPEX_{pv}$ [\$/kW]) and by discounting to the present value the OPEX of the PV system ($OPEX_{pv}$ [\$/kW]), the decommissioning costs of the PV system at the end of its lifetime ($C_{decom,pv}$ [\$/kW]), and the financing of the PV system (F_{pv} [\$]). $Capacity_{pv}$ [kW] is the capacity or size of the PV system. The amount of energy generated by the PV system (E_{pv} [kWh]), including PV system degradation (deg_{pv} [%]), is discounted for the PV system's lifetime. This is shown in Eq. 3.1.

$$LCOE(\$/kWh) = \frac{(CAPEX_{pv} + C_{decom,pv} + \sum_{n=1}^{N} \frac{OPEX_{pv}}{(1+r_n)^n}) * Capacity_{pv} + \sum_{n=1}^{N} \frac{F_n^{pv}}{(1+r_n)^n}}{\sum_{n=1}^{N} \frac{E_{pv}(1-deg_{pv})^n}{(1+r_n)^n}} \qquad (3.1)$$

For this analysis, only the monocrystalline module is included because this is the most widely used cell material in the literature (for validation purposes). The calculated LCOE of the four types of PV systems for the case study locations are presented in Table 3.4. For completeness the LCOE for the HSAT system is also included for VHF. From these results, the following can be concluded. Firstly, the location's climate has a significant impact on the LCOE of the PV system. If a PV system can generate more energy using the same module (due to irradiance), this will result in a lower LCOE. VHF is located in Fujairah, UAE, which shows a very favourable solar climate (high irradiance levels), resulting in a low LCOE. The tropical climate at Vopak Panama is also very advantageous for a PV system resulting in a slightly higher LCOE than the desert system at VHF but still low. VTL is located in a maritime climate, which is less suitable for implementing a solar PV system due to the low average irradiance levels. Thus, a higher LCOE of the PV system is calculated. Secondly, for all three locations, the system's scale affects the system's LCOE; the larger the PV system, the lower LCOE becomes. This is due to economies of scale as explained in Section 2.4.1. Thirdly, the lowest LCOE is calculated for the fixed-axis bifacial modules for all three locations. This highlights the advantageous energy gain of a bifacial module despite the slightly higher costs. Fourthly, the HSAT with a bifacial module as PV system, which can produce the highest energy yield but for significantly higher costs, is becoming a competitive alternative to the fixed-axis monofacial PV system.

Table 3.4: The calculated LCOE for the three different storage terminals, for a 1, 10, and 100 MW PV system; based on different PV systems

Location	VHF (\$/kWh)			VTL (\$/kWh)			Vopak Panama (\$/kWh)		
PV system size (MW)	1	10	100	1	10	100	1	10	100
Fixed - Monofacial - Monocrystalline	0.085	0.066	0.052	0.129	0.099	0.077	0.094	0.073	0.057
Fixed - Bifacial - Monocrystalline	0.079	0.061	0.048	0.121	0.094	0.073	0.091	0.071	0.055
HSAT - Monofacial - Monocrystalline	0.089	0.070	0.055	0.135	0.104	0.081	0.100	0.078	0.061
HSAT - Bifacial - Monocrystalline	0.086	0.067	0.053	0.130	0.101	0.079	0.097	0.075	0.059

4

Case study: Results analysis

In this chapter, the results will be covered from the Linck model for the three storage terminal locations. In Section 4.1, per storage terminal the calculated LCOSS and sizing of the different PV and battery configurations are analysed. The system with the lowest LCOSS is the chosen CRAP system. This system will be further analysed in a sensitivity analysis. In Section 4.2, the sensitivity of the system costs and the weighted average cost of capital on the system economics are evaluated as well as the sensitivity of the models and the input data for the models. Afterwards, in Section 4.3 the effect of feeding unused energy to the grid is touched upon. The PV and sizing models' outputs are in Appendix C.

4.1. System economics and sizing results

The calculated LCOSS of every system provides insight into the competitiveness of different PV and battery systems. The lowest LCOSS of the three locations is 0.33 [$/kWh] for the location at VHF, followed by the location in Panama (0.53 [$/kWh]) and the highest LCOSS is at VTL (0.96 [$/kWh]). The lowest LCOSS use a VRF battery and polycrystalline as cell material for all the system locations.

4.1.1. Vopak Horizon Fujairah

As mentioned in Section 3.1, the combination with the HSAT is not included as a system option. The results from the sizing model for VHF are shown in Figure 4.1, and Figure 4.2 provides an overview of the calculated LCOSS of the different PV and battery systems. Generally, the results show relatively low LCOSS values due to the constant climate of high solar irradiance in Fujairah with minimal seasonal variation. This results in a constant PV energy yield throughout the year, as shown in Appendix C.1; thus, the battery system must only be sized to satisfy the daily energy demand with storage and does not need to provide long-term storage. This results in a PV system which is less oversized, reducing the overall amount of dumped energy. Additionally, due to the scale of the system, it can profit from cost reduction, resulting in overall lower PV system and BESS costs. The calculated LCOE (see Table 3.4), with an estimated 0.048–0.055 [$/kWh] for a 100 MW system, clarifies that the LCOSS values are strongly determined by the battery system costs and the amount of energy dumped.

Based on the results, using a bifacial rather than a monofacial module results in a higher energy yield, resulting in a decrease in the PV size and a slight decrease in battery size. The bifacial gain outweighs the more expensive system costs, resulting in a slightly lower LCOSS. Furthermore, the LCOSS of the VRF is generally lower than the Li-ion battery system due to the advantageous technical properties (SOC limits, cycle life), resulting in lower replacement costs despite the relatively higher initial investment costs. The lowest LCOSS is 0.33 [$/kWh], with a 108.6 [MW] fixed bifacial polycrystalline PV system and a 416.0/52.0 [MWh/MW] VRF battery. The PV system [MW] is roughly twice the size of the battery [MW], with 48% of the excess energy generated being dumped. This is still a high percentage but shows the potential if this dumped energy is used, lowering the LCOSS.

	Battery type	PV (MW)	Li-ion (MWh/MW)	PV (MW)	Li-ion (MWh/MW)	PV (MW)	VRF (MWh/MW)	PV (MW)	VRF (MWh/MW)
	Storage duration (hours)		4		8		4		8
PV System	Fixed - Monofacial - Polycrystalline	118.2	532.4/133.1	118.1	541.6/67.7	120.2	416.4/104.1	116.3	434.4/54.3
	Fixed - Monofacial - Monocrystalline	118.2	532.4/133.1	118.1	541.6/67.7	120.2	416.4/104.1	116.3	434.4/54.3
	Fixed - Bifacial - Polycrystalline	109.1	525.2/131.3	110.7	524.8/65.6	110.4	412.8/103.2	108.6	416.0/52.0
	Fixed - Bifacial - Monocrystalline	109.1	525.2/131.3	110.7	524.8/65.6	110.4	412.8/103.2	108.6	416.0/52.0

Figure 4.1: The calculated sizing for VHF in [MW]; the blue cell is the system with the lowest LCOSS

	Battery type	($/kWh)		VRF LCOSS ($/kWh)	
	Storage duration	4 Hours	8 Hours	4 Hours	8 Hours
PV system	Fixed - Monofacial - Polycrystalline	0.52	0.49	0.40	0.34
	Fixed - Monofacial - Monocrystalline	0.52	0.49	0.40	0.35
	Fixed - Bifacial - Polycrystalline	0.51	0.47	0.39	0.33
	Fixed - Bifacial - Monocrystalline	0.52	0.48	0.40	0.33

Figure 4.2: The calculated LCOSS for VHF; the blue cell is the system with the lowest LCOSS

4.1.2. Vopak Terminal Laurenshaven

The climate in the Netherlands, where VTL is located, strongly influences the LCOSS of the system. Firstly, the amount of energy generated is generally relatively low compared to the other two locations. Secondly, the energy yield results (in Appendix C.2) show a strong seasonal variation in the amount of energy generated in the winter (lower) and in the summer (higher). This difference in seasonal energy yield causes the system to be oversized to satisfy the load both daily and seasonally. It can satisfy the load by either increasing the battery size, which is expensive, or increasing the PV system size, which is cheaper but results in a system with a large amount of dumped (unused) PV energy. This second option was chosen, as shown by the sizing ratio of the PV-to-battery system (five times higher for the lowest LCOSS system). Furthermore, based on the system size, it can only profit from intermediate-scale advantages, limiting the potential cost decrease. An overview of the sizing of the system is shown in 4.3, and the LCOSS values of the different system combinations are shown in Figure 4.4.

In general for VTL, the results show that if the energy gain of the PV technology outweighs the costs, the system results in a lower LCOSS. This is the case for both the bifacial and HSAT configuration. Additionally, it highlights that if a location in a generally low level of irradiance climate, needs to select a PV system, the system with the highest energy yield for the autonomous system is chosen. The additional PV energy results in a smaller battery size, which is the main cost factor of the LCOSS. Thus, resulting in a lower LCOSS. Furthermore, the results show that the bifacial module has a higher impact on the LCOSS than using a tracking system compared to a fixed monofacial system. The additional costs of using a bifacial system are lower than for the tracking system, despite the higher additional energy yield of the tracking system.

The lowest-cost option for an autonomous system for VTL is a 16.6 [MW] HSAT bifacial polycrystalline PV system with a 28/3.5 [MWh/MW] VRF battery. The LCOSS of this system is 0.96 [$/kWh]. For the lowest LCOSS, the size of the PV system is almost five times the battery size. The PV system is extremely oversized; therefore, almost 70% of the energy is dumped, resulting in a very high LCOSS. Based on the calculated LCOE of 0.101 [$/kWh] for the same PV system of 10 MW (see Table 3.4), the effect of the battery system and the amount of energy dumped is evident on the LCOSS.

The systems with a VRF battery have a lower LCOSS than those with a Li-ion battery system. Generally, a VRF battery is smaller than a Li-ion battery, whilst the PV system size remains the same or is slightly higher due to the advantageous SOC limits of the VRF battery. Furthermore, the VRF battery must be replaced less often, reducing capital expenditure costs. This reduces the total system costs and thus the LCOSS. Furthermore, from the results it is evident that when the storage duration of the VRF battery increases, the LCOSS ([$/kWh]) decreases.

Battery type	PV (MW)	Li-ion (MWh/MW)	PV (MW)	Li-ion (MWh/MW)	PV (MW)	VRF (MWh/MW)	PV (MW)	VRF (MWh/MW)
Storage duration (hours)		4		8		4		8
Fixed - Monofacial - Polycrystalline	20.5	52.0/13.0	21.1	47.2/5.9	22.1	33.6/8.4	21.1	37.6/4.7
Fixed - Monofacial - Monocrystalline	20.5	52.0/13.0	21.1	47.2/5.9	22.1	33.6/8.4	21.1	37.6/4.7
Fixed - Bifacial - Polycrystalline	19.7	36.4/9.1	19.9	35.2/4.4	19.9	28.0/7.0	19.2	31.2/3.9
Fixed - Bifacial - Monocrystalline	19.7	36.4/9.1	19.9	35.2/4.4	19.9	28.0/7.0	19.2	31.2/3.9
HSAT - Monofacial - Polycrystalline	19.0	34.0/8.5	19.1	33.6/4.2	19.4	25.6/6.4	19.0	27.2/3.4
HSAT - Monofacial - Monocrystalline	19.0	34.0/8.5	19.1	33.6/4.2	19.4	25.6/6.4	19.0	27.2/3.4
HSAT - Bifacial - Polycrystalline	16.6	35.2/8.8	16.6	35.2/4.4	17.1	26.0/6.5	**16.6**	**28.0/3.5**
HSAT - Bifacial - Monocrystalline	16.6	35.2/8.8	16.6	35.2/4.4	17.1	26.0/6.5	16.6	28.0/3.5

(The leftmost column is labelled "PV System" vertically.)

Figure 4.3: The calculated sizing in [MW] for VTL; the blue cell is the system with the lowest LCOSS

Battery type	($/kWh)		VRF LCOSS ($/kWh)	
Storage duration	4 Hours	8 Hours	4 Hours	8 Hours
Fixed - Monofacial - Polycrystalline	1.66	1.45	1.29	1.18
Fixed - Monofacial - Monocrystalline	1.68	1.48	1.31	1.20
Fixed - Bifacial - Polycrystalline	1.28	1.18	1.12	1.03
Fixed - Bifacial - Monocrystalline	1.31	1.21	1.14	1.05
HSAT - Monofacial - Polycrystalline	1.26	1.18	1.10	0.95
HSAT - Monofacial - Monocrystalline	1.29	1.20	1.12	0.97
HSAT - Bifacial - Polycrystalline	1.25	1.17	1.07	**0.96**
HSAT - Bifacial - Monocrystalline	1.27	1.19	1.09	0.99

(The leftmost column is labelled "PV system" vertically.)

Figure 4.4: The calculated LCOSS for VTL; the blue cell is the system with the lowest LCOSS

4.1.3. Vopak Panama

The LCOSS of Vopak Panama is also influenced by the climate. The climate is constant in Panama despite the seasonal period of rainfall. This is reflected in the energy yield during the year, as shown in Appendix C.3. Therefore, the system does not need to be sized based on the seasonal energy output of the system. Thus, the system must only be sized based on the daily energy load fluctuation, which results in an overall lower amount of energy dumped. Furthermore, the average energy yield is generally reasonable, resulting in a relatively lower LCOSS compared to VTL. However, the size of the necessary PV system is moderate, which does not enable profiting from the scaling factors of the PV and battery system. However, similarly, as with the other two systems, the LCOE (see Table 3.4) is much lower than the lowest LCOSS, highlighting the effect of unused energy and the cost of the battery influencing the LCOSS of the system. Figure 4.5 provides an overview of the sizing of the different system combinations. The corresponding LCOSS values of the different systems are given in Figure 4.6.

For an autonomous system, the system with the lowest LCOSS is a 17.1 [MW] fixed bifacial poly-crystalline PV system with a 52.0/13.0 [MWh/MW] VRF battery. The LCOSS of this system is 0.53 [$/kWh]. A 10 MW system using a bifacial fixed system shows a LCOE of 0.090 [$/kWh] (see Table 3.4, illustrating the impact of the amount of dumped energy and battery system costs on the LCOSS. On average, the PV system configurations with a fixed system have a lower LCOSS than the HSAT. The additional energy yield of the tracking system do not outweigh the additional costs.

The VRF battery with 4 hour storage results in the lowest LCOSS of the system. A VRF battery is expected due to the technical capabilities and minimal replacement costs. However, based on the sizing results which are determined by the energy management strategy as well as other factors, that a VRF with 4 hour storage duration is more cost-effective than a VRF with 8 hours of storage. This is realized by increasing the PV system size to reduce the size of the BESS. Ultimately, resulting in a system with the lowest LCOSS.

The systems using a bifacial module have a lower LCOSS than those with a monofacial module because the energy gain exceeds the additional costs. When a bifacial module is used with a VRF battery with a storage duration of 4 hours, the LCOSS is lower than with a VRF battery with a storage duration of 8 hours. This is likely because the size of the VRF battery with 8 hours storage duration decreases minimally compared to the 4-hour VRF battery.

	Battery type	PV (MW)	Li-ion (MWh/MW)	PV (MW)	Li-ion (MWh/MW)	PV (MW)	VRF (MWh/MW)	PV (MW)	VRF (MWh/MW)
	Storage duration (hours)		4		8		4		8
PV System	Fixed - Monofacial - Polycrystalline	10.3	104.4/26.1	10.2	104.8/13.1	13.0	70.4/17.6	10.1	83.2/10.4
	Fixed - Monofacial - Monocrystalline	10.3	104.4/26.1	10.2	104.8/13.1	13.0	70.4/17.6	10.1	83.2/10.4
	Fixed - Bifacial - Polycrystalline	9.6	104.0/26.0	9.6	104.0/13.0	17.1	52.0/13.0	9.4	83.2/10.4
	Fixed - Bifacial - Monocrystalline	9.6	104.0/26.0	9.6	104.0/13.0	17.1	52.0/13.0	9.4	83.2/10.4
	HSAT - Monofacial - Polycrystalline	10.2	106.8/26.7	10.0	106.4/13.3	12.8	74.8/18.7	9.9	83.2/10.4
	HSAT - Monofacial - Monocrystalline	10.2	106.8/26.7	10.0	106.4/13.3	12.8	74.8/18.7	9.9	83.2/10.4
	HSAT - Bifacial - Polycrystalline	9.3	106.4/26.6	9.3	106.4/13.3	17.0	51.6/12.9	9.3	84.0/10.5
	HSAT - Bifacial - Monocrystalline	9.3	106.4/26.6	9.3	106.4/13.3	17.0	51.6/12.9	9.3	84.0/10.5

Figure 4.5: The calculated sizing in [MW] for Vopak Panama; the blue cell is the system with the lowest LCOSS

	Battery type	($/kWh)		VRF LCOSS ($/kWh)	
	Storage duration	4 Hours	8 Hours	4 Hours	8 Hours
PV system	Fixed - Monofacial - Polycrystalline	0.93	0.85	0.64	0.59
	Fixed - Monofacial - Monocrystalline	0.93	0.86	0.65	0.59
	Fixed - Bifacial - Polycrystalline	0.92	0.85	0.53	0.59
	Fixed - Bifacial - Monocrystalline	0.93	0.85	0.53	0.59
	HSAT - Monofacial - Polycrystalline	0.96	0.88	0.69	0.60
	HSAT - Monofacial - Monocrystalline	0.97	0.88	0.70	0.61
	HSAT - Bifacial - Polycrystalline	0.96	0.75	0.54	0.60
	HSAT - Bifacial - Monocrystalline	0.96	0.75	0.55	0.61

Figure 4.6: The calculated LCOSS for Vopak Panama; the blue cell is the system with the lowest LCOSS

4.2. Sensitivity analysis

As explained in the previous section, the calculated systems are very sensitive to the location's meteorological conditions as this influences the sizing of the system and thus the economic feasibility. Furthermore, the models are based on specific technological assumptions, assumed data and the economic environment. Therefore, there is quite a lot of uncertainty in their predictions. A better understanding is developed of the competitiveness of the calculated LCOSS by conducting a sensitivity analysis for the lowest LCOSS system of each location. In Section 4.2.1, a sensitivity analysis is carried out for the main cost components of the system. The model's sensitivity to the WACC is examined in Section 4.2.2. Additionally, in Section 4.2.3 the sensitivity of the models are evaluated. Finally, the sensitivity of the input data for the models are described in Section 4.2.4.

4.2.1. Sensitivity to the cost components

The cost assumptions for the PV and battery system used in the cost model are from 2020. Due to economies of scale and technological progression, these technologies' costs are expected to decline. However, political warfare (e.g. war in Ukraine), supply chain issues, scarcity of raw materials, and other social and economic developments can cause the price of some of these technologies to rise. The total investment (including replacement), decommissioning cost and the O&M costs for the PV system and battery system, and the combined system costs are multiplied by values between 0.5 and 1.5 to simulate an increase and decrease in cost to develop a broader understanding of the impact of cost uncertainty on the LCOSS of the system. The sensitivity of the cost components is graphically shown in Figure C.6.

This analysis shows an almost linear trend because the sizing is assumed to stay the same. The results highlight the effect of increasing/decreasing the PV and battery cost components on the calculated LCOSS. However, in reality, the costs influence the sizing of the system, the costs and the sizing together influence the LCOSS of the system. Therefore, if the cost components change, it can affect the sizing and, thus, the calculated LCOSS. Resulting in an alternative LCOSS for different PV systems and BESS combinations and a (possibly) different CRAP system with the lowest LCOSS. Unfortunately, this effect has not been included in this analysis. Nevertheless, what can be expected is that if only the battery system costs decrease, the size of the battery will increase, and the size of the PV will decrease. If only the costs of the PV system further decrease, a minimal to some decrease in PV size is expected. This is because, from the results, it is clear that the current costs of the battery are

two to three times higher than the PV system; therefore, these PV systems are generally stretched to the limit in PV size. Cost reduction of the PV system will reduce the costs, not necessarily the sizing. Suppose both PV system costs and BESS costs are reduced. In that case, the effect will be that the sizing will be more balanced in ratio because the cost reduction of the battery system will significantly influence the system's total costs, resulting in a reduction of the PV size and an increase in the battery size.

Based on this cost sensitivity analysis, the following can be concluded. Firstly, the battery costs strongly impact the LCOSS. For VHF, where the PV system is 2.1 times the size of the battery, a 50% decrease in battery costs results in a 38% decrease in the LCOSS to 0.20 [$/kWh]. Conversely, a 50% decrease in the PV system only decreases the LCOSS by 12% to 0.29 [$/kWh]. The same can be concluded for the cost sensitivity of Vopak Panama, which has a PV-to-battery ratio of 1.3 to 1, where a 50% decrease in battery costs results in a 37% decrease in the LCOSS to 0.33 [$/kWh], while a 50% decrease in PV costs results in a 14% decrease in the LCOSS to 0.45 [$/kWh]. It is therefore more important to focus on cost reduction in the battery system to realize a lower LCOSS. Secondly, the ratio of the PV-to-battery system influences the importance of the different cost components. This is shown in the sensitivity for VTL, where the PV system is almost five times larger than the battery system; in this case, the PV and battery systems have more or less the same effect on the LCOSS.

A more realistic cost reduction is also added in the analysis (see figures below) to indicate the estimated LCOSS in 2030 for the same system sizing. Based on the report from DOE (n.d.), a 50% cost reduction is expected in 2030 from 2021 for the installation capital costs, O&M costs and decommissioning costs of a PV system. A cost reduction of 20% is estimated for the capital investment of a VRF battery, and a 10% cost reduction of the O&M costs and decommissioning costs between 2020 and 2030 (Viswanathan et al., 2022). Based on these reduction values, it is clear that to make autonomous PV and battery systems even more cost-effective, the costs of the BESS need to decrease further to become competitive with current fossil-fuel-generated energy.

(a) Vopak Horizon Fujairah

(b) Vopak Terminal Laurenshaven

(c) Vopak Panama
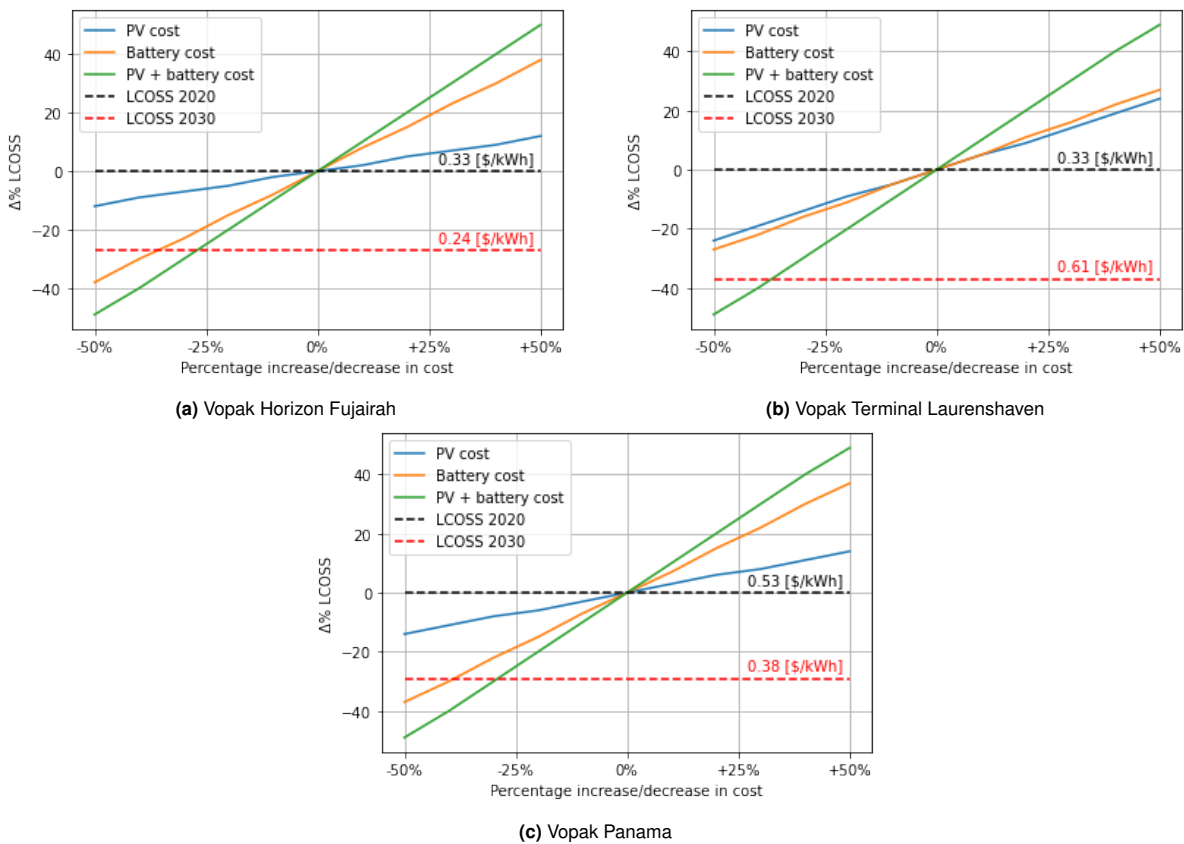
Figure 4.7: Percentage change in the LCOSS caused by changing the cost components of the system for all three locations. Created by running the model with an increase/decrease of 10%, 20%, 30%, 40% and 50% in costs

4.2.2. Sensitivity to the weighted average cost of capital

The sensitivity of the calculated LCOSS to the WACC is examined in this section. The WACC is briefly explained in Section 2.4. The WACC represents the interest to be paid over the loan for the proposed project. This value provides an understanding of the riskiness of an investment. A low value of 5% or even 3% indicates that minimal risk is involved. The probability that the moneylenders will be repaid is high; therefore, they do not need to charge high interest to compensate for this insecurity. Projects posing a low risk comprise well-proven technologies in stable countries with reliable companies. The calculation method used by Vopak for the WACC is confidential and country-dependent. The calculated WACC is 8.5% for VHF, 5.7% for VTL, and 8% for Vopak Panama. Based on these calculated WACCs, it can be concluded that Vopak views VHF and Vopak Panama as high-risk investment locations. Figure 4.8 shows the difference between the currently calculated WACC (light blue bar) and when the WACC is assumed to be lower or higher (dark blue bar). Evidently, lowering the WACC significantly impacts the LCOSS. Therefore, it is beneficial to keep it as low as possible. It can be concluded that a difference in the WACC of 2% has approximately the same effect as a cost reduction in the PV system and battery system of 10%–15%. This highlights the importance of a safe investment climate to develop the cheapest possible system.

(a) Vopak Horizon Fujairah

(b) Vopak Terminal Laurenshaven

(c) Vopak Panama
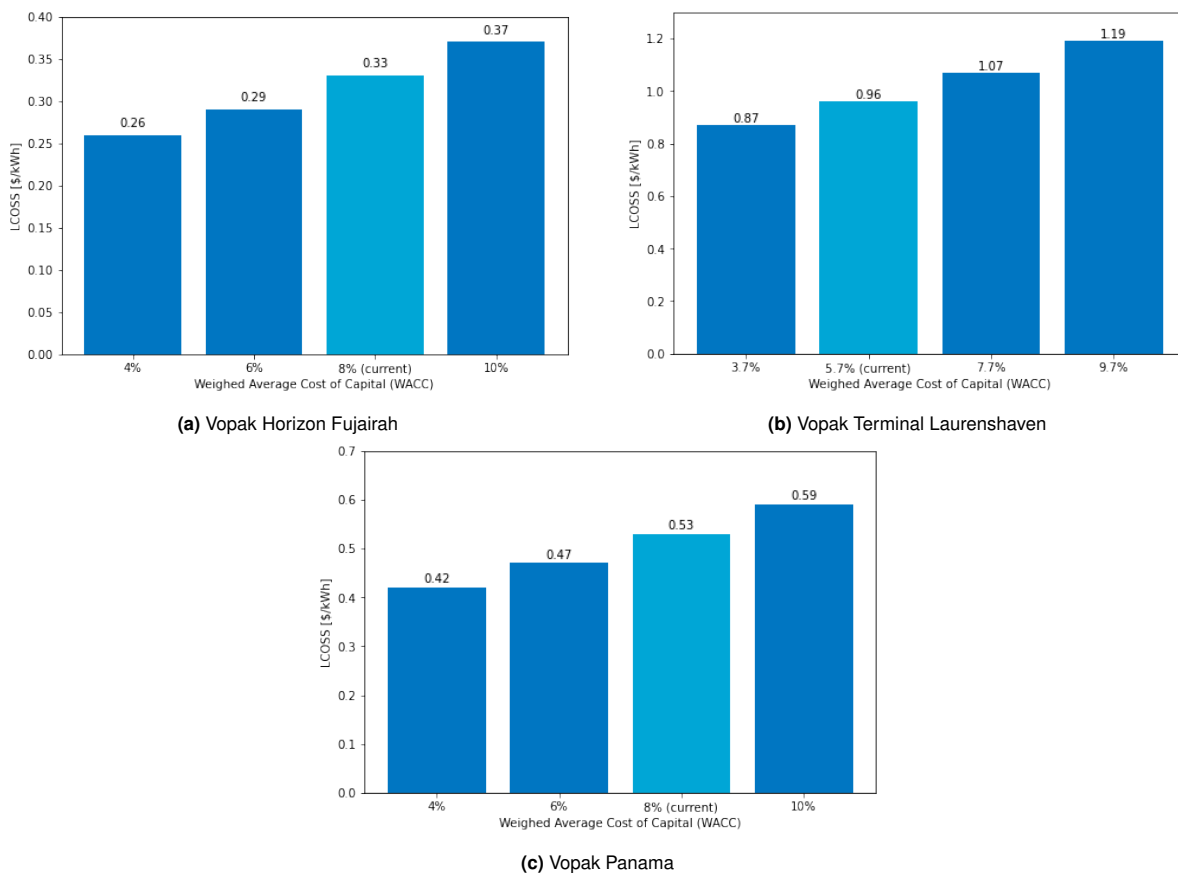
Figure 4.8: Sensitivity analysis of the LCOSS with varying WACC for all three locations created by running the model with different WACC values.

4.2.3. Sensitivity of the models

The PV and sizing models' accuracy affects the final results. Firstly, the sensitivity of the PV model depends on three main factors: (a) the chosen meteorological data, (b) the calculation method (irradiance models, programming functions, classes etc.) and (c) the selected system losses. To validate this PV model, the results from this model are compared with the well-known "PVGIS" (2022) model. The values from PVGIS have, on average, a higher amount of irradiance. The amount of irradiance a system can receive determines the PV power output resulting in a specific sizing. The extracted meteorological data influences the amount of irradiance as input for the model. This model uses Meteonorm data (as

explained in Section 2.3.1). Meteonorm uses a combination of measured and modelled solar radiation data by interpolating long-term monthly averages. Whilst PVGIS uses solar radiation data calculated from satellite images.

Both models use Perez et al. (1987) diffuse model to calculate the Global Tilted Irradiance (GTI) on the optimally tilted surface. GTI is the sum of the scattered, direct and reflected irradiance. There is a difference in the way temperature losses are included in both models. PVGIS uses a fixed percentage of losses for the temperature variation. The PV model uses a variable temperature loss factor based on variable temperature, irradiance, wind speed and chosen mounting structure. Furthermore, the inputs which are considered system losses are different. Thus, this can impact the final PV power output. In Table 4.1, the comparison between the two models is presented for a fixed-tilted monofacial system. A third AC Power output from an external source is added for extra comparison to validate the PV model. These results show a maximum deviation of less than 5% for AC PV power output compared to the other model and sources. This is acceptable because a limit of 5% tolerance is also used for the industry's output power labelling of PV modules, according to IE (2010).

Table 4.1: Accuracy comparison of the PV model and PVGIS model ("PVGIS", 2022)

Location	Fujairah			Laurenshaven			Panama		
Model	PV model	PVGIS	$\triangle$%	PV model	PVGIS	$\triangle$%	PV model	PVGIS	$\triangle$%
Annual GTI (kWh/m2)	2047	2234	9.1	1044	1284	23.0	1708	1797	5.2
AC Power output (kWh/kWp)	1570	1606	2.3	883	920	4.2	1372	1335	2.7
	1598 (Das, 2014)		1.8	901 (Smets et al., 2016)		2.0	1400 (World Bank Group, 2022)		2.0

The sizing model's sensitivity is determined by two factors: the energy management system strategy and the step size of the grid-search method. Firstly, the energy management strategy sizes a system based on data for an entire year (8760 hours). Thus for the system to be autonomous, the PV system and battery system need to satisfy the load for all 8760 hours. If the sizing would be based, for example, on a "worst case scenario week", a completely different sizing would be realized (this has not been simulated in this study). Secondly, the sizing uses the grid-search system selection method and includes all system configurations based on the predetermined step size. This model uses $\triangle = 0.1$. A more accurate result is received if a smaller step is taken, resulting in a possibly lower or higher sizing and LCOSS. Table 4.2 shows the effect of a smaller step size on the final sizing output for the lowest LCOSS system configuration for VTL. In this case, a smaller PV system size is calculated if a step size of $\triangle = 0.05$ is selected. Obviously, a higher sizing could have also been calculated for a different scenario. However, for Vopak an accuracy of $\triangle = 0.05$ is not necessary; therefore, $\triangle = 0.1$ is chosen for the sizing model.

Table 4.2: The effect of increasing the step size resolution of the grid-search system selection method for the lowest LCOSS system configuration of VTL

Step size	$\triangle$=1	$\triangle$=0.5	$\triangle$=0.1	$\triangle$=0.05
PV size (MW)	17	16.5	16.6	16.55
Battery size (MWh)	32	32.0	28.0	28.00

4.2.4. Sensitivity of the input data

The sensitivity of the input data in the models is firstly determined by the source that delivers the data and their sensitivity, e.g. Meteonorm and their measuring techniques of weather data. Secondly, the time interval used for the input data, for example, the weather data used for the PV model, uses average hourly intervals. The weather data determines the energy yield of the different PV systems. The weather variable with the strongest influence on the power is the irradiance, power generally increases with increasing irradiance. Consequently, the distribution of power typically resembles the distribution of irradiance. Hansen and Stein (2012) researched the time-effect on the analysis of a PV system. This study illustrated the distribution of using a smaller time interval for the irradiance and corresponding power output, the results are shown in Figure 4.9. Based on these results, a higher time interval (more

counts) resulted in a 0.6% higher energy output (calculated using the midpoint-rule), illustrating the effect of the chosen time interval on the final power output.
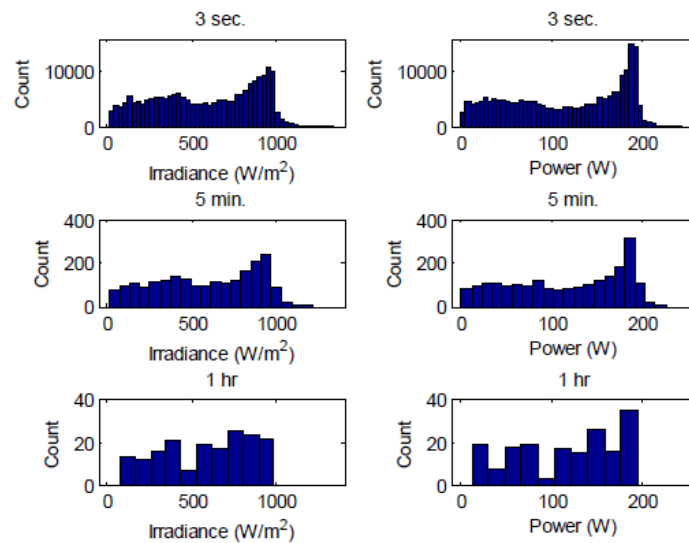
Figure 4.9: Distribution of measured irradiance [W/m^2] and modeled power for a 3-seconds, 5-minutes and 1-hour intervals (Hansen & Stein, 2012)

The sizing model is determined by the time interval of the PV model and the time interval of the storage terminals' load to calculate the amount of excess energy. Increasing the time interval accuracy (hours to minutes) of both data inputs results in a system that can more realistically determine the system's excess, dumped, and unmet energy. Therefore, a system can be sized with a higher accuracy.

4.3. Effect of grid-feeding on the system

The calculated LCOSS so far are all for an autonomous system. The system is entirely independent and does not need a secondary energy source or the grid to satisfy the load of the storage terminal. However, this does result in a system with a high amount of dumped energy, thus the system does not use its full energy generating potential. Therefore in this section, an analysis is conducted to understand the effect of integrating the system with the grid to only feed the dumped energy to the grid. In this analysis, it is assumed that the system operates using the "standard grid-feeding method". In this configuration, the solar energy is first used to supply the load and charge the battery. Excess energy that is not used (dumped) is sold to the grid. In this study, only the effect of selling the dumped energy to the grid is analyzed thus the size of the system stays the same.

In Western-Europe, energy is normally traded on the day-ahead market. This market is very volatile and dependent on multiple factors, as well as very specific for the Western-European market. Therefore, for this study it is assumed that the dumped energy is sold to the grid using feed-in tariffs. The feed-in tariff is a policy designed to stimulate the generation of renewable energy by providing producers with a fixed and guaranteed price often related to the economic lifetime of the project (usually 15-25 years). The feed-in tariffs are usually paid by electricity grid, system or market operators, often in the context of Power purchasing agreements (PPA). Thus the price of the feed-in tariff in these PPAs strongly determine the LCOSS. To understand the impact of the feed-in tariff price, three different price scenarios are examined. The first scenario is the "worst case" scenario, which corresponds to a low average feed-in tariff price for electricity. The second scenario is the "base-case" scenario, which assumes an intermediate feed-in tariff price for electricity. The "best case" scenario is the third scenario, with a feed-in tariff price based on the average selling price caused by the current energy crisis. There are also advantageous tax regulation for systems that consume their own electricity, this has been disregarded in this analysis.

In this analysis, it is assumed that the dumped energy is sold using a feed-in tariff in the form of a PPA. Table 4.3 shows the PPA price of utility-scale solar system for the locations of the three storage terminals. The PPA price is confidential between producer and buyer, thus the provided PPA price values are estimates and based on news articles. The PPA prices in the table are relatively low compared to the LCOE calculated for the PV systems, because PPAs are often contracted with very large PV systems (more than 100 MW). But it does provide a realistic impression of prices being paid for long-term contracted solar energy. The PPA price difference between worst and best case scenario is the largest for VTL, because the Netherlands is more dependent on other countries (Russia) for its energy, this is reflected in the high energy prices in the current energy crisis. Furthermore, the general price is higher because of the low energy yield of the PV systems. United Arab Emirates (UAE) produces its own energy and is therefore less dependent on other factors, then its own energy capacity. Additionally, the UAE have very favourable solar conditions for PV systems, and PV energy systems have been implemented on a massive scale thus the difference between worst and best case scenario is minimal. The energy prices in Panama are also relatively stable, this is reflected in the price difference between best and worst case scenario with also a relatively advantageous PV energy yield.

Table 4.3: Price purchase agreement price of utility-scale solar for the location of the storage terminals (Apostoleris et al., 2021; Greentech Media, 2018; LevelTen Energy, 2022)

Scenario	Price purchase agreement price of solar utility scale ($/kWh)		
	VHF	VTL	Vopak Panama
Worst	0.015	0.030	0.020
Base	0.025	0.050	0.035
Best	0.035	0.070	0.050

If the system was not autonomous, the system would also buy energy from the grid. Buying and selling of unused energy normally use optimisation algorithms to charge and discharge the energy. It aims to maximize revenue by selling energy when the price is high (high demand) and minimize selling the energy, if the selling price is under the operational cost of energy of the system. Likewise, the system will try to minimize buying energy from the grid if it is more expensive than the cost of energy of the system and try to buy energy from the grid for the lowest price. This study has not included a charge/discharge optimisation because it is out of the scope of this research. If an optimised buying and selling algorithm is implemented it strongly influences the sizing of the system and likely results in a lower LCOSS (depending on the market price). The sizing and the LCOSS of the system depends on the amount of energy contracted with the grid operator. The larger the contract with the grid, the more dependent the system becomes of the buying and selling price of the grid, but it does lower the sizing of the current autonomous PV and battery system.

Furthermore, this analysis makes the following assumptions. Firstly, energy sold to the grid suffer from 6% distribution and transportation losses, based on the average losses calculated for 27 European countries from CEER (2017). Secondly, it is assumed that policy allows integration with the grid. For example, for Vopak Horizon Fujairah storage terminal, located in the United Arab Emirates producing own energy and selling it to the grid is prohibited for private companies, to prevent accumulation of the grid. Thirdly, it is assumed that the feed-in tariff is fixed for the entire lifetime of the system (25 years). Fourthly, the additional costs of grid integration with the system are excluded in this analysis.

Figure 4.10 shows the LCOSS results of feed-in grid integration for the different price scenarios from Table 4.3, based on the fore-mentioned assumptions. The LCOSS for VHF decreases by 66% from 0.33 [$/kWh] to 0.111 [$/kWh] for the "base case" price scenario. For VTL the autonomous LCOSS (0.96 [$/kWh]) decreases with 90% to 0.092 [$/kWh] for the "base case" price scenario. The LCOSS of Vopak Panama for the autonomous system is 0.53 [$/kWh], which shows a decrease of 70% to 0.156 [$/kWh] for the LCOSS of "base case" price scenario. From these results, firstly it is clear that enabling the system to sell the dumped energy increases the amount of energy that can be used, resulting in a lower LCOSS. Secondly, the PPA price of a location has a major effect on the calculated LCOSS. For VTL, the "worst case" scenario and "base case" scenario are almost the "best case" for VHF and Vopak Panama. If the system can receive a higher price, it can generate more revenue which lowers the

LCOSS. Thirdly, the sizing strongly effects the decrease of the LCOSS. From the results is is clear that VTL has the biggest decrease in the LCOSS this is because the sizing of the lowest LCOSS system is very inefficient with an extremely high level of dumped energy due to the seasonal variation of the location. Therefore, if this system can sell this dumped energy, the LCOSS has a higher decrease. VHF and Vopak Panama are more efficiently sized systems because they only need to satisfy the daily energy demand, therefore less energy is dumped. Thus the difference between an autonomous system and a system which can feed the dumped energy to the grid decreases less strong.

(a) Vopak Horizon Fujairah

(b) Vopak Terminal Laurenshaven

(c) Vopak Panama
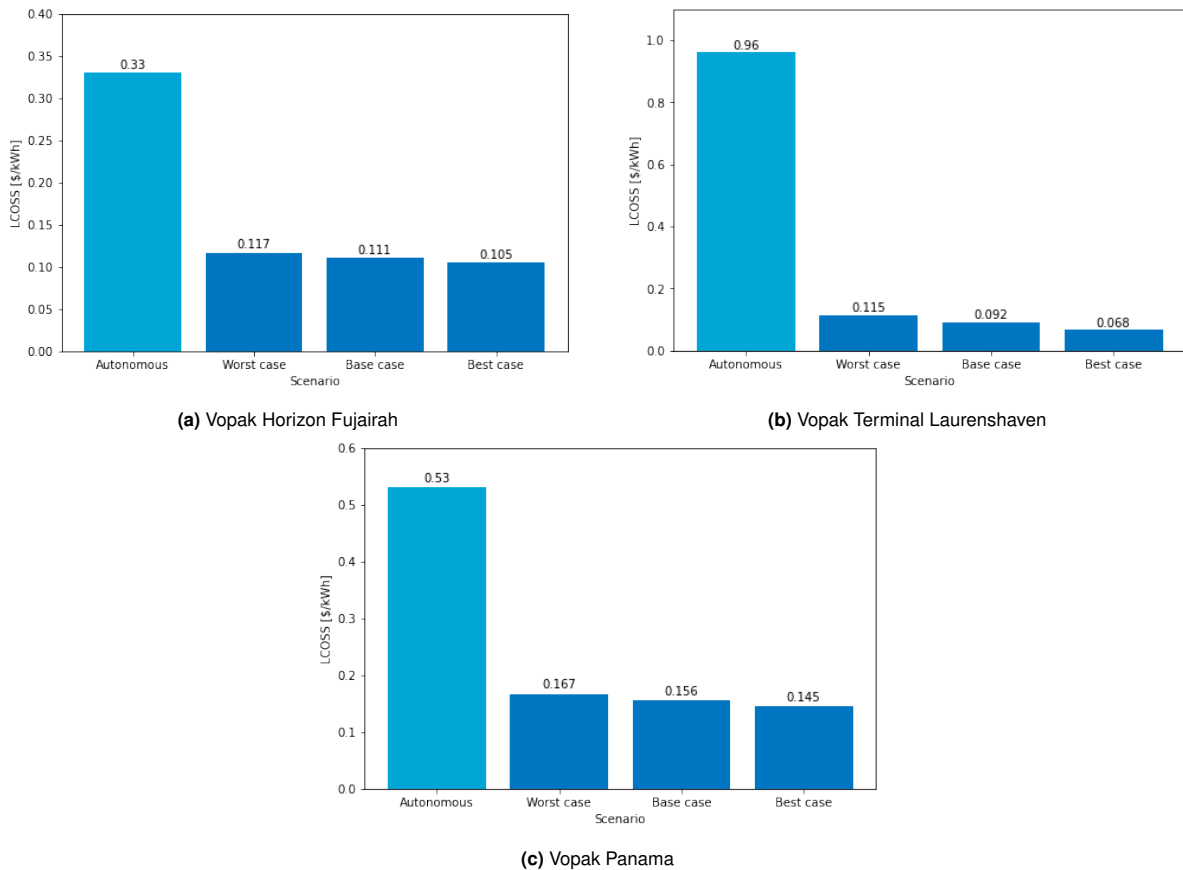
Figure 4.10: Sensitivity analysis of the LCOSS for different pricing scenarios; the light blue bar is the LCOSS of the autonomous system

5

Discussion

The results of the case study are discussed in Section 5.1, followed by a discussion of the general methodology in Section 5.2. Finally, the various limitations, assumptions and other considerations of the developed models are further reflected on in Section 5.3.

5.1. Discussion of the results

This section discusses various relations based on the case study results. The following themes are discussed: (1) the impact of climate, (2) the selected PV technology, (3) the battery choice, (4) the sizing of the system, (5) the cost-effectiveness of the system, (6) the reduction in the LCOSS, and (7) the results of feeding dumped energy to the grid.

First, a location's climate strongly impacts the calculated LCOSS. A higher irradiance level and minimal seasonal variation throughout the year result in a lower LCOSS. VHF has the lowest LCOSS and the highest irradiation with minimal seasonal variation. The highest LCOSS is calculated for VTL because irradiance in the Netherlands is the lowest of the three and shows significant seasonal variation. Therefore, the system must be oversized to compensate for a generally low energy yield and seasonal variation. Vopak Panama showed a LCOSS in between the LCOSS of VTL and VHF with an intermediate average irradiance and minimal seasonal variation.

Second, based on the selected PV technologies, the following is observed. For all three locations, the results show that polycrystalline is the cheapest option compared to monocrystalline despite having a lower efficiency. The lower efficiency is compensated for with larger panel dimensions. All these locations have sufficient land available, and Vopak has full ownership; therefore, no additional cost is incurred for the land. If Vopak did not own the land, it would need to rent (or buy) it. Thus, the larger polycrystalline module would result in a larger system and additional land costs, resulting in a possibly higher LCOSS. Additionally, all three locations select a bifacial module over a monofacial module highlighting the fact that the extra energy outweighs the additional cost. This also validates the increasing demand and potential of using bifacial modules for PV systems (Metz et al., 2017a). Based on the LCOE analysis, the bifacial modules showed the lowest LCOE compared to their monofacial counterpart; the Canadian Solar modules have a conservative bifaciality of 70%, emphasizing the potential additional gain if a module with a higher bifaciality is used. Furthermore, the tracking technology selected strongly depends on the potential additional energy yield of the technology. At VTL, the average irradiance level is relatively low, from the results it highlights the importance of a higher energy yield technology. Consequently, HSAT is the selected option due to the increased energy yield despite the additional costs. The energy gain of the HSAT for Vopak Panama is moderate, however the additional energy gain of the bifacial module outweigh the additional costs realizing the lowest LCOSS for this PV system. In this model, the fixed-axis system is assumed to be fixed throughout the year. However, by manually adjusting it during the different seasons, higher power output can be reached, improving the overall LCOSS.

Third, all the systems show the lowest LCOSS with a VRF battery. The advantageous SOC limits and the lower replacement cost due to the longer cycle life of the VRF battery compared to the Li-ion battery. This despite the lower charge/discharge efficiency and higher initial investment. Research conducted by Bruch and Müller (2014) also concluded that redox flow batteries have high financial potential due to these technical characteristics. Generally, the LCOSS of the VRF with 8 hours of storage is lower than that of a VRF with 4 hours of storage because the installed capital costs in terms of $/kWh decrease with increasing storage duration (as explained in Section 2.4.2). However, for the system at Vopak Panama a VRF with a 4 hour storage duration showed a lower LCOSS when the bifacial module is used for both fixed-axis and HSAT. This shows that the bifacial gain strongly outweighs the additional costs. Furthermore, it highlights that the bifacial gain affected the sizing from the energy management strategy to increase the PV system size and lower the battery size, which is the most costly component. A more accurate time-step or load/irradiance data may have resulted in a lower LCOSS for the VRF with 8 hours of storage.

Fourth, the load must be satisfied by the PV system and BESS for the lowest cost; thus, the system is sized accordingly. As previously mentioned, the climate and seasonal variations of the location determine the energy yields of different PV systems, which increase/decrease the PV system size. The battery system costs are much higher than the PV system costs, influencing the battery size chosen. Based on the sizing results, the system sizing strategy rather increases the PV system's size than add an additional battery to receive the lowest system costs. This results in an oversized PV system with significant (unused) dumped energy.

Fifth, the results show that all the calculated systems are not cost-effective compared to average electricity prices from the grid before the energy current crisis (see Appendix B.4). The LCOSS for the system in Fujairah is 8.3 times higher than energy taken from the grid. For VTL, this is 13 times higher, and for Vopak Panama, this is 3.0 times higher. The high LCOSS for all the systems is caused by the very high cost of the battery and the high amount of energy dumped. A system's cost-effectiveness is determined by the energy market price used for comparison. During the current energy crisis caused by the war between Russia and Ukraine, the energy spot price in August 2022 for Vopak's terminals in the Netherlands was, on average, 0.46 [$/kWh], converted using a USD/EUR rate of 1.0119 (Vopak, 2022). In this case, the designed autonomous system in Laurenshaven becomes more attractive at being only 2.1 times more expensive than sourcing energy from the grid. If the energy prices were to increase by an additional 100%, the designed PV and battery would obviously become even more attractive for VTL. Generally, the price difference between the calculated LCOSS and the grid price is because the designed system is currently autonomous. Excess energy generated by the PV system not fed to the battery is dumped and unused. Therefore, the energy used is lower than the amount the system can potentially generate.

Sixth, based on the sensitivity analysis, it can be concluded that a cost reduction of the PV and/or battery systems significantly impact the LCOSS. Mainly, the battery cost strongly influences the LCOSS; this is highlighted for the VHF and Vopak Panama systems, which show that a 50% reduction in battery cost realizes a LCOSS reduction of 37%–38%. Furthermore, developing the system in a safer investment climate reduces the WACC, decreasing the calculated LCOSS. The results show that a 2% decrease in the WACC is the same as a system cost decrease of 10%–15%. Another important factor highlighted by the LCOE analysis is that the larger the PV system, the lower its capital expenditure. Thus, reducing the LCOSS of the system. VHF is very large system and is therefore able to profit from economies of scale.

Seventh, the effect of feeding dumped energy to the grid shows very promising results based on the analysis in Section 4.3. The strongest reduction in the LCOSS is realized for VTL because of the inefficient sizing which results in a lot of dumped energy that can be sold to the grid. Additionally, the calculated LCOSS is also very dependent on the price the system is able to receive for the dumped energy. For VTL a higher estimated PPA price is paid for in the Netherlands, therefore a higher revenue can be generated. Whereas for VHF a much lower PPA price is paid for solar energy in the UAE.

5.2. Discussion of the methodology

The methodology is comprised of three components. For the PV model, programming was used to simulate the different PV systems. The PV model uses sufficient parameters and enough system settings to understand the effect of climate, seasonal variation, and technology components on the PV system. However, the model lacks the flexibility of easily selecting a location, such as established software such as PVGIS or HOMER, to automatically calculate the PV generations of different technologies. The PV model needs the user to upload weather data manually.

Although, the chosen sizing method is transparent and flexible due to the "trial and error" brute-force method, it is very time-consuming. A different sizing method, such as (non)-linear programming, could have solved this problem faster but with less transparency. The system sizing is based on calculating the lowest-cost system to satisfy the load during the entire year using a PV and battery system. The energy management strategy calculates the sizing based on a volatile load of 8,760 hours. An alternative strategy would be to split the strategy into two parts. First, a strategy could be developed that sizes the base load of the system; subsequently, a strategy could be developed to satisfy the remaining volatile peaks of the energy load. This provides additional insight for Vopak into what can easily be developed to supply a base load of energy and what in the future would be necessary for the system to be fully autonomous. Using the levelized cost of solar plus storage for the economic analysis may be a suitable method for comparing similar systems but oversimplifies project risks.

5.3. Discussion of the models

This section discusses the limitations and assumptions involved in the different models. The PV model uses technical characteristics from the manufacturer, Canadian Solar, as it is one of the few manufacturers that offers all four different types of modules (monocrystalline/polycrystalline and monofacial/bifacial). The efficiencies of these modules differ as well as the module dimensions, e.g. the polycrystalline module with a lower efficiency, is slightly larger in size than the monocrystalline module (higher efficiency). Therefore, the overall energy yield difference between the module is minimal, simplifying the trade-off between cost and module efficiency because the polycrystalline module is cheaper. Thus, when a system is developed where the cost of land can be neglected, the difference between monocrystalline and polycrystalline become irrelevant. However, the impact of the module size is evident when comparing the system's PV sizes [km^2]. Furthermore, the bifacial modules from Canadian Solar have a conservative bifaciality factor of 0.7. If a higher bifaciality is used, this would have resulted in a different sizing and a different LCOSS. Moreover, the inverter efficiency is based on estimating the relation by Baumgartner (2017) to calculate a single inverter efficiency. This can cause misleading results with alternating DC power outputs to convert to the final AC power output. Alternatively, implementing an inverter model that bases the AC power output on the DC power and DC voltage would provide a more precise result.

Although the energy load of the storage terminals for the Netherlands are accurately logged every hour. For storage terminals outside the Netherlands the energy load of the storage terminal is estimated per hour based on pump data. The actual energy load is however higher if it includes the other energy demands of the storage terminal, for example, the energy demand of the storage terminal office and other facilities. Thus, the storage terminals outside the Netherlands have relatively conservative system sizing.

From the analysis in Section 4.2.3 one can conclude that different PV models use different inputs, calculation methods and assumptions which can influence the final energy output. Based on the comparison, the PV model in this study shows relatively comparable results of less than 5% variation. Furthermore, using a smaller step size in the sizing model can influence the final sizing result used to calculate the LCOSS of the system.

The sensitivity of the input data described in Section 4.2.4 highlights the importance of the chosen time interval of the data. The sizing model uses an energy management system for every time step, t, which is in hours. If the load of the storage terminals were available in a higher resolution, such as minutes, with corresponding PV power data, the outcome from the algorithm would be more accurate, resulting in more accurate sizing of the PV and battery systems. The technical characteristics of the

batteries also influence the final sizing. In this model, battery degradation is accounted for by assuming that every day equals one cycle. After the maximum number of cycles, the storage block of the BESS must be replaced. Furthermore, it assumes that the batteries have no self-discharge rate. However, in reality, this is not true and must be implemented in the sizing model for a more realistic approach. An additional assumption is that the replaced batteries have the same cycle life as those batteries initially installed. However, with technological advancements, the cycle life will probably increase.

All the costs in the system calculation are assumptions based on cost data from 2020. Cost factors, especially renewable energy technologies, show strong and unpredictable/volatile behaviour. Consequently, the cost estimates could already be overhauled by rapid developments in PV and battery technology, as described in Section 4.2.1. Furthermore, the capital expenditure of the HSAT is expressed as a percentage of the CAPEX of the fixed-axis system, due to the lack of precise data available in literature. This is a fundamental assumption and not necessarily true when CAPEX values change significantly. Hence, it might be better to assume more absolute values. The PV model also uses backtracking for the HSAT. The additional cost of using backtracking has not been included in the $CAPEX_{pv}$, which may make the HSAT more expensive.

The decommissioning costs of the PV and battery systems are based on a fixed average value from the literature due to the lack of available data. In reality, these costs depend on the scale of the system. Furthermore, the method used to calculate the power density to estimate the necessary PV area used for the system is based on a rule-of-thumb method from Chakraborty et al. (2015). The calculated amount of land needed is probably larger than the actual area needed for the PV system. The area necessary for the battery system is neglected in the total system area due to the size ratio with the PV system. This should be included for a more accurate estimation of the area.

For simplicity and due to the availability of comparable finance models from Vopak, the financing method used to calculate F is the same for all locations. The financial method enforced in the Netherlands is used to calculate the corporate tax and debt payments. However, F should be calculated differently per location because countries are subject to different financial legislation. Also the model assumes a constant debt repayment structure, other structures are possible which can influence the LCOSS.

The autonomous systems generate a specific amount of green electricity and is thus issued green certificates, also known as Renewable Energy Certificates (RECs) in the US or Guarantee of Origin (GO) in Europe. These green certificates represent the environmental value of renewable energy production, which can be indirectly traded or sold, resulting in a secondary revenue stream. This was not included in the cost analysis. Furthermore, this project uses the WACC developed by Vopak for a "normal" investment as an investor. It would be better to develop/recalculate with Vopak a WACC based on a green investment or an investment in low-carbon technology. On average, the WACC is lower for such investments, reducing the LCOSS (Ameli et al., 2021). Additionally, when a country's subsidies for low-carbon-generating technology are enforced, this should also be included in the costs.

In this model, the sizing is based on an energy management system that can provide energy throughout the year. The system is not designed for certain days of autonomy for maintenance or if the PV/battery system fails. The authenticity of the system is improved by including autonomy in the sizing model or by introducing a backup energy source, such as a hydrogen-based generator, in the cost model. Furthermore, this model has not included the technical implications of dumping excess energy, such as the system overheating or causing electrical malfunction. It is assumed that when energy is not used, it is curtailed. The PV panels are effectively open-circuited, resulting in no current or power flow. Different sizing should be chosen if safety measures are included in this model (such as avoiding a battery's thermal runaway).

6

Conclusion and recommendations

In this Chapter, a conclusion is given about this study in Section 6.1. In Section 6.2, recommendations for further research are explained.

6.1. Conclusion

This study aimed to develop a methodology to evaluate the cost-effectiveness of an autonomous solar and storage system to electrify Vopak's storage terminals. The literature clarified that using CSP is not an economically viable solution due to the scale on which it must be implemented and the minimal DNI. The proposed system thus comprises a solar PV system with a BESS. After researching the cost-effectiveness and worldwide implementation of different PV technologies, the following PV system components are evaluated in the PV system: a fixed-axis or a HSAT, a monofacial or bifacial module, and a monocrystalline or polycrystalline cell material. A selection was also made of BESSs meeting the economic, technology-readiness level and large-scale technical implementation criteria: a Li-ion battery and a VRF battery with storage durations of 4 and 8 hours.

A method was developed using a TEM which calculates a system that is Clean, Reliable, Autonomous, and Payable i.e. CRAP. The TEM comprises three main components. Firstly, a PV model uses meteorological data and specific technical characteristics of a PV system to simulate the AC power output per PV system. Secondly, the system costs of the different technologies are used in a grid-search system selection method to size the lowest-cost autonomous PV and battery system. Thirdly, the sizing of the system is used to calculate the LCOSS of the combined system. The models used are user-friendly and offer flexibility, inclusiveness, and transparency.

Regarding the first sub-question to answer how a flexible sizing approach can be developed for an autonomous PV and battery system. This was realized with the grid-search system selection method that provides the user with an overview of different system configurations. Furthermore, flexibility and transparency are obtained by visualizing the different sizing possibilities and their impact on the amount of dumped energy, unmet energy, and system costs. For example, the sizing options are first shown based on the constraint of no energy being unmet; the system is then selected based on a second constraint (lowest system cost) but with a reflection of the percentage of energy dumped. Based on this sizing approach, the LCOSS of the PV and battery system is calculated.

The second sub-question asked about the effect of the costs and the WACC on the economics of an autonomous PV and battery system. Using a sensitivity analysis on the case study systems, the LCOSS was evaluated based on the variation in the system costs and the WACC. The most significant impact on the system costs is the cost of the battery, showing a 38% decrease in LCOSS with a 50% decrease in battery costs for two case study systems. Furthermore, a decrease of 2% in the WACC has the same impact as a 10%–15% decrease in total system costs.

The third sub-question asked to what extent an autonomous PV and battery system is economically viable at the storage terminals in Fujairah, Laurenshaven, and Panama. Based on the results, the lowest-cost proposed autonomous system for the three storage terminals is not economically viable. The calculated LCOSS values are, on average, 3 to 14 times higher than the average energy price taken from the grid for the storage terminal location. The cost-effectiveness of a system strongly depends on the climate and the seasonal variation of the located storage terminal, as this determines the energy yield of the PV system. Furthermore, the battery system costs are extremely high compared to the PV system. Therefore, in the sizing approach when the system is required to satisfy the load, there are two options: either (i) increasing the battery size, which is expensive, or (ii) increasing the PV size, which is cheaper but increases the amount of energy generated. This method searches for the cheapest system; thus, the latter option is selected, however this results in more unused energy.

The system only becomes a cost-effective solution with future cost reductions (i.e. lower BESS costs and/or PV system costs) or a lower assumed WACC for green investments. Furthermore, by selling unused (dumped) energy to the grid, it increases the amount of used energy generated by the system. An alternative to reduce the amount of unused energy is to add an external clean energy source, e.g. a hydrogen generator, to the system to compensate for the seasonal variation in energy output.

6.2. Recommendations

Based on the case study results, the following is recommended for an autonomous PV system and battery system to be cost-effective. Firstly, an autonomous PV and battery system should be implemented at a location with a good solar climate (high energy yield potential and minimal seasonal variation) to ensure more efficient sizing and less unused energy. Secondly, the capital investment of the battery system is currently too high at almost two to three times the capital investment of a PV system. Therefore, the sizing preference will result in a large PV system due to the lower cost. This results in dumped energy that the system cannot use. Thus, future cost reduction in the BESS can make the system more efficient, resulting in a lower LCOSS. Thirdly, to reach a lower LCOSS, the full energy-generating potential of the system needs to be realized, either by selling unused energy to the grid, feeding the unused energy to another industrial company (joint venture), or using it to power a nearby city/village. Fourthly, an alternative solution is to add a secondary energy source, e.g., hydrogen or a biomass generator, to the system, which can assist the autonomous PV and battery system during seasonal energy yield variation (winter) to satisfy the load.

The following recommendations are proposed for a future method. In this study, the system technology is scoped, essentially two types of PV tracking systems were chosen for modelling. Further investigating the implementation of a V(T)SAT, a HTSAT, and a dual-axis tracking system as a PV tracker will provide a complete analysis of the PV system that might provide the lowest LCOSS. Using alternative cell materials for the PV modules will also offer insight into other solar PV possibilities. Likewise, the potential of other large-scale battery systems as storage systems with varying storage duration should be explored.

This research was the first exploration. This study used the grid-search system selection method; however, further research should be conducted on alternative sizing methods that can obtain faster results with comparable flexibility and transparency. Future research could evaluate how this PV and battery can be sized based on efficiency, the available area for a system, or other criteria.

A further study combining a secondary renewable energy source (e.g. a hydrogen generator) with the current PV and battery system could offer a potential solution for seasonal energy yield variation. Additionally, it can operate as a backup for maintenance stops, worst-case scenarios (system failure), and dumped energy reduction. Adding this to the sizing model could provide insight into an alternative autonomous system.

The impact of interacting with the grid was shown, by selling dumped energy and reducing the LCOSS of the system. The system can still be made climate neutral by designing an optimized sizing between

PV, battery, and the grid (with green energy). Vopak will generate most of its electricity and use green electricity to and from the grid to generate income and stabilize the system (reducing the sizing of the system). Further research is needed to explore the optimal sizing of the grid integration, including an optimized buying and selling strategy for the system.

Although this study concludes that autonomous systems are currently not cost-effective, additional research is required to explore what factors would allow them to be so. Cost-effective solutions could possibly be realized by simulating different secondary energy sources for the system, researching the necessary future cost reductions in battery and PV system costs as well as different buying and selling strategies of (green) energy from and to the grid.

<div align="right">

A

</div>

Photovoltaic and battery energy storage technologies

A.1. Concentrated Solar Power

The concentrated Solar Power (CSP) concept uses mirrors to direct and reflect the Sun's solar energy from a large area to a focal region to produce heat at an applicable temperature. This energy can be directly used in heat processes or to produce electricity. Unlike PV technology, CSP systems do not work with diffused radiation, thus an area with a high percentage of clear sky and high Direct Normal Irradiation (DNI). According to Müller-Steinhagen and Trieb (2004), for CSP to be economically viable at a location, it needs a minimum DNI of 1800 KWh/m^2/year. DNI converts to energy, which converts into revenue and provides the expected return for the project.

The electricity production by CSP can be divided into two or three blocks (Baharoon et al., 2015). As shown in Figure A.1, the first block is the solar field, which consists of the (mirror) concentrator plus the receiver. This is further explained in Section A.1.1. A second block is necessary to compensate for overnight and cloudy periods so that heat can be stored by a thermal energy storage (TES) system. The different types are explained in Section A.1.2. To produce electricity a power block is needed to convert the produced heat into power, as explained in Section A.1.3. Finally, the main technical challenges of CSP plant are described in SectionA.1.4 An all-round comparison of the different CSP systems is presented in Section A.1.5.
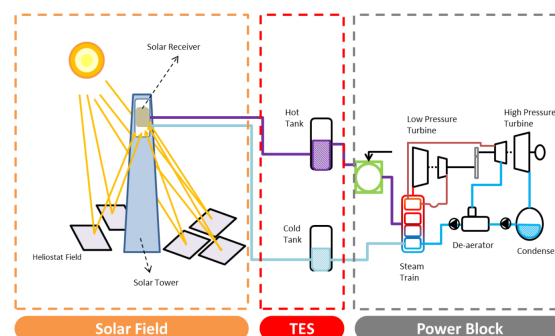
Figure A.1: Block scheme of a typical Concentrated Solar Power system (Castillo, 2014)

A.1.1. Solar field

As explained, a solar field needs to be able to concentrate photons that directly come from the Sun without being scattered by the Earth's atmosphere. The primary energy resource of the technology is direct normal irradiance, defined as the direct irradiance received on a plane normal to the sun (P. Blanc et al., 2014). As shown in Figure A.2, higher DNI values can be found in subtropic regions and/or high altitudes. A solar field can be divided into three main components:

49

- The collector uses a combination of mirrors and lenses to concentrate the radiation
- The receiver which has the function of absorbing the radiation
- The Heat Transfer Fluid (HTF) is the substance heated up in the receiver, which will act as a transport medium in the CSP system.

As shown in Table A.1, there are four different solar field types: Parabolic trough collector (PTC) and Linear Fresnel collector (LFC), Tower solar power (TSP) and Stirling dish (SD). Since the punctual concentrators potentially achieve higher concentrator factors (Romero et al., 2015), they can also be classified as medium and high-temperature technologies. The receivers that use rotation tracking are called mobile-type receivers. PTC is the most employed of these four technologies, PTC with 83% of US sales in 2018 (Visiongain, 2019). However, according to IEA (2014) it does not mean that this will be the cheapest CSP in the future because the other technologies have great cost reduction potential. Below, for each type of solar field, the technical operating of the technology, the receivers used and the (preferred) HTF is explained.
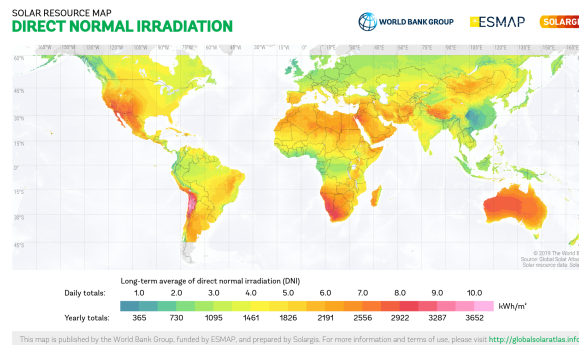
Figure A.2: World map of the long-term average DNI (World Bank Group, 2022)

	Linear Focus	Punctual Focus
Fixed type receiver	Linear Fresnel collector	Solar power-tower
Mobile type receiver	Parabolic trough collector	Parabolic dish

Table A.1: Overview of the different solar field types

Linear Fresnel collector

Linear Fresnel collector (LFC) technology uses a series of fixed long, narrow, shallow curvature (or even flat) mirrors to focus light on elevated linear tower receivers with one or more absorber tubes running parallel to the reflector rotational tracking axis. These mirrors, known as the primary reflector, act as reflectors and track the movement of the Sun by being inclined at different angles relative to the tower target. This makes it possible to use almost flat, low-cost glass mirror elements (Platzer et al., 2021). The receiver assembly includes multiple tubes and an optional secondary reflector. The secondary reflector is used to improve the overall collector performance and reduce the heat loss of the absorber. There are four classes of mirror designs using either constant or variable mirror width and varying with constant and variable gap (Montes et al., 2017) and using water as a working fluid is called direct-steam generation (DSG). A linear Fresnel system can produce steam with a temperature of 450 °C and even higher temperatures when using molten salt as fluid reaching 550 °C (Zhu, 2017). Molten salt can be used in low-cost thermal storage.

Parabolic trough collector

It a similar working as the linear Fresnel solar collector but a parabolic-trough collector (PTC) is composed of a large parabolic U-shaped concentrator that reflects direct solar radiation onto an absorber tube located in the focal line of the parabola. The collector field consists of long parallel rows aligned on a north-south axis. Therefore, the single-axis trough only needs to track the Sun from east to west throughout the day. In the focal area, the receiver tube heats the fluid that circulates through it (Moya, 2021). The limitation of this system is that the working fluid, thermal oil, known as the heat

Fluid	Advantages over thermal oil	Disadvantages compared thermal oil
Molten salt	• More efficient heat storage • Higher working temperature (>575 °C) • No pollution or fire hazard	• Higher thermal losses overnight • More complex solar field design • Higher electricity consumption
Water/steam	• Simple plant design • Higher working temperature • No pollution or fire hazards	• Lack of suitable storage system • More complex solar field control • Solar field higher pressure
Pressurized Gas	• Higher steam temperature (>500 °C) • Thermal storage enhancement • No pollution or fire hazards	• Poor heat transfer in the receiver tubes • More complex solar field control • Solar field higher pressure

Table A.2: Advantages and disadvantages of alternative fluids compared to thermal oil (Moya, 2021; Nekeman, 2014)

transfer fluid (HTF), can only deliver valuable thermal energy up to 398 °C. After this temperature, the oil degrades. Research is being conducted on new working fluids because if a higher HTF can be applied, this will mean a smaller PTC field is needed; thus, higher efficiency can be reached by the thermal generator. An overview of the advantages and disadvantages of alternative working fluids is shown in Table A.2.

Solar power-tower
A solar power-tower (SPT) system consists of many tracking mirrors or heliostats. These are spaced in a field to avoid mechanical or optical interference with one another as they pivot to reflect incident direct-beam sunlight onto an elevated receiver or secondary reflector (Hildebrandt A F & Vant-Hull, 1977). The optimal position of the central receiver (CR) is quite complicated due to the multitude of variables to be considered and the continuous variation in configuration and performance of each heliostat whilst tracking the Sun. Nevertheless, the high concentration, high temperature of heat collected and efficient collection make it very applicable for specific locations. Since the CR is fixed, this largely avoids the need for extensive energy transport networks and allows a more cost-effective investment designed to improve the efficiency and sophistication of the energy conversion process, according to Vant-Hull (2021).

There are two main types of commercial plants. The first option is distributed in a surrounding field, where the heliostats surround the central tower (CT) in a circular shape, covering 360 °. The second option is based on a polar field, where the plant covers a part of the circle in the shape of a wedge. The tower is directed somewhat downward and towards the pole to face an array of heliostats. According to Merchán et al. (2022), as latitude increases, a field which is more concentrated on the polar side of the tower reaches a higher performance. Therefore, depending on the hemisphere, a north/south polar field is preferred at higher latitudes. At the top of the tower, the reflected solar radiation reaches the receiver.

The receiver can have an external cylinder or a cavity receiver. The external cylinder contains an absorbing surface that can be seen from all directions, suitable for both surrounding and polar fields. The cavity receiver is an insulated enclosure containing an opening to receive sunlight onto a heated surface, generally used for polar fields. Cavity receivers have reduced radiative and convective heat losses compared to external receiver designs. The annual optical efficiency of a cavity receiver is typically greater (by 10% or more) than an external receiver design with a surround field (Falcone, 1986). However, cavity receivers require taller towers to absorb all the light from the heliostats field relative to a surrounding field for a given power requirement (Ho, 2017). In the receiver, water/steam, liquid sodium, molten salt, or air can be utilised as HTF for large plants with a capacity of 100–200 MW (Islam et al., 2018).

A less popular alternative is the beam-down concept. The light from the heliostats directed to the tower's (virtual) focus point is redirected towards the ground. The redirected sunlight is captured on the ground by an upward-looking receiver secondary mirror. The linear magnification (LM) is defined by the ratio of the primary and secondary mirrors. A large secondary mirror reaches a small LM, but this is more expensive to build and support. Additionally, it produces additional shading of the field (Vant-Hull, 2021).

Parabolic dish
A parabolic dish (PD) systems use mirrors mounted over a parabolic-shaped dual-axis tracking dish to focus the Sun's rays onto a receiver with an integrated Stirling engine for direct production of electricity (Berrada et al., 2021). A tracking system is used to ensure that the operator tracks the Sun bi-axially so that the optical axis of the concentrator always points to the Sun. Either an azimuth-elevation tracking, where the dish rotates in a plane parallel to the Earth's surface (azimuth) and around an axis perpendicular to it. An alternative is a polar-equatorial tracking system. The collector rotates about an axis parallel to the Earth's axis of rotation and the declination axis perpendicular to the polar axis. This combination results in maximum performance throughout the year. Due to the combination of the bi-axial concentration of Sun and bi-axial tracking results in the highest optical efficiency compared to the other CSP technologies, according to the System Advisor Model (SAM, 2020). The receiver of the system can reach surface temperatures between 750-1000 °C, according to Schiel and Keck (2021).

The high surface temperatures can result in considerable thermal losses by convection, infrared radiation and heat conduction. This is avoided by using an optimised insulated cavity receiver, which is large enough to absorb most of the concentrated sunlight but small enough to limit losses. The captured radiation as high-temperature thermal fluid is either directly converted using a receiver-mounted engine cycle or is transported to ground-based processes. Either a Brayton cycle or a Stirling cycle is used as an engine cycle. The Brayton cycle uses air as a working fluid. The Stirling engine used air, hydrogen or helium as a working fluid which is further explained in Section A.1.3. The Stirling engine is preferred due to the high efficiency (thermal-to-mechanical efficiencies over 40% have been reported), high power density (40–70 kW/L swept volume for solar engines), and potential for long-term, low-maintenance operation (Schiel & Keck, 2021).

According to Schiel and Keck (2021), dish concentrators have the highest optical efficiencies, concentration ratios, and overall conversion efficiencies of all the CSP technologies. A single parabolic dish can have a power generation capacity varying from 0.01 to 0.5 MW (Berrada et al., 2021). Despite the high conversion efficiencies when using a dish system in combination with TES, it suffers from small size with related cost drawbacks and technical challenges (Schiel & Keck, 2021). Consequently, it can only compete with PV technology, which is much cheaper to produce.

A.1.2. Thermal Energy Storage
When the solar field produces a surplus of heat not directly used by the power block to generate electricity, it can be stored using thermal energy storage (TES). This stored heat can be converted to electricity as required by demand during nighttime and periods of cloudiness. This enables the CSP plant to produce electricity each hour of every day. In Section A.1.2, the different types of storage media are explained with their corresponding advantages and disadvantages. The different storage technologies combined with a solar field are explained in Section A.1.2.

Storage media
There are two types of TES systems, sensible and latent heat storage. Worth mentioning is thermochemical storage, but this is under heavy research and development.

Sensible heat storage
Sensible heat storage stores energy based on the substance's temperature change. Thus increasing the temperature of a substance increases the energy content; when the material is cooled, the stored energy is released, but without a phase change (Caraballo et al., 2021). The choice of storage material is either liquid or solid. Solid storage materials have the advantage that they have a reduced risk of leakage and viability at very high temperatures. However, have a low heat storage density and higher thermal losses (Kalaiselvam & Parameshwaran, 2014b). The most popular materials are concrete and stable ceramic (Gil et al., 2010). As liquid media, molten salt, minerals and synthetic oils are mainly used due to for their advantages.

Latent heat storage
Latent heat storage makes use of the concept of storing capability of some substances during the phase change. This occurs at constant temperature and can involve the latent heat of phase change

during fusion (solid-liquid transition) or vaporisation (liquid-vapour transition). Substances used to store energy during the phase change are called Phase Change Materials (PCM). The main advantage of this storage process is the higher storage density. Furthermore, organic PCMs have revealed excellent thermophysical properties, melting and thermal stability, congruent freezing and non-corrosiveness (Kalaiselvam & Parameshwaran, 2014a). The main drawback is the lower thermal conductivity leading to slow charging and discharging processes and significant heat losses (dependent on the level of insulation) (Abedin & Rosen, 2011; Kuravi et al., 2013).

Thermo-chemical storage
Thermo-chemical storage makes use of the enthalpy of reaction of reversible chemical reactions. During charging, the heat produced by the solar field is used to produce an endothermic reaction. During discharge, the reverse exothermic reaction releases the needed heat. Despite thermo-chemical storage being less mature than sensible and latent heat storage, it can potentially store more energy due to the heat of reaction (Glatzmaier, 2011). The storage system enables the components to be stored separately, which causes little to no heat loss during storing period. Due to the low heat loss, this system is suitable for long-term energy storage and the high energy density relative to sensible and latent heat storage (Abedin & Rosen, 2011). Despite theoretically being very promising, further research is needed to improve the performance and implementation of the storage system. The cyclic behaviour, the degradation of thermo-chemical materials, cost, availability and durability, are challenges that need to be solved (Abedin & Rosen, 2011).

Storage technologies
There are several storage technologies commercially available, the most common systems are based on sensible heat storage: the two-tank direct and indirect systems, the single-tank thermocline storage system and the direct steam accumulator. Other TES systems are under development which involve solid, sensible heat, latent heat, and thermo-chemical. These systems have demonstrated the potential to reduce costs significantly and will likely be installed in demonstration projects in the future (IRENA et al., 2020).

Two-tank direct and indirect storage system
Two-tank direct and indirect storage systems are based on Sensible storage. In a two-tank direct system, often used with a power tower, two tanks (or two groups of tanks) store the fluid, one at a high temperature and the other at a low temperature. A pump sends fluid from the cold tank to the solar collector or receiver, where solar energy heats it. The pump then sends the hot fluid to the hot tank for storage, from where it is pumped through a power block cycle, as explained in Section A.1.3 to generate electricity. The fluid exits the power block at a low temperature and returns to the cold tank. In this case, the HTF is also the TES media in the storage system; no heat exchanger is needed leading to cost reduction.

When a two-tank indirect system is deployed in commercial parabolic trough plants, a two-tank indirect system collects solar radiation's heat and stores it in one tank. The other tank holds the storage fluid. In the loading mode, a pump sends the storage fluid through a heat exchange where heat from the fluid transfers to the storage medium that flows to the hot tank for storage. In unloading mode, the hot liquid from the tank flows through a heat exchanger and generates steam to generate electricity. The stored fluid then returns to the cold tank. The HTF is a heating fluid in the heat exchanger to heat the TES media. Indirect systems are therefore less efficient due to efficiency losses in the heat exchange process (IRENA et al., 2020).

Single-tank thermocline storage system
Thermocline storage systems consist of a single tank with the temperature of the upper portion medium-high and the temperature of the lower portion low. The transition layer, known as the thermocline, acts as a heat exchanger between the two layers. This is caused by buoyancy forces, creating a vertical stratification and narrow layer of a large temperature gradient. The temperature profile is a sigmoid-shape curve, which travels up and down the storage tank during charge and discharges (Flueckiger & Garimella, 2014). A solid filler material forming a porous packed bed in the storage tank is used through which the HTF can flow. In literature, many materials have been suggested to act as suitable fillers. The most important are rocks and silica sand which are the most attractive in terms of cost, chemical
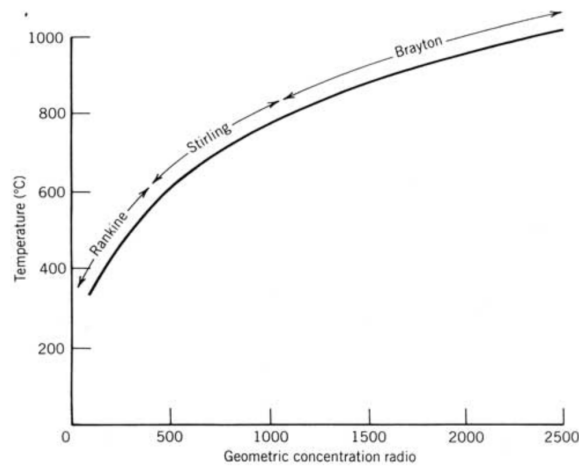
Figure A.3: Optimum operating temperature with geometric concentration ratio. Nominal collector parameters: $I_{b,a}$ = 1000 W/m^2; T_a = 298 K; U_l = 60 $W/m^2 K$; η_{opt} = 0.9; ϵ = 0 (Stine & Geyer, 2001)

inertness and physical stability (Galione et al., 2015). Using molten salt as HTF and TES media can reduce costs by a third compared to a conventional two-tanks system (IEA, 2014). However, the stability of the thermocline in the system makes it a complicated storage method therefore the two-tank system is more desired.

Steam Accumulators
Steam accumulators use sensible heat storage in pressurised saturated liquid. When demand is lower than heat output, the surplus generated steam is fed into a pressurised liquid water volume. This results in condensed steam which increases the temperature and the pressure of the liquid volume. This acts as a storage volume for the steam. The liquid is stored in a horizontal cylinder in which 90% is saturated liquid, and the rest is saturated steam. By storing it as a liquid and not as steam, a higher volumetric capacity and, therefore, higher energy density can be reached. During discharge, the steam is subtracted from the vessel and the pressure of the liquid decreases. Since water can be both storage and working fluid, high discharge rates are possible (Steinmann & Eck, 2006). However, this type of system is not cost competitive yet with other TES systems due to the high investment costs (W. Sun et al., 2016).

A.1.3. Power block
As explained in Section A.1.1, different types of solar fields are used to absorb the Sun's heat. Thermal energy can be stored or directly used to produce power using different power block systems. The power block systems are based on three types of thermodynamic cycles, explained below: the Rankine cycle, Brayton cycle and Stirling cycle. An important aspect that differentiates the cycles from each other is the (optimum) working temperature. As shown in Figure A.3, a Rankine cycle is operable at lower temperatures, making it a very popular choice as the engine. CSP can be used in the Rankine and Brayton cycles in the constant-pressure heat-addition processes. The Stirling, which uses a piston design, can incorporate solar heating for its constant-temperature heat-addition process (Stine & Geyer, 2001).

Rankine cycle
The most common power cycle used in solar power systems is the Rankine cycle. The basics of the Rankine cycle are as follows: a working fluid (water) is pumped from low to high pressure. Afterwards, a heat source converts the high-pressure liquid to a dry saturated vapour (steam) inside a boiler. After that, the dry saturated vapour expands through a turbine to produce electricity. This causes the temperature and pressure of the vapour to decrease, causing condensation. The wet vapour is condensed to to be used again in the boiler. Instead of using water as a working fluid but an organic fluid, such as refrigerants and hydrocarbons, with a lower boiling point as a working fluid, it is called an organic Rankine cycle (ORC). The working fluid depends on the thermodynamic characteristics.

An important factor is the critical point of the working fluid. This is the state at which the conditions (pressure, temperature and sometimes composition) as phase boundary cease to exist. The Rankine (steam) cycle, with a maximum pressure higher than the critical point, is known as super-critical (Astolfi, 2017) and lower is known as sub-critical. A Rankine cycle loses approximately 50% of low-temperature energy to cooling water. To increase efficiency, the Rankine cycle can increase the peak temperature (without increasing the pressure). This process is known as super-heating. According to Messadi and Timoumi (2018), to improve the efficiency of the Rankine cycle depends on the performance of each component used, the nature of the working fluid, the heat transfer fluid, the condensation conditions, the evaporation conditions and the overheating temperature at the inlet of the turbines, and the nature of the cycle used: cycle with overheating, with single or multiple reheating or with regenerations. According to Besarati and Goswami (2017), subcritical steam Rankine cycles are currently used in all operating solar thermal power plants. However, the thermal efficiencies of these power cycles are limited to about 42%.

Brayton cycle
The method used in a gas turbine is based on the Brayton cycle. There are two types of Brayton cycles, an open and closed Brayton cycle. In an open Brayton cycle, the air is taken from the atmosphere to be compressed and afterwards heated in a heat exchanger so that the gas expands, to push the turbine blades producing power. Finally, the residual heat in the exhaust is dumped into the surroundings. Approximately 45% of the power produced by the high-temperature expansion is used in compressing air, along with considerable heat loss in the exhaust (Stein & Buck, 2017). To combat these losses, a closed Brayton engine can be used which cools the residual heat from the exhaust to be used again in the compressor. A closed cycle is used if a working gas other than air is used, for example, helium or hydrogen or carbon dioxide. The heat source needed in the heat exchanger can be produced by CSP, for example, a solar dish. The efficiency of the Brayton cycle is increased by adding several stages, such as regeneration, intercooling and reheating. When the inlet temperatures are between 850-900 °C in a closed-loop Brayton cycle with helium working, a net cycle efficiency up to 48% can be achieved (Besarati & Goswami, 2017).

Stirling cycle
A Stirling engine is based on the principle that when a working gas (air, helium, hydrogen) is enclosed in space when heated, it expands, and when it is cooled, it contracts. This compression or expansion of the working gas results in a pressure change which powers a piston inside the engine cylinder. Electricity can be produced by coupling the motor shaft to an electrical generator. The heat from the Sun can be transferred to the Stirling engine's hot side to provide the engine's thermal input. The cold side is provided by ambient temperature. These Stirling engines operate at relatively high speed, providing a high power density. Operating at temperatures between 700-1000 °C (Breeze, 2018b). When CSP is applied, a Stirling engine could theoretically achieve close to 40% energy conversion efficiency. However, the best so far recorded is 32% (Breeze, 2018b).

A.1.4. Technical challenges
There are several technical challenges that a CSP plant needs to overcome for a successful implementation. The most critical challenges are described below. Firstly, the necessary water consumption of the system is explained in Section A.1.4. Secondly, in Section A.1.4, the necessary dust cleaning of the heliostat mirrors is described. Thirdly, the choice of the heat transfer fluid as transport and ideally as a storage medium is explained in Section A.1.4.

Water consumption
For current CSP systems, 3 and 3.5 m3/kWh of water is required, 95% of which is used for the cooling tower and 5% is consumed for mirror cleaning (X. Xu et al., 2016). There are two methods for the cooling process: wet cooling and dry cooling. Wet cooling can provide a higher conversion efficiency than dry cooling because the exhaust steam from a power block can be cooled faster. However, dry cooling can consume 80-90% less water, dependent on the dry cooling system. There are three dry cooling methods—the direct method, where the exhaust steam from the turbine is transported to an air-cooled condenser. The indirect method uses a condenser heat exchanger through a closed-loop water cooling process to dissipate thermal power. The hybrid is based on an operation of two systems in parallel, dry and wet cooling, dependent on the ambient outside temperature. An alternative is to

use CSP desalination techniques to use the power to remove salt, other minerals, and contaminants from seawater to use as cooling water. The most competitive and cheapest method is the multi-effect desalination (MED) which uses 4-4.5 kWh/m^3. Other methods are using reverse osmosis and multi-stage flash.

Dust cleaning

According to X. Xu et al. (2016), almost all CSP systems are installed in arid or semi-arid regions with high DNI. Therefore, the occurrence of dust accumulation on heliostat mirrors is very high. According to Solar Power World, a dust layer of 1/7 ounce per square yard can cause a decrease of 40% in solar power conversion (Hunter et al., 2014). Cleaning the mirrors with water and detergent is the best solution, but this is time-consuming and labour-intensive, using an average of 0.15-0.175 m^3/kWh of water. However, developments are being made in data-driven solutions, recover water, and anti-dust coating to reduce cost and water consumption.

Heat Transfer Fluid

Heat Transfer Fluid (HTF) is an essential component of a CSP plant as it transports the concentrated heat by the receiver to the steam generator. The HTF also acts as a storage media for a direct two-tank system, which is ideal. Multiple characteristics are desirable as HTF: the energy storage density, thermal, chemical and cyclic stability, heat transfer between HTF and TES material, costs, abundance, flammability, toxicity and more (Alva et al., 2017) (Alnaimat & Rashid, 2019). For high-temperature applications, molten salts are the most widely used HTF. The composition of 60% sodium nitrate ($NaNO_3$) and 40% potassium nitrate (KNO_3) is the most common, known as Solar Salt. This is because of their high volumetric heat capacity, high boiling point, high-temperature stability and vapour pressure being close to zero, neither toxic nor flammable (Caraballo et al., 2021). Molten salt does have the disadvantages of having a high viscosity, high melting point (resulting in solidification of pipes), and low thermal conductivity compared to other materials (Alva et al., 2018) (Gil et al., 2010). As a result, alternatives are being researched; a comprehensive review has analysed fifteen different TES materials, see Table A.3. The results show that nitrate-based materials are similar when compared based on their nature, thermo-physical properties and economic impact. The studied chloride-based materials are favourable for high-temperature applications due to their very attractive low cost (excluding KMgZnCl) (Caraballo et al., 2021).

	Specific Cost $/kg	E^m MJ/kg	E^v MJ/m^3	E $/MJ
	Nitrate-based			
Solar Salt	1.3	0.491	901.1	2.65
Hitec	1.93	0.480	826.9	4.02
Hitec XL	1.66	0.464	928.1	3.58
LiNaKNO3	1.1	0.683	1285.7	1.61
LiNaKCaNO3	0.7	0.542	977.1	1.29
LiNaKNO3NO2	N/A	0.408	764.9	N/A
	Chloride-based			
KMgCl	0.35	0.271	431.3	1.29
NaKMgCl	0.22	0.325	541.6	0.68
NaMgCaCl	0.17	0.289	739.7	0.57
NaKZnCl	0.8	0.447	986.6	1.79
KMgZnCl	1	0.298	553.4	3.36
	Fluoride-based			
LiNaKF	2	0.391	824.1	5.11
NaBF	4.88	0.474	885.4	10.29
KBF	3.68	0.313	833.3	11.75
KZrF	4.85	0.280	750.3	17.32
	Carbonate-based			
LiNaKCO3	2.02	0.448	**9912**	4.15

Table A.3: Specific cost and energy of selected molten salt TES materials (Caraballo et al., 2021)

A.1.5. Comparison CSP systems

A complete overview of the different concentrated solar power types is shown in Table A.4. Based on the explanation and analysis in the previous sections, it is clear that the complete CSP systems differ from each other. Higher total annual efficiencies from solar to electric are reached for SPT and SPD. However, this is reflected in the operations and maintenance costs which are higher than PTC and LFR. Based on the concentration ratio, SPT and SPD have a concentration ratio of more than 1000, which results in a higher operating temperature of the solar field. The operating temperature determines the applicable power block cycle system and fluid conditions. As mentioned in the table, PTC and LFC have the highest installed capacity (MWe) due to the simple storage possibility and lower operating temperature.

Table A.4: Performance parameters of different concentrated solar powered systems (IRENA, 2021; Islam et al., 2018; Liu et al., 2016; Rezk et al., 2022)

Criteria	PTC	LFR	SPT	SPD
Capacity (MWe)	200	200	150	0.4
Annual solar-to-electric efficiency (%)	15	10	35	35
Optical efficiency (%)	Medium	Low	Medium	High
Thermal efficiency (%)	40	36	40	40
Plant peak efficiency (%)	20	18	25	30
Concentration ratio	100	80	1000	3000
Concentration collector (suns)	80	60	1000	1300
Operation & maintenance cost ($/kWh)	0.012-0.02	0.005	0.034	0.21
LCOE ($/kWh) without TES	0.17	0.14	0.19	0.15
LCOE ($/kWh) with TES	0.11 (8-10h)	0.11 (10h+)	0.11 (8-10h)	-
Capital cost ($/kW)	4200	5200	4300	-
Capital cost ($/$m^2$)	424	234	476	-
Typical shape of solar plant	Rectangular	Rectangular	Sector of a circle/ rectangular	Rectangular
Land requirement	Large	Medium	Medium	Small
Water requirement wet (m3/MWh)	3	3	2	0.05
Water cooling (L/MWh)	3 000 or dry	3 000 or dry	2 000 or dry	-
Operation temperature of solar field (\degree C)	290–550	250–390	250–650	800
Storage with molten salt	Commercially available	Possible, but not proven	Commercially available	Possible, but not proven
Power block cycle and fluid conditions	Superheated steam Rankine, steam @380 °C/100 bar	Saturated steam Rankine (steam @ 270 °C/55 bar), superheated steam Rankine (steam @ 380 °C/50 bar)	Superheated steam Rankine, steam @ 540 °C/100 –160 bar	Stirling/ Brayton

Storage possibility, storage system	Yes, but not yet with direct steam generation (DSG) indirect 2-tank molten salt at 380 °C ($\Delta T = 100C$) or Direct 2-tank molten salt at 550 °C ($\Delta T = 300$ °C) 14h TES	Yes, but not yet with DSG, Short-term pressurized steam storage (< 10 min)	Depends on plant configuration Direct 2-tank molten salt at 550 °C (= 300 °C)	Yes, but in limited cases Depends on plant configuration No storage, chemical storage under development
Heat Transfer fluid	Synthetic oil, water/steam (DSG), molten salt Molten salt with lower melting points, air, steam, supercritical CO2 (demonstration), air (demonstration)	Water/steam	Water/steam, molten salt, air (demonstration)	Air, hydrogen, helium
Steam conditions (°C/bar)	380 to 540/100	260/50	540/100 to 160	Not applicable

A.2. Photovoltaic system

Photovoltaics (PV) is the process that converts sunlight into electricity. The working principle of solar cells is based on the photovoltaic effect. The generation of a potential difference at the junction of two different materials in response to electromagnetic radiation, according to Smets et al. (2016). Using PV technology in an integrated system to satisfy demand consists of choosing between three important elements. Firstly the cell material choice of the PV technology, this is explained in Section A.2.1. Secondly, if a certain cell type is chosen, does it have bifacial compatibility, and what extra gain can be achieved? This is described in Section A.2.2. Thirdly, in Section A.2.3 the available solar tracking systems and their most important characteristics are explained.

A.2.1. Cell material

There are many different types of solar cell materials, as shown in Figure A.4. This section describes the two most dominant first-generation crystalline silicon solar cells, mono-crystalline silicon and poly-crystalline silicon, with corresponding advantages and disadvantages and an overview of technical parameters. Followed by a description of the very promising perovskite solar cell, a third-generation solar cell with both a promising technical and cost reduction potential. The current advantages and disadvantages are explained with an overview of the future outlook of the technology.
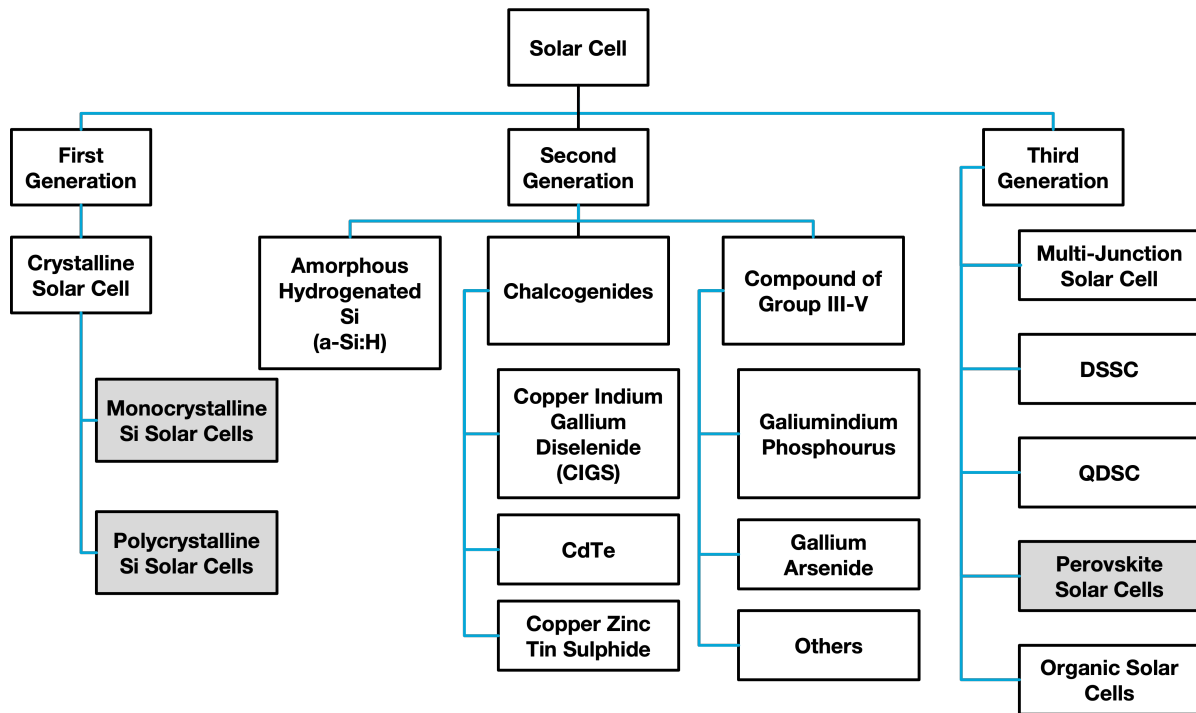
Figure A.4: Various types of solar cells and current advancement (Dambhare et al., 2021)

Crystalline Silicon

Crystalline silicon solar cells have driven the 150 GW PV industry (Wilson et al., 2020). According to Fraunhofer ISE (2021) the Si-wafer-based PV technology accounted for about 95% of the total production in 2020. The share of mono-crystalline technology is about 84% of the total c-Si production. The commercially produced cell material types explained below are highlighted in grey in Figure A.4. Crystalline silicon is the crystal form of silicon. Silicon is widely used in semiconductors because it is an abundant element with an advantageous covalent bond structure. Semiconductors based on silicon distinguish themselves between two types of doping. Doping is the process that intentionally submits impurities into an intrinsic semiconductor. This doping is added to regulate the optical, electrical and structural properties. After being doped, it is called an extrinsic semiconductor. There are two types of doping, n-type silicon, where the electrons have a negative charge, and p-type silicon, the absence of electrons creates a positive charge. Either n-type or p-type can be split again into two different processing techniques: mono-crystalline or poly-crystalline.

Mono-crystalline silicon Mono-crystalline, also known as single-crystalline silicon solar panels, is when the cell's entire volume is a single silicon crystal. A crystalline solid in which the crystal lattice is aligned and unbroken without any grain boundaries over the entire bulk up to the edges and has one uniform colour (Smets et al., 2016). The record lab cell efficiency is 26.7% (Fraunhofer ISE, 2021). On average, mono-Si has an efficiency of 18-22% and ensures the highest power output compared to the other panels, thus requiring the least amount of space. The area required for 1 kWp is between 6-9 m^2 (Taraba et al., 2019). However, they have deficient performance in low-light conditions and are unsuitable for shaded areas or diffused light situations. However, they have proven to show better results if exposed to direct light. In general, mono-Si have high production costs (Sharma et al., 2015). Table A.5 gives an overview of technical parameters.

Poly-crystalline silicon Poly-crystalline, often abbreviated as poly-silicon, is a material that consists of many small crystalline grains with random orientations. Between these grains are grain boundaries. Here mismatches and defects occur, affecting the wafer's efficiency (Smets et al., 2016). Due to their orientation, these crystals can produce energy even with low or diffused light ensuring a more constant out production during the day. The record lab cell efficiency is 24.4% for multi-crystalline silicon wafer-based technology (Fraunhofer ISE, 2021). The average efficiency is between 13-16%

and therefore require wider surfaces of 8-9 [m^2] for 1 KWp (Taraba et al., 2019). Poly-crystalline solar generally has lower prices because the production process is cheaper and simpler (Sharma et al., 2015). Table A.5 provides an overview of these crystalline silicon PV technology characteristics.

Table A.5: Overview of important characteristics of mono- and polycrystalline silicon PV technology (Adeeb et al., 2019; Benda & Černá, 2020; Dash & Gupta, 2015; DOE, 2021; Fraunhofer ISE, 2021; Shahriar et al., 2020)

Type	Mono-Si	Poly-Si
Module Efficiency	18-22%	13-16%
Area required for 1 KWp	6-9	8-9
Cost (average) 2020 ($/$W_p$)	0.185-0.380 (0.200)	0.160-0.290 (0.177)
Temperature coefficient for P_{max} (%/°C)	-0.42	-0.45
Degradation rate (%/year)	0.5	0.5
Installed GWp (2020)	120.6	23.3

Once the doping type is chosen with the desired processing technique, multiple contacting types are used to extract current. Until 2013, it was dominated by the aluminium back surface field (Al-BSF), which plateaued with an efficiency of around 20%. This led to the search for new cell architectures, with the Passivated Emitter and Rear Cell (PERC) as the most commercially developed, with 15% of the market in 2017. PERC can reach a higher efficiency by adding extra layers to the traditional silicon solar cell with minimal extra manufacturing cost. Additionally, the cell design can be adapted to make a bi-facial cell, which is further discussed in Section A.2.2. However, PERC does have problems with degradation processes. Light-induced degradation (LID) can cause modules to lose a percentage of power after the first exposure to light. Furthermore, potential induced degradation (PID) can lead to significant power losses in long-term operation (Taylor & Jäger-Waldau, 2018). PERC is often referred to as a technology family because several variations exist: Passivated Emitter Rear Locally-diffused (PERL), Passivated Emitter Rear Totally diffused (PERT), and Tunel Oxide Passivated Contact (TOPCon). Other cell architectures, Si-Heterojunction, Interdigitated Back Contact (IBC) and Si-based tandem cell configuration, are also gaining interest. Figure A.5 shows the future perspective of different cell architectures.
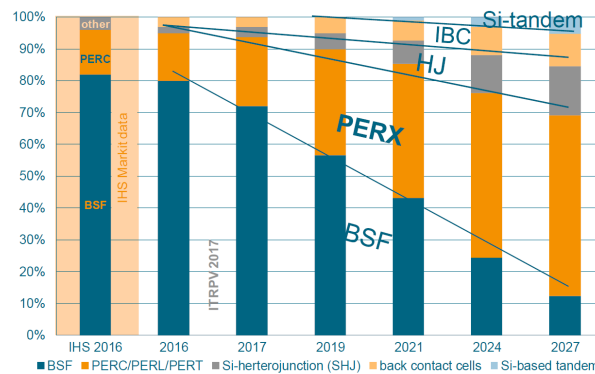
Figure A.5: Market share of different cell architects from 2016-2027 (Metz et al., 2017b)

Perovskite

Perovskite solar cells (PSCs) have gained popularity in the photovoltaic family within a short duration. It has become one of the promising photovoltaic technologies for the future due to its high power conversion efficiency. Perovskite is the original name of calcium titanate ($CaTiO_3$), applied to the class of materials with the same crystal structure type. In 2009, a power conversion efficiency of 9.7% was measured. In 2021 a lab efficiency of 25.7% was achieved by effective coating and composition engineering (NREL, 2022) (DOE, 2022). Advantageous is that PSCs require cheap raw material and a simple processing technique which uses a disposition technique at low temperatures with relatively little energy (TNO, 2022). However, the cell material is still heavily being researched due to challenges in stability and degradation. PSCs have problems such as that they cannot handle moisture, oxygen and

extended periods of light or heat. The current lifetime of a PSC is several months of operation, which needs to become 20 years for commercial applications (DOE, 2022). Table A.6 provides insight into the cost reduction and technical performance increase for perovskites in 2020 and 2030. The estimated values are based on a perovskite single junction system in 2020 and a two-junction with an increased efficiency system in 2030.

Table A.6: Performance parameter of perovskite cell in 2020 and expected in 2030 (Smith et al., 2020)

Perovskite cell	2020	2030
Average cost ($/$W_p$)	0.38	0.18
Efficiency at STC (%)	13.0	28.0
Power temperature coefficient (%/°C)	-0.20	-0.20
Degradation rate per year (%)	10.0	0.50

A.2.2. Monofacial and bifacial solar panels

The oldest photovoltaic technology, monofacial solar panels absorb light only from the front side of the panel, and the back sheet is opaque. In contrast, bifacial solar panels can produce electrical energy by illumination on both front and rear surfaces. In 2020, 10% of the market share consisted of bifacial modules. This will become an estimated 35% in 2030 (Metz et al., 2017a). The energy gain and cost are the most important aspects determining whether implementing a bifacial module is beneficial. The bifacial system is attractive if the additional energy gain outweighs the extra cost. The energy yield gain is determined by the surface albedo (the reflectivity of the ground), the installation height of the panels, spacing, and tilt angle. An absolute white surface has an albedo of 1, and grassland/vegetation has an albedo between 0.1-0.25 based on the soil conditions. An overview of different albedo values relative to the type of underground is shown in Appendix A.4. The higher the albedo, the more sun rays are reflected by the ground surface into the back absorbing layer of the bifacial solar panel. Thus if a bifacial module is installed in an area with a higher Albedo value, a higher bifacial gain can be reached. In Figure A.6 this relationship is shown. An important characteristic to show this relation is the bifaciality factor (%), defined as the ratio between rear efficiency and front efficiency based on the same irradiance.
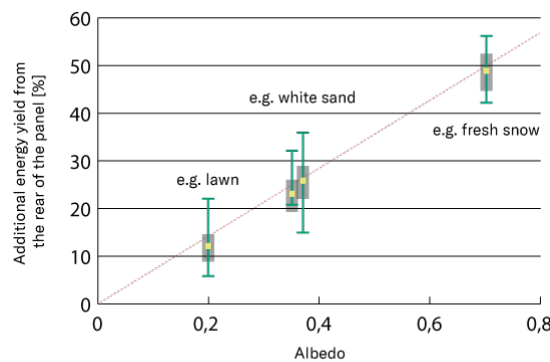
Figure A.6: Influence of albedo on energy yield from the rear of the panel (Rödl & Partner, 2020)

Implementing a bifacial system compared to a monofacial system results in extra costs. The manufacturing cost of the module determines the higher costs, and the module depends on the bifacial module's cell architecture. Table A.7 provides the difference between these types and their corresponding additional cost. A major study was conducted by Rodríguez-Gallegos et al. (2018) in 55 countries to map out how the LCOE of bifacial relate to monofacial in any module orientation (AMO). The results show that in latitudes above 40° bifacial modules are more cost-effective than monofacial modules.

Table A.7: Difference between bifacial and monofacial module based
on their cell architecture (Deline et al., 2019)

Bifacial module type	PERC+	n-PERT	Si Heterojunction
Bifaciality	0.65-0.80	0.75-0.90	0.85-0.95
Extra cost compared to monofacial PERC	+0%	+9%	+16%
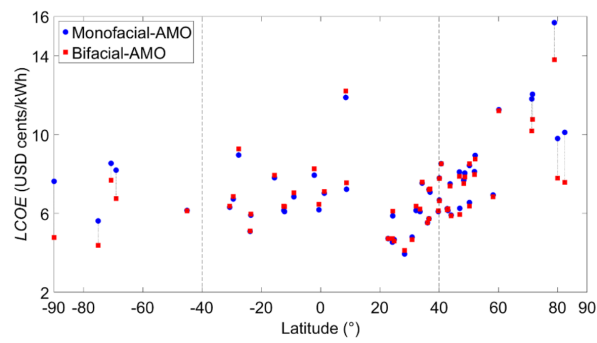
Figure A.7: LCOE comparison Monofacial-AMO vs Bifacial-AMO
based on latitude orientation (Rodríguez-Gallegos et al., 2018)

A.2.3. Solar tracking system

For a solar panel to transform photons from the Sun into electricity, it needs to maximize the absorption of solar energy. It does this by having the rays of the sun strike perpendicular to the surface of solar panels. However, the position of the Sun moves every hour and every month. During the day, it moves from East to West. In the northern hemisphere, the Sun is near the horizon in the winter and overhead in the summer. The incident irradiation on the solar panel is maximized by having the system orientated based on the optimum tilt angle. "To obtain the optimum tilt angle, a rule of thumb for quick optimization is to use an angle equal to the latitude of the location facing south in the northern hemisphere and the north in the southern hemisphere" according to Isabella (2021). The solar panel system has three orientation methods to absorb the maximum amount of sun rays: fixed, single-axis and dual-axis tracking. An overview of these different types of solar orientation is shown in Figure A.8. Based on these different orientation methods, a choice can be made between the classic monofacial solar panel and the bifacial solar panel. The different types of tracking systems are explained below, ending with a technical comparison.
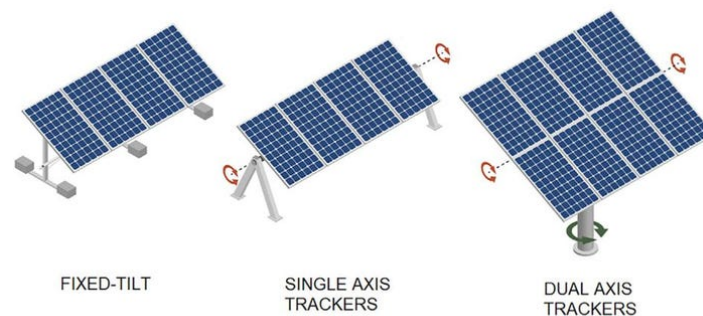
Figure A.8: Fixed, single-axis and dual-axis solar panel orientation (Snowden, 2020)

Fixed Axis

Fixed tilted solar panels have a constant fixed (and tilted) position throughout the year. For solar panels located further away from the equator, it can be better to adjust seasonally or monthly because the difference between winter and summer is larger. The optimal angle orientation is chosen by analyzing the maximum energy yield based on the different tilt angles and azimuth. The simple installation and low material usage make this the cheapest solar panel system.

Single-Axis tracking

Single-axis tracking is a mechanical tracking system that tracks the Sun by rotating around one axis. Single-axis trackers have one angle as the axis of rotation and a tracker to move from the east to the west by following the Sun's direction. This is a relatively low-cost, simple and efficient method to improve the functioning of the solar installation (Weimar, 2020). However, the usefulness of single-axis trackers decreases further towards the north due to the angle variance between winter and summer. A vertical axis tracker is, therefore, better. There are different types of single-axis trackers; these are shortly explained below.

Horizontal (Tilted) Single-Axis solar Tracker (H(T)SAT)

HSAT rotates throughout the day from east to west on a fixed axis parallel to the ground. This system has a simple structure and uses less material for construction than other tracking orientations. Additionally, no special connection is needed to rotate the system about its centre of gravity. HTSAT are similar to the HSAT, but the solar panels are tilted. This tracking system is more complex and often requires a concrete foundation which adds to the extra costs.

Vertical (Tilted) Single-Axis solar Tracker (V(T)SAT)

VSAT is mounted in north/south or east/west orientation to follow more "up-and-down" movement of the Sun in the sky. The axis of rotation is vertical with respect to the ground. This becomes more advanta-

geous in high-altitude/mountainous locations. Unlike solar panels that are horizontally positioned, a vertical field layout needs to accommodate the tall profile of the vertical tracker. It needs a separation between the units to avoid shading and energy-related losses (Weimar, 2020). VTSAT are comparable with the HTSAT, but the tilt aligns to a horizontal position and rotates on a vertical axis. Vertical trackers are subject to increased wind loads compared to horizontal units, and the high structural demand requires extra concrete and steel (Weimar, 2020).

Dual-Axis tracking
Dual-axis tracking is a mechanical tracking system with two axis degrees which enable the rotational axis to move upwards and downwards to adjust to the angles of the Sun throughout the entire day. There are two types of dual-axis trackers: the azimuth-altitude dual-axis tracker (AADAT) and the tip-tilt dual-axis tracker (TTDAT). The difference between the two types is the orientation of the primary axis to the ground. AADATs have the primary axis vertical to the ground, and TTDATs have their horizontal. The azimuth/altitude method seems to be primarily used, based on its references in multiple research articles on tracking (Gupta et al., 2016).

Table A.8: Overview of important characteristics of a fixed, single-axis and dual-axis tracking system (Gupta et al., 2016; Lane, 2022; Maatallah et al., 2011; Metz et al., 2017b)

Type	Fixed-Axis	Single-Axis	Dual-Axis
Average power gain	0%	+10-20%	+30-50%
Average extra cost	0%	+15%	+103%
Estimated payback time (years)	13	15.5	19
KW_p/m^2	Low	Medium	High
Technology	Fixed	Mechanical	Mechanical
Preferred latitude	Equator	Equator/high latitude	High latitude
Installed in 2020	65%	33%	2%

A.3. Battery energy storage system

Batteries can store the power generated by a renewable energy source. Batteries are an energy storage technology that uses chemicals to absorb and release energy on demand. When there is low demand, energy can be stored and released at peak demand. Such a system is called a battery energy storage system (BESS). Commercially implemented BESSs regulate frequency, support voltage levels, support ramping and assist in shifting electric energy time. There are currently over 50 different types of rechargeable batteries available. Two essential criteria need to be satisfied to decide which type of battery can be implemented to be combined with a renewable-powered system. Firstly, the maturity level of the battery technology and secondly, the realistic implementation in a large-scale industrial application with a function to be autonomous. There are three types of batteries that have been scaled commercially: electrochemical batteries, redox flow batteries and hybrid batteries. An overview of the different types of batteries that will be researched in this chapter is shown in Figure A.9. First, the different electrochemical batteries are analyzed in Section A.3.1. After that, the different redox flow battery options are explored in Section A.3.2. Followed by a short analysis of the possible hybrid flow batteries available in Section A.3.3. Finally, Section A.3.4 presents a summary with a classification of the chosen batteries based on the criteria mentioned above.
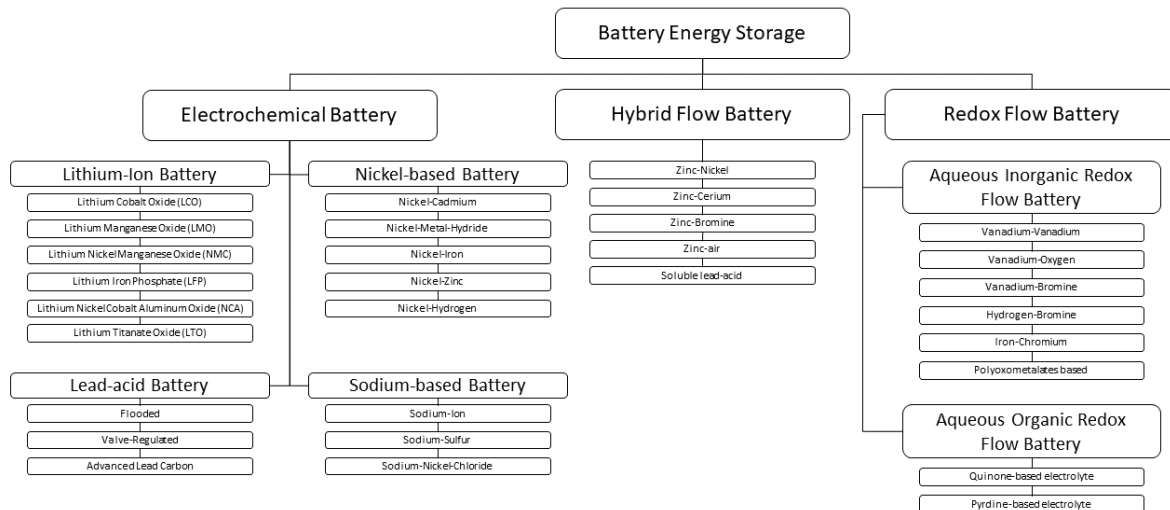
Figure A.9: Overview of the different researched batteries

A.3.1. Electrochemical batteries

The most well-known battery type on the market is electrochemical batteries. The basic working of such a battery is described in Section A.3.1. Section A.3.1 explains the main criteria for these types of batteries. Finally, Section A.3.1 examines the different types of electrochemical batteries based on the criteria.

Battery energy storage system

An electrochemical battery consists of one or several electrochemical cells. Every cell consists of two electrodes and an electrolyte separated by a semi-permeable barrier. The flow of electrons generates electricity through an external wire. A flow of electrons is created by an electrode that produces electrons known as the anode (negative electrode) so that electrons flow to the other electrode known as the cathode (positive electrode). A reduction-oxidation chemical reaction takes place at the anode between the electrode and the electrolyte to produce electrons and at the same happens at the cathode to accept electrons. Electrons have a negative charge. The reaction continues to run and stay balanced because the electrolyte provides a medium to transport positively charged ions. During charging, the opposite happens. The external power source forces the cathode to let electrons and ions flow back to the anode. This charging and discharging, known as cycles, decreases the battery's performance, which is why

rechargeable batteries do not last forever. In Figure A.10, a schematic is shown of an electrochemical battery.
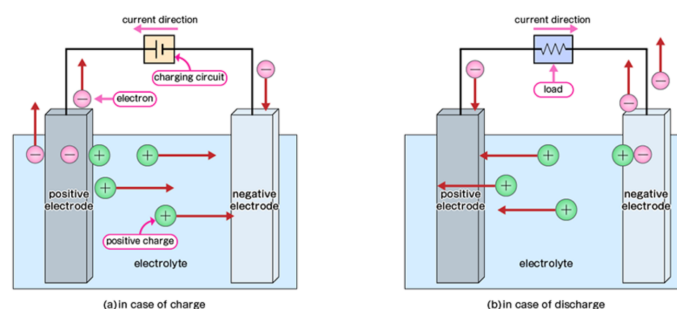
Figure A.10: A schematic of the basic working of an electrochemical battery (Yoon, 2021)

Selection criteria for electrochemical batteries
There are two important criteria when selecting a battery technology. First, the battery system needs to be low-cost because a too expensive system will not be considered. Secondly, does the battery system have the technical parameters to satisfy the necessary demand. Electrochemical batteries are a mature type of technology. The battery system for a storage terminal is stationary; thus, energy density (Wh/kg) is not essential, but the area occupied by the system plays a role. The most relevant characteristics are power/energy capacity, storage duration, cycle life/lifetime, self-discharge, round-trip efficiency and energy cost. Electrochemical batteries are generally designed to store energy for 4 hours, so this will be the minimum storage duration of the system. In Table A.9, the minimal performance parameters for the electrochemical battery system are provided with reasoning.

Table A.9: Key characteristics with corresponding value and reasoning for electrochemical batteries

Performance parameter	Minimum value	Reason
Power capacity (MW)	1	To distinguish between industrial scaled batteries and home-applied batteries
Energy capacity (MWh)	4	Based on the minimum rated power capacity with an 4-hour storage duration
Storage duration (hours)	4	The standard storage duration of a battery is 4 hours
Cycle life	1800-3650	Minimum cycle life of 5-10 years assuming 365 days per year
Self-discharge per day (%)	1-3	To maximize cycle operation of the battery system
Round-trip efficiency (%)	70	To ensure that the cost of the system is minimized

Types of electrochemical batteries
There are many different types of electrochemical batteries. The most important types are described below, with corresponding advantages and disadvantages and an overview of essential performance parameters to determine if the battery type is applicable for a storage terminal. The most critical electrochemical batteries mentioned below are: lithium-based, lead-based, nickel-based and sodium-based.

Lithium-based batteries
Lithium-ion (Li-ion) batteries are rechargeable batteries characterized by their high power density (Gladysz & Chawla, 2015). Li-ion batteries are one the most popular and mature battery types, used in most electronic products such as cell phones and electric vehicles. During discharge, the anode releases lithium ions in an oxidation process which passes to the cathode. The created electrons from the ions flow in the opposite direction of the powered electronic circuit. The ions and the electrons then reform at the cathode. During charging, the opposite happens. The lithium ions from the cathode are passed through the electrolyte to the anode. The electrons provided by the electronic circuit combine with the lithium ions to provide stored electrical energy.

The large-scale applicability of Li-ion batteries in the mobile energy storage sector has resulted in significant investments in lithium-ion battery technology. According to Persson (2020), economies of scale driven by market growth are simultaneously lowering the cost of the technology. Figure A.11 presents the projected capital costs of a complete lithium-ion battery system. In 2020, a system costs 350 $/kWh and is expected to decrease to 198 $/kWh in 2030 and 149 $/kWh in 2050.
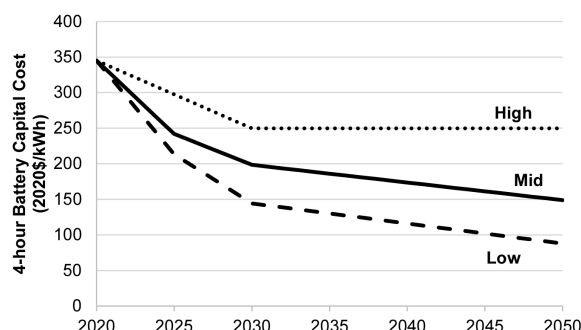
Figure A.11: High, mid and low battery cost projections for 4-hour lithium-ion systems (Cole et al., 2021)

According to Pramanik et al. (2019), the advantages of Li-ion batteries are the high energy density compared to other batteries. Lithium-ion batteries have a low rate of charge loss and a relatively high number of charge and discharge cycles. However, Li-ion batteries are extremely sensitive to high temperatures, involve the risk of bursting, and are costly. There are different types of Li-ion batteries: Lithium Cobalt Oxide (LCO), Lithium Manganese Oxide (LMO), Lithium Nickel Manganese Oxide (NMC), Lithium Iron Phosphate (LFP), Lithium Nickel Cobalt Aluminium Oxide (NCA) and Lithium Titanate Oxide (LTO). An overview of these batteries with corresponding characteristics is shown in Appendix A.5. LCO is the most mature Li-ion battery type due to its large-scale implementation in the cellphone and laptop industry. However, it does not have good lifetime durability, which is essential for grid storage use-cases (Killer et al., 2020). The LTO battery has a very high cycle life which is advantageous but is still under research to be implemented as a stationary storage system (Hesse et al., 2017). NMC, LFP and NCA batteries are Li-ion batteries applied in stationary systems on an industrial scale. Furthermore, a 1 to 3 hours discharge time has only been tested in techno-economical research papers by Burke et al. (2012) and Ud-Din Khan et al. (2022). The Li-ion battery is generalized with corresponding technical parameters in literature reviews and comparison studies. Table A.10 provides an overview of these parameters.

Table A.10: Performance parameter of Li-ion battery (Abdin & Khalilpour, 2018; Cole et al., 2021)

Parameter	Li-ion
Energy density (Wh/kg)	75-200
Power density (W/kg)	150-2000
Rated energy capacity (MWh)	0.004-10
Power rating (MW)	0.1-100
Lifetime (years)	5-15
Cycle life	1,000-20,000
Discharge time (hours)	4
Efficiency (%)	85-95
Energy installation cost in 2020 (2030) ($/kWh)	350 (198)

Lead-based batteries

Lead-acid (PbA) batteries are based on the chemistry that the positive active material is lead dioxide (PbO_2) and lead (Pb) as the negative active material with a fluid-like solution of sulfuric acid (H_2SO_4) as the electrolyte. In 2020, an energy storage system of 1 MW with a 4-hour energy duration cost between 414-489 $/kWh and in 2030, 351-418 $/kWh. For a 10 MW system with a 4-hour energy duration in 2020, it will cost between 380-448 $/kWh, and in 2030, it is expected to decrease to 324-384 $/kWh

(PNNL, 2022). Lead-acid batteries are classified into two types: flooded and valve-regulated.

The flooded lead-acid battery contains an electrolyte that is free to move around in the battery encasement. Therefore, it is crucial to keep these batteries mounted upright so that the electrolyte does not leak out of the caps on top. These batteries release toxic hydrogen gas when charging and thus need to be vented to the outside to prevent a hazardous environment from happening. Furthermore, to ensure a longer lifespan, distilled water needs to be added to compensate for the loss of the electrolyte solution. There are two types of flooded batteries: starter and deep-cycle. The starter is used in cars with a short discharge time. Deep-cycle batteries are designed for cycling with a capacity rated with a 5-hour and 20-hour discharge (Buchmann, 2016).

A valve-regulated lead-acid (VRLA) battery prevents the electrolyte movement inside the battery by trapping the hydrogen near the plates. This reduces the water loss during the discharge/recharge cycle and makes the system maintenance-free (adding water is unnecessary), and the battery is sealed. There are two types of VRLA batteries: absorbent glass mat (AGM) and gel. In AGM technology, the battery is spill-proof because the sulfuric acid is absorbed by a very fine fibreglass mat (Buchmann, 2016). It offers the ability to charge faster and realize deep cycles, but with lower specific energy and higher manufacturing cost than flooded batteries. The sulfuric acid is mixed with a silica-type gel in gel batteries to avoid spillage. These types of batteries are more expensive than AGM but have a higher performance during their lifetime caused by the better heat transfer (Buchmann, 2016).

Both flooded and VRLA batteries require a long charging time (more than 14 hours), the advanced lead-carbon (ALC) lead-acid battery solves this problem by adding carbon to the cathode. According to Buchmann (2016), this changes the battery into a supercapacitor which, however, does cause a voltage drop on discharge. In Appendix A.22, an overview of different lead-based batteries with corresponding performance parameters is shown. From the parameters, it is clear that lead-based technology is insufficient to satisfy a terminal's performance criteria based on cycle life (based on full DoD). Longer cycle life of 2000-7000 can be reached with a lower DoD (10-30%), but this is not economically viable even with the expected decrease in cost by 2030.

Nickel-based batteries
Nickel-based batteries use nickel oxide hydroxide (NiOOH) as the positive electrode. There are different types of nickel-based batteries: nickel-cadmium (Ni-Cd), nickel metal hydride (Ni-MH), nickel-iron (Ni-Fe), nickel-zinc (Ni-Zn), nickel-hydrogen (Ni-H_2). All these batteries have different operating characteristics and are used in variable applications, as shown in Appendix A.7. Ni-Zn and Ni-MH have investment costs that are too high in proportion to the cycle life. Ni-Fe and Ni-H_2 have a cycle life that can satisfy the minimum lifetime of ten years to supply power for the terminal.

Nickel cadmium is based on the following charging principle, during discharge, the nickel oxide-hydroxide combines with water and produces nickel hydroxide and a hydroxide ion. At the negative electrode, Cadmium hydroxide is produced. When the battery is charged, the process can be reversed. Despite the relatively high cycle life, there are some major disadvantages. The battery system contains cadmium, a highly toxic heavy metal that suffers from memory effect and has a relatively high investment cost with minimal reduction in the near future. In Table A.11, key performance parameters are shown.

Ni-Fe is well known for its robustness, non-toxicity and eco-friendliness, with a high cycle life and a specific energy 1.5-2 times that of a lead-acid battery (Abdalla et al., 2016). The battery that is needed for the proposed system needs to be able to overcome the nighttime. Therefore multiple batteries (hundreds) with high capacity are needed to satisfy demand, which results in substantial-high investment costs. A Ni-Fe battery pack of 48V with 1000Ah from Iron Edison, the Ni-Fe battery manufacturer, costs $41,828.00, resulting in roughly 800 $/kWh. Due to the high cycle life claimed by the manufacturer of more than 50 years, this system can be economically viable. Furthermore, nickel-iron batteries are being investigated to be used in combination with electrolysis for hydrogen production as storage, known as a "battolyser". The system is charged and discharged like regular batteries, but when fully charged produces hydrogen (Mulder et al., 2017). According to the company website, it is currently

waiting to complete the next phase of scaling to a 2MWh/2MW system. This battery technology has a high potential if the investment cost can be reduced. Performance parameters of Iron Edison are shown in Table A.11.

Table A.11: Performance parameter of Ni-Cd and Iron Edison Ni-Fe battery
(EASE, 2016; Iron Edison, 2016)

Nickel battery type	Ni-Cd	Ni-Fe
Energy density (Wh/kg)	30-70	20-95
Energy output (MW)	10	10
Power output (MW)	0.1-2	0.05-1
Lifetime (years)	10-20	30
Cycle life	1,000-5,000	11,000
Discharge time (hours)	4	5
Efficiency (%)	60-70	80
Installation cost in 2016 ($/kWh)	400-700	800

$Ni-H_2$ has an extremely high cycle life and low volumetric energy density due to the gaseous hydrogen. However, using platinum as a catalyst makes the system very costly and has shown limited applications, except for satellites and aerospace applications. Due to the long service life, very high reliability, stability and durability (Zimmerman, 2009).

Sodium-based batteries
Three mature sodium-based batteries have the potential to operate as battery storage for a terminal: sodium-ion battery (SIB), sodium-sulfur battery (NaS) and sodium-nickel-chloride battery ($Na-NiCl_2$). These batteries are described below with corresponding advantages and disadvantages, including technical characteristics.

Sodium-ion battery
Sodium-ion batteries (SIBs) have a similar structure and fundamental working to that of a Li-ion battery. The positive electrode is the sodium-ion source that contains the transferable sodium ions, often used are sodium transition metal oxides or Prussian blue analogues. For the negative electrode, disordered carbons (hard carbons) are used. According to K.M. Abraham, research professor at Northeastern University and CTO of lithium battery consulting firm E-KEM Sciences, projects the cost of sodium-ion batteries is about 10-20% less than lithium-ion, and they are very sustainable. Sodium batteries are abundant, cheap, stable, safe and user-friendly materials (Patel, 2021). The world leader in sodium-ion technology, Faradion, has claimed the following performance parameters. As can be seen in Table A.12, it shows a high expected cycle life which can be very promising in future use. Suppose lithium-ion battery assembly lines can be converted to sodium-ion batteries with long cycle life. In that case, this can drastically reduce costs in the future (Tapia-Ruiz et al., 2021).

Table A.12: Performance parameter of Faradion Na-ion batteries in 2021 and future
perspective in 2026 (Tapia-Ruiz et al., 2021)

Parameter	Faradion Na-ion (2021)	5 year target (2026)
Specific energy (Wh/kg)	160 (32 Ah pouch)	210
Specific power (W/kg)	1000 (2 Ah pouch)	2000
Cycle life (80% DOD)	3000	8000
Round-trip energy efficiency (%)	93	95

Sodium-sulfur battery
An alternative sodium-based battery is the sodium-sulfur (NaS) battery, which was originally developed as much larger and made specifically for large MW-scale systems (Ferrari, 2021). In NaS batteries, the positive electrode is molten sulfur, and the negative electrode is molten sodium; therefore, the system must be in a heated state. A ceramic material that only allows positively charged sodium ions to pass through is used to separate the electrodes. Despite these batteries requiring heaters to maintain the

system at greater than 300 °C, the round-trip efficiency of NaS batteries is high, approaching 90%. This is because NaS systems are made from low-cost materials and are even more economically viable due to economies of scale, with lower prices for larger systems (Ferrari, 2021). One of the largest projects is installed in Abu Dhabi, United Arab Emirates, with 108 MW of capacity with a 6-hour duration (648 MWh) (Ferrari, 2021). An overview of the performance parameters of a NaS battery is shown in Table A.13.

Sodium-nickel-chloride battery
An alternative high-temperature sodium-based battery is the sodium-nickel-chloride ($Na - NiCl_2$) battery, also known as the ZEBRA battery. The electrochemical charge/discharge reactions occur between sodium metal as the anode and $NiCl2/FeCl_2$ consisting of the cathode. A ceramic electrolyte (Na ion conductor) separates the anode and cathode. $NaAlCl_4$ transports sodium ions to the positive electrode. Higher diffusivity is achieved between the solid reactants and higher conductivity of the solid electrolyte by having the cell operate at around 300 °C. The battery system is maintenance-free, fully recyclable, high efficiency, high energy density and very safe. However, the ceramic electrolyte easily degrades, reducing battery lifespan and needs to be kept in a molten state (Mexis & Todeschini, 2020). Furthermore, chlorine gas has a bad reputation as a chemical weapon which can cause problems with being accepted in certain countries, according to Ad van Wijk (Professor of Technical University Delft). In Table A.13, an overview of performance parameters is provided for a sodium-nickel-chloride battery.

Table A.13: Performance parameter of NaS and $Na - NiCl_2$ battery (Arabkoohsar, 2021; Breeze, 2018a, 2019; Ferrari, 2021; IRENA, 2017; Mexis & Todeschini, 2020; Mongird et al., 2020)

Parameter	NaS	Na-NiCl2
Energy density (Wh/kg)	110	100-120
Power density (W/kg)	150	150-160
Energy output (MWh)	0.4-32	0.12-5
Rated power output (MW)	0.05-4	0.001-1
Lifetime (years)	10	15
Cycle life	4,500	4,500
Storage duration (hours)	<10	<10
Efficiency (%)	70-90	85-95
Energy installation cost in 2016 (2030) ($/kWh)	499 (225)	403 (165)

A.3.2. Redox flow batteries

According to Lim et al. (2015), the redox flow battery (RFB) has received great attention in recent years due to its attractive structure for large-scale energy storage applications. The basic working of a redox flow battery is described in Section A.3.2. Section A.3.2 explains the main criteria for these RFBs. Moreover, based on the criteria, an explanation of advantages and disadvantages per RFB is provided in Section A.3.2.

Basic working of a redox flow battery
Unlike rechargeable batteries, where the conversion and storage takes place in closed cells, RFBs have the conversion and storage of energy separated. RFBs have a structure similar to a fuel cell and thus have the feature that energy and power can be scaled separately. Energy is defined by the amount of energy storage medium and power by the cell size and the number of cells. The specific investment cost decreases with an increase in the energy to power ratio. Furthermore, the chemical reaction occurs between the electrolytes instead of between an electrolyte and an electrode. Therefore no electro-deposition or loss in electroactive substances occurs during cycling (C. Blanc & Rufer, 2010). A VRB consists of two tanks that store the discharged/charged electrolytes, a converting energy system (a cell stack) comprising several cells connected in series or parallel, pumps for pumping the electrolytes through the power converting system and a connection to the energy generating/consuming system. In Figure A.12, a schematic of a redox flow battery is shown. During the operation of a RFB, two reactions occur simultaneously on both sides of the ion-permeable membrane between the anolyte and catholyte. In every RFB, different reactions take place determined by the redox couples of the active solutions or materials. During discharge, an oxidation reaction takes place in the anolyte releasing electrons. The

electrons move through the external circuit to produce power and are accepted at the catholyte. During charging, the electron flow in the opposite direction resulting in an oxidation reaction in the catholyte and reduction in the anolyte.

The advantages of RFBs are the ability to size the power and energy of the system independently, thus allowing for virtually unlimited capacity (Alotto et al., 2014). Other advantages are the design of the membrane that ensures good electrode permeability and high electrode active area (Weber et al., 2011). Additionally, because the Redox flow reaction is reversible, it enables a long cycle life. Furthermore, RFBs have a controllable cell temperature, no self-discharge, low maintenance, and deep charges are viable and capable of rapid response and energy management services (Alotto et al., 2014). However, RFBs also have disadvantages, such as low power and energy density, making them unsuitable for mobile applications. The cell-active areas and membranes are large, increasing the dimensions of the battery, causing a high transverse gradient of the solutions, and reducing the average current density and nominal current density compared to the theoretical values. Another disadvantage is that the electrolytes are conductive, which can cause shunt currents, producing additional losses and affecting electric efficiency. A specifically designed system is needed to control the heat/temperature of the electrolyte (Alotto et al., 2014).
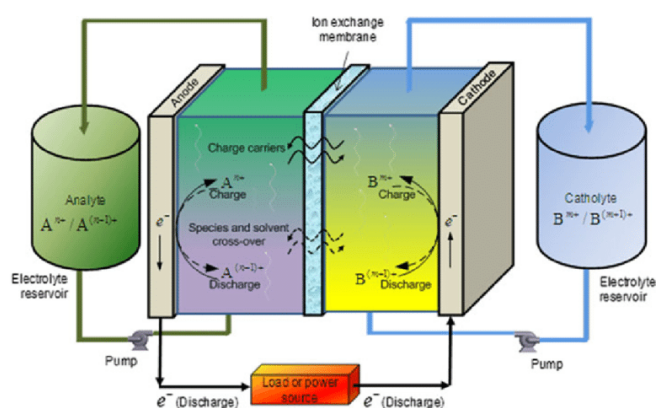
Figure A.12: A schematic of the basic working of a redox flow battery (Weber et al., 2011)

Selection criteria for redox flow batteries

The basic principle of working a redox flow battery is old, but the commercial research and development of redox flow batteries are relatively new. Therefore, a technology readiness level study of the different redox flow batteries is essential. The Technology readiness level (TRL) is a measurement system used to assess the maturity level of a particular technology. The scale is from 1 (the basic principles are documented) to 9 (the technology is released, and industrial production is started). The TRL can provide insight into how developed the technology (the battery) is but more insight into batteries which might be interesting in the near future if they can overcome their challenges. In Table A.14, the redox flow batteries researched in this report are shown with their corresponding TRL. The redox flow batteries with values of six and higher are further researched in Section A.3.2. The minimum performance parameters for the large-scale commercial implementation for the terminal are the same as previously described in Table A.9.

Table A.14: Overview of researched redox flow batteries with corresponding TRL

Redox flow battery types	TRL (1-9)
Aqueous inorganic flow batteries	
Vanadium-vanadium	9
Vanadium-oxygen	3-4
Vanadium-bromine	4-5
Hydrogen-bromine	7-8
Iron-chromium	8
Polyoxometalates based	4-5
Aqueous organic flow batteries	
Quinone-based electrolyte	4-5
Pyrdine-based electrolyte	6-7

Types of redox flow batteries

Redox flow batteries can be split into two categories: organic and inorganic. Inorganic can be categorized as acqueous, only using a fluid (liquid or gas) as a medium for the redox reaction to occur and hybrid, which uses one or more solid layers as an electroactive component. Organic batteries can be categorized as acqueous (use water as electrolyte solvent) and non-acqueous (use organic solvents as electrolytes). If these types are combined with an inorganic anode or cathode, they are called a hybrid. The most advanced types were further researched from the long list of researched and developed redox flow batteries. The further researched batteries are selected in Table A.14. Acqueous flow batteries are the most popular, split between inorganic and organic redox flow batteries. The inorganic acqueous RFBs with a value higher than 6 are vanadium-vanadium (9), iron-chromium (9), and hydrogen-bromine (7-8). Multiple early-stage organic acqueous flow batteries are based on different compositions, such as viologens, phenazines, altoxanes, ferrocenes, thiaxzines and more. According to Brushett et al. (2020), several start-up companies are emerging based on organic components: Kemiwatt, Green Energy Storage, XL Batteries, JenaBatteries and CMBlu. JenaBatteries with an anolyte that is pyridine based with a TRL of 6-7. The hybrid batteries are further explained and researched in Section A.3.3.

Vanadium-vanadium flow battery

A vanadium-vanadium redox flow battery is the most advanced flow battery system. It is based on the redox couples V^{2+}/V^{3+} and V^{4+}/V^{5+} in the anolyte and catholyte (Revankar, 2019). Advantages are the low maintenance cost, high energy efficiency, the ability to deep charge without affecting the cycle life and tolerance to overcharging. However, the system is not applicable for small-scale energy storage applications due to the need for pumps, sensors, power management, and secondary containment (Revankar, 2019). Furthermore, the downside is that vanadium is a scarce and expensive metal, and the electrolyte used in the system is fairly toxic. In Table A.15, vanadium-vanadium flow battery performance characteristics are shown.

Iron-chromium flow battery

An iron-chromium flow battery is based on the redox couples Fe^{3+}/Fe^{2+} and Cr^{3+}/Cr^{2+} in hydrochloric acid solution medium used in the anolyte and catholyte (Revankar, 2019). Using low-cost, low toxic and abundant chromium and iron chlorides as redox materials makes it very advantageous (Zeng et al., 2016). However, it suffers from system complexity because of SOC re-balancing, according to Zeng et al. (2016). Furthermore, due to the use of chromium, the risk of parasitic side reactions can cause capacity loss and unfavourable electrolyte imbalance. However, developers have been able to counteract this effect (C. Sun et al., 2021). Since the end of 2020, a demonstration project of 250kW/1.5MWh in Zhanshigou, China, has been stable for nearly 400 days with a storage time of 6 hours (Airvers, 2022). Demonstrating the commercial potential of iron-chromium flow batteries to be implemented in the near future. Literature-based parameters from Zeng et al. (2015) are shown in Table A.15.

Hydrogen-bromine flow battery

Hydrogen-bromine flow battery uses HBr as an electrolyte in the system. During charging, HBr is split into H^+ and Br^- ions, producing Br_2 and H_2. During a discharge cycle, H_2 is recombined with Br_2 to form HBr releasing the stored energy. The electrolyte has rapid reaction kinetics, low cost, and uses an abundance of active material (Lin et al., 2016). The chemicals crossover of bromine and

hydrogen bromine to the hydrogen side can deactivate the catalyst. This can decrease the performance and lifetime (Hugo et al., 2016). There are specific safety concerns. Firstly, the escape of broom vapour can cause health damage if inhaled. Secondly, explosions can occur due to gas build-up of hydrogen gas. Thirdly, the release of hydrogen bromide can be fatal. An overview of the technical characteristics of a hydrogen bromide battery by the leading manufacturer Elestor is shown in Table A.15.

Prydine-based anloyte (JenaBatteries)
JenaBatteries is a redox flow start-up that developed a flow battery without metal that uses the analyte based on the organic pyridine compound. The company claims that it is ideal for areas of application with high technical safety requirements due to the low maintenance and safe materials. In Table A.15, performance parameters of the battery are provided.

Table A.15: Overview of selected redox flow batteries (Abdin & Khalilpour, 2018; Elestor, 2022; IRENA, 2017; JenaBatteries, 2020; Zeng et al., 2015)

Redox flow type	Vanadium-vanadium	Iron-chromium	Hydrogen-bromine (Elestor)	JenaBatteries
Energy Density (Wh/kg)	40-130	-	-	11
Power density W/kg)	50-140	-	-	3
Efficiency (%)	75-85	75	65-75	70
Rated Power (MW)	100	1	50	2
Storage duration (hours)	10	8	10	-
Cycle life	12,000-14,000	10,000	10,000	10,000
Lifetime (years)	10-20	-	10-20	10-20
Energy installation cost in 2016 (2030) ($/kWh)	315 (108)	-	-	-

A.3.3. Hybrid batteries

Hybrid flow batteries can be better described as the 'non-true' form of redox flow batteries or a combination of traditional secondary and redox flow batteries. The electrolytes are still stored in external tanks, but they are pumped through the core during charging and discharging. This is similar to conventional batteries, where one electrolyte is electroplated on the electrodes in the cell core (Niclas, 2015). Due to the structure of the battery, where power and energy are not separated, limits the system's scalability because a large energy storage capacity requires a larger battery cell core. Although using cheaper elements than a standard vanadium-vanadium flow battery, zinc-based technologies can cause a build-up of zinc residues (expensive) membrane, gradually leading to corrosion and thus reducing efficiency over time (Niclas, 2015). As shown in Table A.16, Zinc-bromine is currently the only hybrid flow battery that satisfies the minimum TRL and large-scale implementation criteria mentioned above.

Table A.16: Overview of researched hybrid flow batteries with corresponding TRL

Hybrid flow battery	TRL (1-9)
Zinc-nickel	5-6
Zinc-cerium	4-5
Zinc-bromine	9
Zinc-air	3-4
Soluble lead-acid	5-6

Zinc-bromine flow battery

A zinc-bromine (ZnBr) flow battery consists of two electrolytes flowing past carbon-plastic composite electrodes in two compartments, separated by a micro-porous polyolefin membrane. The anolyte is purely water-based, while the catholyte contains an organic amine compound to hold bromine in solution (Revankar, 2019). During discharge, Zn and Br combine into zinc bromide, increasing Zn^{2+} and Br^- ion density in both electrolyte tanks releasing energy. During charge, metallic zinc is plated as a thin film on one side of the carbon-plastic composite electrode. While on the other side of the membrane, bromine evolves as a dilute solution to react with other agents (organic amines) to produce thick bromine oil that sinks to the bottom of the electrolytic tank (Revankar, 2019). ZnBr has a relatively high energy density, works under normal temperatures, has deep discharge capability and good reversibility. According to Kim et al. (2017), downsides include dendrite formation, material corrosion and relatively low cycle efficiencies compared to traditional batteries, which can limit its applications. In Table A.17, an overview is provided with the performance parameters of a ZnBr battery.

Table A.17: Performance parameter overview of selected batteries (IRENA, 2017; Wu et al., 2019) (Abdin & Khalilpour, 2018)

Performance parameter	Zinc-bromine
Energy Density (Wh/kg)	60-80
Power density W/kg)	50-150
Cycle efficiency (%)	65-75
Rated Power (MW)	10
Storage duration (hours)	<10
Cycle life	10,000
Lifetime (years)	10 to 20
Energy installation cost in 2016 (2030) ($/kWh)	1680 (576)

A.3.4. Summary and battery choice

Based on the researched batteries in the previous sections, the batteries can be classified into three categories. The first category, "Meets criteria" refers to batteries that satisfy the economic, the TRL and large-scale technical implementation criteria. The second category, "High potential", are batteries with very high potential to be utilized as a battery storage system in the near future. The third category, "No potential", are batteries that do not satisfy both criteria and do not show potential soon. A summary of the researched batteries classified in the first two categories is shown in Table A.18.

Table A.18: Classification of researched batteries

Classification	Battery type
Meets criteria	Vanadium-vanadium
	Zinc-bromine
	Lithium-ion
	Nickel-cadmium
	Nickel-iron
	Sodium-sulfur
	Sodium-nickel-chloride
High potential	Hydrogen-bromine
	Faradion Na-ion
	Iron-chromium
	Prydine-based anolyte
	Faradion Na-ion

From the batteries that meet the criteria, four batteries are selected as battery system. The four batteries are the Vanadium-vanadium, Zinc-bromine, sodium-sulfide and Li-ion batteries. The most important criteria were: the future cost perspective, environmental aspects like toxicity and the technical combination of cycle life, lifetime and discharge hours. For a better comparison of these batteries, Table A.19 provides an overview of their performance parameters.

Table A.19: Performance parameter overview of batteries that meet criteria

Battery type	Vanadium-vanadium	Zinc-bromine	Sodium-sulfide	Li-ion
Energy density (Wh/kg)	40-130	60-80	110	75-200
Power density (W/kg)	50-140	50-150	150	150-2000
Efficiency (%)	75-85	65-75	70-90	85-95
Rated Power (MW)	100	10	0.05-4	0.1-100
Storage duration (hours)	8	8	8	8
Cycle life	12,000-14,000	10,000	4,500	1,000-20,000
Lifetime (years)	10-20	10-20	10	5-15
Energy installation cost in 2016 (2030) ($/kWh)	315 (108)	1680 (576)	499 (225)	700 (396)

A.4. Albedo

Natural surface types	Approximated albedo
Blackbody	0
Forest	$0.05 - 0.2$
Grassland and cropland	$0.1 - 0.25$
Dark-colored soil surfaces	$0.1 - 0.2$
Dry sandy soil	$0.25 - 0.45$
Dry clay soil	$0.15 - 0.35$
Sand	$0.2 - 0.4$
Mean albedo of the earth	0.36
Granite	$0.3 - 0.35$
Glacial ice	$0.3 - 0.4$
Light-colored soil surfaces	$0.4 - 0.5$
Dry salt cover	0.5
Fresh, deep snow	0.9
Water	$0.1 - 1$
Absolute white surface	1

Table A.20: Different natural surface types with corresponding approximated albedo (E. Dobos, 2005)

A.5. Performance parameters of lithium-based batteries

Chemistry	Lithium Cobalt Oxide (LCO)	Lithium Manganese Oxide (LMO)	Lithium Nickel Manganese Oxide (NMC)	Lithium Iron Phosphate (LFP)	Lithium Nickel Cobalt Aluminum Oxide (NCA)	Lithium Titanate Oxide (LTO)
Nominal voltage	3.60V	3.70V (3.80V)	3.60V (3.70V)	3.20, 3.30V	3.60V	2.40V
Full charge	4.20V	4.20V	4.20V (or higher)	3.65V	4.20V	2.85V
Full discharge	3.00V	3.00V	3.00V	2.50V	3.00V	1.80V
Minimal voltage	2.50V	2.50V	2.50V	2.00V	2.50V	1.50V (est.)
Specific Energy	150–200Wh/kg	100–150Wh/kg	150–220Wh/kg	90–120Wh/kg	200–260Wh/kg	70–80Wh/kg
Charge rate	0.7–1C (3h)	0.7–1C (3h)	0.7–1C (3h)	1C (3h)	1C	1C (5C max)
Discharge rate	1C (1h)	1C, 10C possible	1–2C	1C (25C pule)	1C	10C possible
Cycle life (ideal)	300-800	800–2000	1000–2000	200–2000	800–5000	3,000–7,000
Energy installation cost in 2016 (expected in 2030)	- (75)	380$/kWh (150)	380$/kWh (150)	580$/kWh (230)	350$/kWh (130)	1,050$/kWh (480)
Thermal runaway	150°C (higher when empty)	250°C (higher when empty)	210°C (higher when empty)	270°C (safe at full charge)	150°C (higher when empty)	One of safest Li-ion batteries
Applications	Mobile phones, tablets, laptops, cameras	Power tools, medical devices, power trains	E-bikes, medical devices, EVs, industrial	Stationary with high currents and endurance	Medical, industrial, EV (Tesla)	UPS, EV, solar street lighting

Table A.21: Overview of performance parameters of different lithium-ion batteries (ADB, 2018) (IRENA, 2017) (Buchmann, 2016), data updated on website (10/2021)

A.6. Performance parameters of lead-based batteries

Chemistry	Starter (SLI) Flooded	Deep-cycle Flooded	AGM VRLA	Gel VRLA	Advanced Lead Carbon (ALC)
Nominal voltage	2.00V				
Full charge	2.45V at ambient, lower when hot		2.40V, or more	2.40V, or less	2.45V
Full discharge	1.75V, must be recharged to prevent sulfation				1.75V
Specific Energy	30–50Wh/kg				20–30Wh/kg; some are higher
Charge rate	0.1–0.05C (16h charge time to get for full saturation)				2–4 times faster
Discharge rate	High momentary current	Continuous moderate current	Moderate to high current		High current
Cycle life (full DoD)	12–15	150–200, longer if not discharged lower than 60% SoC		5–10 years for UPS	Better than regular lead acid
Maintenance	Flooded needs water; 16 hour charge every 6 months to prevent sulfation		Maintenance-free; less prone to sulfation, no water can be added		Less prone to sulfation
Environment	Lead is toxic, electrolyte is caustic	AGM, gel has less lead, electrolyte; avoid heat, use special charger			Toxic
Applications	SLI (starter, light, ignition) for vehicles	UPS, wheeled mobility	Military, aircraft, start-stop, racing, NASCAR, marine	UPS, wheeled mobility, busses, trucks, industry	Vehicles, military, energy storage
Comments	Well-suited for SLI. Low price; large temperature range	Ideal for UPS that needs few cycling	Big seller, cost-effective, fast charging, high power but does not transfer heat as well as gel. Performs well when cold.	High ambient rating, high cycle count, less prone to sulfation, needs correct charge; costly. Tolerant at warm temperatures; low self-discharge.	Better charge acceptance for regenerative breaking; longer lasting

Table A.22: Overview of performance parameters of different lead-based batteries (Buchmann, 2016), data updated on website (10/2021)

A.7. Performance parameters of nickel-based batteries

Chemistry	Nickel-cadmium	Nickel-metal-hydride	Nickel-iron	Nickel-zinc	Nickel-hydrogen
Nominal voltage	1.20V/cell (1.25)		1.20V	1.65V	1.25V
Charge	Taper charger. Constant current; floating voltage		Taper charger, similar to NiCd	Taper charger, similar to NiCd	Not defined
Full charge	Observing voltage drop; plateau voltage as override			1.9V	Not defined
Trickle charge	0.1C	0.05C	Not defined	No trickle charge	Not defined
Specific Energy	45–80Wh/kg	60–120Wh/kg	50Wh/kg	100Wh/kg	40–75Wh/kg
Charge rate	Can be above 1C	0.5–1C	Not defined	Regular charge	Not defined
Discharge rate	Can be above 1C	1C	Moderate	Relative high power	Not defined
Cycle life (full DoD)	2000-2500	500-1000	10,000	200–300	Very long cycle life (>70,000 partial)
Maintenance	Full discharge every 3 months (memory)	Full discharge every 6 months	Not defined	Not defined	Maintenance free; low self-discharge
Failure modes	Memory reduces capacity, reversible	Memory (less affected than NiCd)	Overcharge causes dry-out	Short cycle life due to dendrite growth	Minimal corrosion
Environment	Broad temperature range.Toxic	Considered non-toxic	Poor performance when cold	Good temperature range	−28°C to 54°C
Applications	Main battery in aircraft (flooded), wide temperature range	Hybrid cars, consumer, UPS	German V-1 flying bombs, V-2 rockets; railroad signalling, UPS, mining	Renewed interest to commercial market with improvements	Exclusively satellites; too expensive for terrestrial use
Comments	Robust, forgiving, high maintenance. Only battery that can be ultrafast charged with little stress	More delicate than NiCd; has higher capacity; less maintenance	In 1990, Cd was substituted with Fe to save money. High self-discharge and high fabrication costs	High power, good temperature range, low cost but high self-discharge and short service life	Uses a steel canister to store hydrogen at 8,270kPa (1,200psi)

Table A.23: Overview of performance parameters of different nickel based batteries (Buchmann, 2016), data updated on website (10/2021)

B

System assumptions and input data

B.1. PV model parameters

Table B.1: PV model parameters

PV model parameters	Value			Unit
Surface azimuth	180			°
Maximum rotation angle	90			°
Axis tilt	0			°
K_{shade}	-0.02			-
$K_{transmission}$	0.00			-
IAM	1.0			-
n	1000			-
PV Panel height	2.25			m
Bifaciality	0.70			-
γ, temperature coefficient	0.36			%
	Fujairah	**Laurenshaven**	**Panama**	
Optimal Surface tilt angle	26	36	13	°
Pitch	8.86	10.29	6.60	m
GCR	0.45	0.39	0.61	-
Albedo	0.3	0.2	0.25	-

B.2. Empirically determined coefficients a, b

Table B.2: Empirically determined coefficients used to predict module back surface temperature (King et al., 2004)

Module Type	Mount	a	b	ΔT (°C)
Glass/cell/glass	Open rack	-3.47	-.0594	3
Glass/cell/glass	Close roof mount	-2.98	-.0471	1
Glass/cell/polymer sheet	Open rack	-3.56	-.0750	3
Glass/cell/polymer sheet	Insulated back	-2.81	-.0455	0
Polymer/thin-film/steel	Open rack	-3.58	-.113	3
22X Linear Concentrator	Tracker	-3.23	-.130	13

B.3. DC system losses for a PV system

Table B.3: DC system losses for a PV system per location (Marion et al., 2005) (A. P. Dobos, 2014) (Hasan Shah et al., 2020)

Loss mechanism	Typical derate factor	Range derate factor	Fujairah Losses (%)	Laurenshaven Losses (%)	Panama Losses (%)
Soiling/dust	0.96	0.75 - 0.98	9	2	4
Shading	1.00	0.0 - 1.00	0.5	3	3
Snow	0.00	0.0 - 1.00	0	1	0
Mismatch	0.98	0.97 - 0.985	2	2	2
Wiring	0.98	0.97 - 0.99	2	2	2
Connections	0.995	0.99 - 0.997	0.5	0.5	0.5
Light-induced degradation	0.98	0.90 - 0.99	1.5	1.5	1.5
Nameplate rating	1.00	0.85 - 1.05	1	1	1
Age	0.00	0.0 - 1.00	0	0	0
Total Losses			16	13	14

B.4. Economic parameters

Table B.4: Economic parameters used for the costs of the system

Parameters	Value	Unit	Source
PV system degradation	0.5	%/year	(Jordan et al., 2016)
System lifetime	25	years	Vopak
Debt payment terms PV	25	years	Vopak
Debt payment terms Battery	25	years	Vopak
Depreciation period	15	years	Vopak
Percentage financed by equity	60	%	Vopak
Percentage financed by debt	40	%	Vopak
w, Average annual income U.S.	70,430	%	(World Data, 2021)

	Fujairah	Laurenshaven	Panama		
w, Average annual income	39,410	56,370	14,010	$	(World Data, 2021)
i, Long term annual interest rate	1.5	1.7	1.61	%	(Trading Economics, 2022a)
r, discount rate (WACC)	8.5	5.7	8.0	%	Vopak
Country's corporate tax rate	0	25.8	25	%	(Trading Economics, 2022a)
Average Industry electricity price (incl. tax and transmission fees)	0.04	0.07	0.18	$/kWh	(Boersma, 2020) (Trading Economics, 2022b) (Statista, 2020)

B.5. Cost breakdown of the CAPEX and OPEX of a PV system

Table B.5: Installation cost components of a PV system with corresponding cost price range (NREL et al., 2020)

Cost component	Cost Range ($/kW)	Description
Module price	390 - 430	Costs of an average mono-crystalline monofacial module
Inverter price	50 - 100	Low end: Three-phase string inverter High end: DC power optimiser three-phase string inverter
Structural BOS	80 - 120	Fixed-tilt ground-mounting racking system
Electrical BOS	70 - 120	A variety of parts like conductors, transition boxes, switchgear, panel boards etc.
Install, labour, equipment	80 - 130	Costs associated with the installation of the system
Engineering, procurement, construction (EPC) overhead	60 - 80	Costs associated with EPC, inventory, shipping and handling
Permitting, Inspection, Interconnection (PII)	30 - 50	Construction permits fees, interconnection study fees for existing substations
Developer overhead	50 - 150	Overhead costs such as legal fees, business development, finance, administrative, payroll etc.
Contingency	30 - 50	Markup on EPC costs
Total	**870 - 1210**	
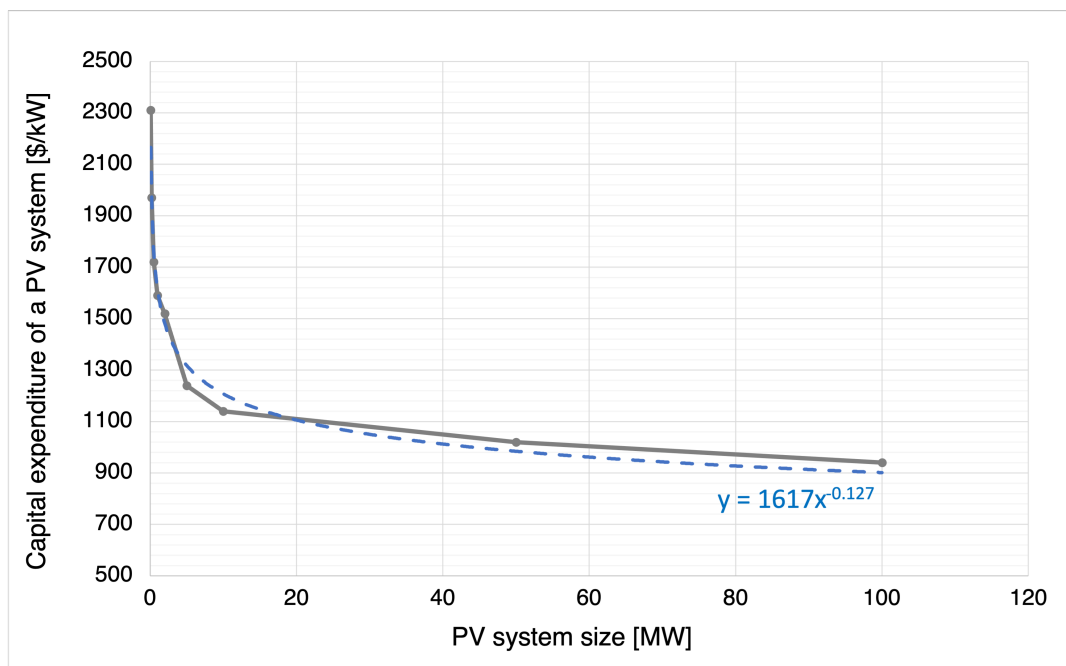
Figure B.1: A visualisation of CAPEX [$/kW] development for an increasing PV size [MW], values from NREL et al. (2020)

Table B.6: O&M costs for a PV system (Andino García et al., 2021) (Sandia Laboratories, 2015) (Feldman et al., 2020)

O&M Item	Budget Range ($/kW − year)	Tasks Including	Variable based on	Fujairah	Laurenshaven	Panama
General site maintenance	0.20 - 1.50	Site upkeep, safety signage, fencing, road/building management, water/waste management, environmental compliance, and other activities	System size, location, frequency of activity	0.8	0.8	0.8
Panel washing	0.80 - 1.30	Ensuring that dust and sand does not impact PV panel production	Site's setting, environment, technology, cleaning, frequency of activity	1.3	0.8	0.8
Vegetation management	0.50 - 1.80	Ensuring that vegetation growth does not impact PV panel power production	Site characteristics and acreage	0.5	1.8	1.8
System inspection and monitoring	1.00 - 3.00	Visual, thermal scanning and current-voltage curve analysis activities	The inspection covers 10% or 100% of the plant	2.0	2.0	2.0
Component parts replacement	0.40 - 0.60	Parts including fuses, contacts, wiring, inverter parts (circuit boards, filters, fans, etc.), disconnect switches, modules and more	Weather conditions and warranty of certain components	0.5	0.5	0.5
Module replacement	1.00 - 3.00	Module replacement due to harsh weather conditions, malfunctions and damage	Module sizes, models and warranty	2.0	2.0	2.0
Inverter replacement	2.00 - 4.00	Typically one inverter replacement activity after the initial warranty period (10-12 years)	Inverter sizes, models and warranty	3.0	3.0	3.0
Tracker maintenance	1.00 - 1.50	Repair/replace PV parts of tracking system	Site size, conditions	1.3	1.3	1.3
Insurance, asset management and security	2.50 - 3.50	To ensure that the PV plant can effectively and safely operate	Insurance cost in place and necessary security	3.0	3.0	3.0
Operations administration	0.40 - 0.60	Administrations behind the operations of the PV plant	The complexity of a country's regulations, administration fees	0.5	0.5	0.5
Property tax	1.50 - 2.00	Obligated tax paid for property	Country's tax regulations	1.5	1.5	1.5
Total	**11.50 - 26.50**			**16.4**	**16.6**	**17.2**

B.6. Cost breakdown of the CAPEX of a battery system

Table B.7: Initial capital expenditure of a Li-ion and Vanadium Redox Flow battery for 4 and 8 hour charge/discharge time (DOE, 2020)

Cost Component	Unit	Li-ion Battery		Vanadium Redox Flow Battery	
		4 Hour	8 Hour	4 Hour	8 Hour
Storage Block	$/kWh	164 - 200	162 - 198	260 - 317	217 - 265
Storage Balance of System	$/kWh	38 - 47	36 - 45	52 - 63	43 - 53
Power Equipment	$/kW	76 - 93	76 - 93	139 - 170	139 - 170
Control Communication	$/kW	36 - 44	36 - 44	36 - 44	36 - 44
System Integration	$/kWh	37 - 56	35 - 52	50 - 61	41 - 50
Engineering, Procurement and Construction	$/kWh	48 - 74	44 - 68	57 - 69	47 - 57
Project Development	$/kWh	57 - 90	52 - 83	72 - 88	60 - 73
Grid Integration	$/kW	29 - 34	28 - 34	28 - 34	28 - 34
Total BESS cost	$/kW	1517- 2040	2775 - 3735	2163 - 2644	3461 - 4230
	$/kWh	379 - 510	358 - 482	541 - 661	433 - 529
Annual cost reduction factor (κ)	%	3.4	3.5	2.2	2.2
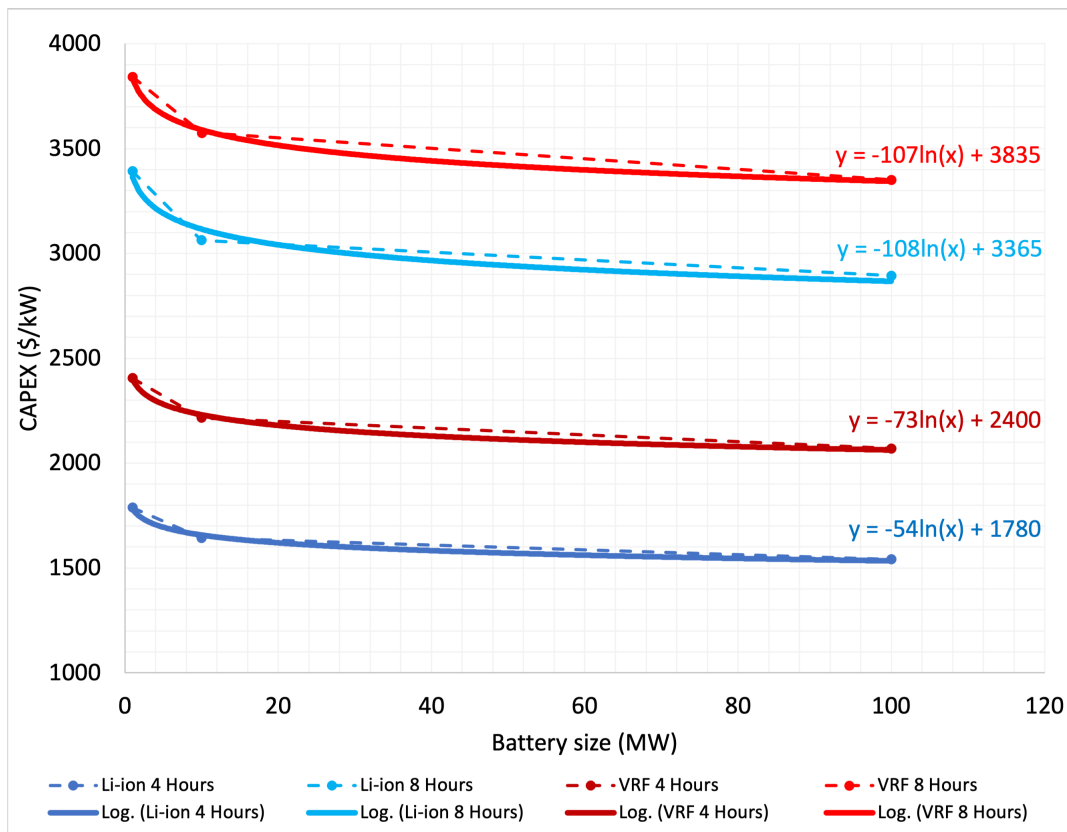
Figure B.2: A visualisation of the CAPEX development for Li-ion/VRF battery for 4/8 hours with increasing battery size (MW), values from DOE (2020)

B.7. PV panel data sheets from Canadian Solar

KuMax

HIGH EFFICIENCY MONO PERC MODULE
CS3U-380|385|390|395|400MS
(1000 V / 1500 V)

MORE POWER

Low power loss in cell connection

Low NMOT: 42 ± 3 °C
Low temperature coefficient (Pmax): -0.36 % / °C

Better shading tolerance

High PTC rating of up to: 93.24 %

MORE RELIABLE

Lower hot spot temperature

Minimizes micro-cracks

Heavy snow load up to 5400 Pa,
wind load up to 3600 Pa*

MBB **5BB**

25 years linear power output warranty*

12 years enhanced product warranty on materials and workmanship*

*According to the applicable Canadian Solar Limited Warranty Statement.

MANAGEMENT SYSTEM CERTIFICATES

ISO 9001:2015 / Quality management system
ISO 14001:2015 / Standards for environmental management system
OHSAS 18001:2007 / International standards for occupational health & safety

PRODUCT CERTIFICATES*

IEC 61215 / IEC 61730: VDE / CE / CQC / MCS / KS / INMETRO
UL 1703 / IEC 61215 performance: CEC listed (US)
UL 1703: CSA / IEC 61701 ED2: VDE / IEC 62716: VDE / IEC 60068-2-68: SGS
Take-e-way

* As there are different certification requirements in different markets, please
contact your local Canadian Solar sales representative for the specific certificates
applicable to the products in the region in which the products are to be used.

CANADIAN SOLAR INC. is committed to providing high quality solar
products, solar system solutions and services to customers around
the world. No. 1 module supplier for quality and performance/price
ratio in IHS Module Customer Insight Survey. As a leading PV project
developer and manufacturer of solar modules with over 36 GW
deployed around the world since 2001.

* For detailed information, please refer to the Installation Manual.

CANADIAN SOLAR INC.
545 Speedvale Avenue West, Guelph, Ontario N1K 1E6, Canada, www.canadiansolar.com, support@canadiansolar.com

Figure B.3: Data sheet: Canadian Solar mono c-Si monofacial

ENGINEERING DRAWING (mm)

Rear View

Frame Cross Section A-A

Mounting Hole

CS3U-400MS / I-V CURVES

■	1000 W/m²	
■	800 W/m²	
■	600 W/m²	
■	400 W/m²	
■	200 W/m²	

5°C	■
25°C	■
45°C	■
65°C	■
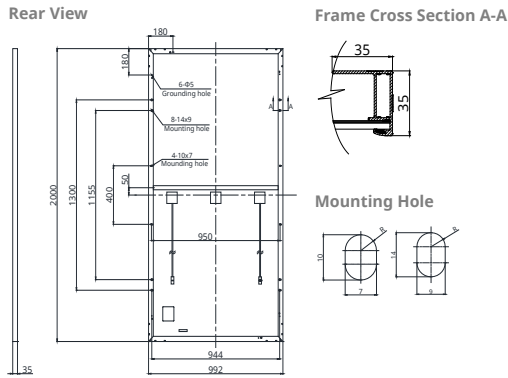
ELECTRICAL DATA | STC*

CS3U	380MS	385MS	390MS	395MS	400MS
Nominal Max. Power (Pmax)	380 W	385 W	390 W	395 W	400 W
Opt. Operating Voltage (Vmp)	40.0 V	40.2 V	40.4 V	40.6 V	40.8 V
Opt. Operating Current (Imp)	9.50 A	9.58 V	9.66 A	9.73 A	9.81 A
Open Circuit Voltage (Voc)	47.8 V	48.0 V	48.2 V	48.4 V	48.6 V
Short Circuit Current (Isc)	10.01 A	10.09 A	10.17 A	10.25 A	10.33 A
Module Efficiency	19.15%	19.41%	19.66%	19.91%	20.16%
Operating Temperature	-40°C ~ +85°C				
Max. System Voltage	1500V (IEC/UL) or 1000V (IEC/UL)				
Module Fire Performance	TYPE 1 (UL 1703) or Class C (IEC 61730)				
Max. Series Fuse Rating	30 A				
Application Classification	Class A				
Power Tolerance	0 ~ + 5 W				

* Under Standard Test Conditions (STC) of irradiance of 1000 W/m², spectrum AM 1.5 and cell temperature of 25°C.

ELECTRICAL DATA | NMOT*

CS3U	380MS	385MS	390MS	395MS	400MS
Nominal Max. Power (Pmax)	283 W	287 W	290 W	294 W	298 W
Opt. Operating Voltage (Vmp)	37.2 V	37.4 V	37.6 V	37.8 V	38.0 V
Opt. Operating Current (Imp)	7.60 A	7.66 A	7.72 A	7.78 A	7.84 A
Open Circuit Voltage (Voc)	44.8 V	45.0 V	45.2 V	45.4 V	45.6 V
Short Circuit Current (Isc)	8.08 A	8.14 A	8.20 A	8.27 A	8.33 A

* Under Nominal Module Operating Temperature (NMOT), irradiance of 800 W/m², spectrum AM 1.5, ambient temperature 20°C, wind speed 1 m/s.

MECHANICAL DATA

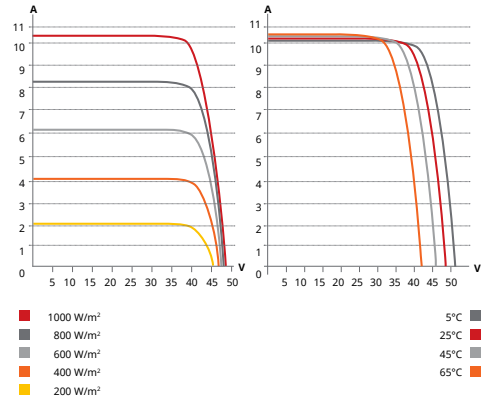| Specification	Data
Cell Type	Mono-crystalline
Cell Arrangement	144 [2 X (12 X 6)]
Dimensions	2000 X 992 X 35 mm (78.7 X 39.1 X 1.38 in)
Weight	22.5 kg (49.6 lbs)
Front Cover	3.2 mm tempered glass
Frame	Anodized aluminium alloy, crossbar enhanced
J-Box	IP68, 3 bypass diodes
Cable	4 mm² (IEC), 12 AWG (UL)
Cable Length (Including Connector)	Portrait: 400 mm (15.7 in) (+) / 280 mm (11.0 in) (-); landscape: 1250 mm (49.2 in);leap-frog connection: 1670 mm (65.7 in)*
Connector	T4 series or H4 UTX or MC4-EVO2
Per Pallet	30 pieces
Per Container (40' HQ)	660 pieces

* For detailed information, please contact your local Canadian Solar sales and technical representatives.

TEMPERATURE CHARACTERISTICS

Specification	Data
Temperature Coefficient (Pmax)	-0.36 % / °C
Temperature Coefficient (Voc)	-0.29 % / °C
Temperature Coefficient (Isc)	0.05 % / °C
Nominal Module Operating Temperature	42 ± 3°C

PARTNER SECTION

* The specifications and key features contained in this datasheet may deviate slightly from our actual products due to the on-going innovation and product enhancement. Canadian Solar Inc. reserves the right to make necessary adjustments to the information described herein at any time without further notice. Please be kindly advised that PV modules should be handled and installed by qualified people who have professional skills and please carefully read the safety and installation instructions before using our PV modules.

CANADIAN SOLAR INC.
545 Speedvale Avenue West, Guelph, Ontario N1K 1E6, Canada, www.canadiansolar.com, support@canadiansolar.com

Oct. 2019. All rights reserved, PV Module Product Datasheet V5.6_EN

Figure B.4: Data sheet: Canadian Solar mono c-Si monofacial

HiKu

SUPER HIGH POWER POLY PERC MODULE

395 W ~ 420 W

CS3W-395|400|405|410|415|420P

MORE POWER

24 % higher power than conventional modules

Up to 4.5 % lower LCOE
Up to 2.7 % lower system cost

Low NMOT: 42 ± 3 °C
Low temperature coefficient (Pmax): -0.36 % / °C

Better shading tolerance

MORE RELIABLE

Lower internal current, lower hot spot temperature

Minimizes micro-crack impacts

Heavy snow load up to 5400 Pa, wind load up to 3600 Pa*

25 years linear power output warranty*

12 years enhanced product warranty on materials and workmanship*

*According to the applicable Canadian Solar Limited Warranty Statement.

MANAGEMENT SYSTEM CERTIFICATES*

ISO 9001:2015 / Quality management system
ISO 14001:2015 / Standards for environmental management system
OHSAS 18001:2007 / International standards for occupational health & safety

PRODUCT CERTIFICATES*

IEC 61215 / IEC 61730: VDE / CE / MCS / KS / INMETRO
UL 1703 / IEC 61215 performance: CEC listed (US)
UL 1703: CSA / IEC 61701 ED2: VDE / IEC 62716: VDE / IEC 60068-2-68: SGS
UNI 9177 Reaction to Fire: Class 1 / Take-e-way

* As there are different certification requirements in different markets, please contact your local Canadian Solar sales representative for the specific certificates applicable to the products in the region in which the products are to be used.

CANADIAN SOLAR INC. is committed to providing high quality solar products, solar system solutions and services to customers around the world. No. 1 module supplier for quality and performance/price ratio in IHS Module Customer Insight Survey. As a leading PV project developer and manufacturer of solar modules with over 40 GW deployed around the world since 2001.

* For detail information, please refer to Installation Manual.

CANADIAN SOLAR INC.
545 Speedvale Avenue West, Guelph, Ontario N1K 1E6, Canada, www.canadiansolar.com, support@canadiansolar.com

Figure B.5: Data sheet: Canadian Solar poly c-Si monofacial

ENGINEERING DRAWING (mm)

Rear View

Frame Cross Section A-A

6-ø5
Grounding
Hole

8-14x9
Mounting
Hole

4-10x7
Mounting
Hole(tracker)

Mounting Hole

CS3W-400P / I-V CURVES

1000 W/m²	5°C
800 W/m²	25°C
600 W/m²	45°C
400 W/m²	65°C
200 W/m²	
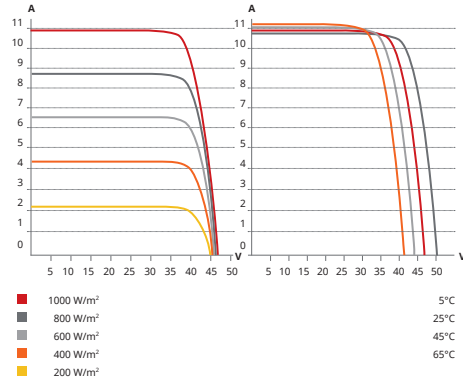
ELECTRICAL DATA | STC*

CS3W	395P	400P	405P	410P	415P	420P
Nominal Max. Power (Pmax)	395 W	400 W	405 W	410 W	415 W	420 W
Opt. Operating Voltage (Vmp)	38.5 V	38.7 V	38.9 V	39.1 V	39.3 V	39.5 V
Opt. Operating Current (Imp)	10.26 A	10.34 A	10.42 A	10.49 A	10.56 A	10.64 A
Open Circuit Voltage (Voc)	47.0 V	47.2 V	47.4 V	47.6 V	47.8 V	48.0 V
Short Circuit Current (Isc)	10.82 A	10.90 A	10.98 A	11.06 A	11.14 A	11.26 A
Module Efficiency	17.9%	18.1%	18.3%	18.6%	18.8%	19.0%
Operating Temperature	-40°C ~ +85°C					
Max. System Voltage	1500V (IEC/UL) or 1000V (IEC/UL)					
Module Fire Performance	TYPE 1 (UL 1703) or CLASS C (IEC 61730)					
Max. Series Fuse Rating	20 A					
Application Classification	Class A					
Power Tolerance	0 ~ + 10 W					

* Under Standard Test Conditions (STC) of irradiance of 1000 W/m², spectrum AM 1.5 and cell temperature of 25°C.

ELECTRICAL DATA | NMOT*

CS3W	395P	400P	405P	410P	415P	420P
Nominal Max. Power (Pmax)	294 W	298 W	302 W	305 W	309 W	313 W
Opt. Operating Voltage (Vmp)	35.8 V	36.0 V	36.2 V	36.4 V	36.6 V	36.8 V
Opt. Operating Current (Imp)	8.21 A	8.27 A	8.33 A	8.39 A	8.45 A	8.51 A
Open Circuit Voltage (Voc)	44.1 V	44.3 V	44.5 V	44.7 V	44.9 V	45.1 V
Short Circuit Current (Isc)	8.73 A	8.79 A	8.86 A	8.92 A	8.99 A	9.08 A

* Under Nominal Module Operating Temperature (NMOT), irradiance of 800 W/m², spectrum AM 1.5, ambient temperature 20°C, wind speed 1 m/s.

MECHANICAL DATA

Specification	Data
Cell Type	Poly-crystalline
Cell Arrangement	144 [2 X (12 X 6)]
Dimensions	2108 X 1048 X 40 mm (83.0 X 41.3 X 1.57 in)
Weight	24.9 kg (54.9 lbs)
Front Cover	3.2 mm tempered glass
Frame	Anodized aluminium alloy, crossbar enhanced
J-Box	IP68, 3 bypass diodes
Cable	4 mm² (IEC), 12 AWG (UL)
Cable Length (Including Connector)	Portrait: 500 mm (19.7 in) (+) / 350 mm (13.8 in) (-); landscape: 1400 mm (55.1 in); leap-frog connection: 1670 mm (65.7 in)*
Connector	T4 series or H4 UTX or MC4-EVO2
Per Pallet	27 pieces
Per Container (40' HQ)	594 pieces

* For detailed information, please contact your local Canadian Solar sales and technical representatives.

TEMPERATURE CHARACTERISTICS

Specification	Data
Temperature Coefficient (Pmax)	-0.36 % / °C
Temperature Coefficient (Voc)	-0.28 % / °C
Temperature Coefficient (Isc)	0.05 % / °C
Nominal Module Operating Temperature	42 ± 3°C

PARTNER SECTION

* The specifications and key features contained in this datasheet may deviate slightly from our actual products due to the on-going innovation and product enhancement. Canadian Solar Inc. reserves the right to make necessary adjustment to the information described herein at any time without further notice.

Please be kindly advised that PV modules should be handled and installed by qualified people who have professional skills and please carefully read the safety and installation instructions before using our PV modules.
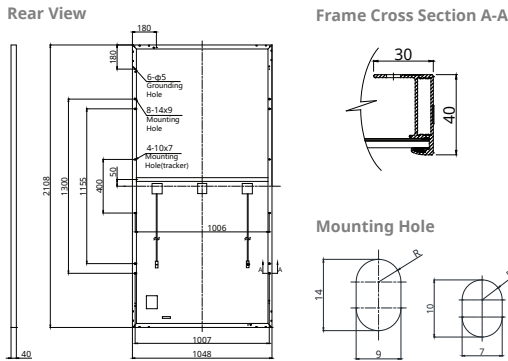
CANADIAN SOLAR INC.
545 Speedvale Avenue West, Guelph, Ontario N1K 1E6, Canada, www.canadiansolar.com, support@canadiansolar.com

May 2020. All rights reserved, PV Module Product Datasheet V5.591_EN

Figure B.6: Data sheet: Canadian Solar poly c-Si monofacial

BiKu MODULE

NEW GENERATION BIFACIAL MODULE
FRONT POWER RANGE: 375W ~ 400W
UP TO 30% MORE POWER FROM THE BACK SIDE
CS3U-375|380|385|390|395|400MB-AG

MORE POWER

EXTRA POWER — Up to 30% more power from the back side

41°C — Low NMOT: 41 ± 3 °C
Low temperature coefficient (Pmax): -0.36 % / °C

Better shading tolerance

MORE RELIABLE

Lower internal current, lower hot spot temperature

Minimizes micro-cracks and snail trails

Heavy snow load up to 5400 Pa, wind load up to 2400 Pa *

Fire Class A and Type 3 / Type 13

FRONT   BACK

5BB cell   MBB cell

* Both 5BB and MBB modules will be supplied.

30 years — **linear power output warranty***

12 years — **enhanced product warranty on materials and workmanship***

*According to the applicable Canadian Solar Limited Warranty Statement.

MANAGEMENT SYSTEM CERTIFICATES*
ISO 9001:2015 / Quality management system
ISO 14001:2015 / Standards for environmental management system
OHSAS 18001:2007 / International standards for occupational health & safety

PRODUCT CERTIFICATES*
IEC 61215 / IEC 61730: VDE / CE / MCS / INMETRO
UL 1703 / IEC 61215 performance: CEC listed (US) / FSEC (US Florida)
UL 1703: CSA / IEC 61701 ED2: VDE / IEC 62716: VDE / IEC 60068-2-68: SGS
Take-e-way

* As there are different certification requirements in different markets, please contact your local Canadian Solar sales representative for the specific certificates applicable to the products in the region in which the products are to be used.

CANADIAN SOLAR INC. is committed to providing high quality solar products, solar system solutions and services to customers around the world. No. 1 module supplier for quality and performance/price ratio in IHS Module Customer Insight Survey. As a leading PV project developer and manufacturer of solar modules with over 36 GW deployed around the world since 2001.
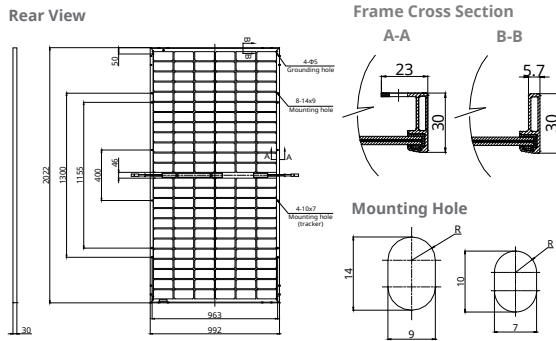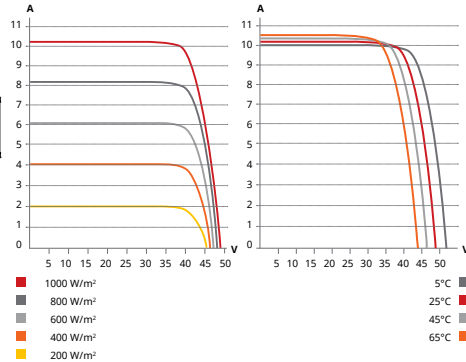
* For detailed information, please refer to Installation Manual.

CANADIAN SOLAR INC.
545 Speedvale Avenue West, Guelph, Ontario N1K 1E6, Canada, www.canadiansolar.com, support@canadiansolar.com

Figure B.7: Data sheet: Canadian Solar mono c-Si bifacial

ENGINEERING DRAWING (mm)

Rear View

Frame Cross Section
A-A   B-B

Mounting Hole

CS3U-390MB-AG / I-V CURVES

■ 1000 W/m²	■ 5°C
■ 800 W/m²	■ 25°C
■ 600 W/m²	■ 45°C
■ 400 W/m²	■ 65°C
■ 200 W/m²	

ELECTRICAL DATA | STC*

		Nominal Max. Power (Pmax)	Opt. Operating Voltage (Vmp)	Opt. Operating Current (Imp)	Open Circuit Voltage (Voc)	Short Circuit Current (Isc)	Module Efficiency
CS3U-375MB-AG		375 W	39.8 V	9.43 A	47.6 V	9.93 A	18.70%
	5%	394 W	39.8 V	9.90 A	47.6 V	10.43 A	19.64%
Bifacial	10%	413 W	39.8 V	10.37 A	47.6 V	10.92 A	20.59%
Gain**	20%	450 W	39.8 V	11.32 A	47.6 V	11.92 A	22.43%
	30%	488 W	39.8 V	12.26 A	47.6 V	12.91 A	24.33%
CS3U-380MB-AG		380 W	40.0 V	9.50 A	47.8 V	10.01 A	18.94%
	5%	399 W	40.0 V	9.98 A	47.8 V	10.51 A	19.89%
Bifacial	10%	418 W	40.0 V	10.45 A	47.8 V	11.01 A	20.84%
Gain**	20%	456 W	40.0 V	11.40 A	47.8 V	12.01 A	22.73%
	30%	494 W	40.0 V	12.35 A	47.8 V	13.01 A	24.63%
CS3U-385MB-AG		385 W	40.2 V	9.58 A	48.0 V	10.09 A	19.19%
	5%	404 W	40.2 V	10.06 A	48.0 V	10.59 A	20.14%
Bifacial	10%	424 W	40.2 V	10.54 A	48.0 V	11.1 A	21.14%
Gain**	20%	462 W	40.2 V	11.50 A	48.0 V	12.11 A	23.03%
	30%	501 W	40.2 V	12.45 A	48.0 V	13.12 A	24.98%
CS3U-390MB-AG		390 W	40.4 V	9.66 A	48.2 V	10.17 A	19.44%
	5%	410 W	40.4 V	10.14 A	48.2 V	10.68 A	20.44%
Bifacial	10%	429 W	40.4 V	10.63 A	48.2 V	11.19 A	21.39%
Gain**	20%	468 W	40.4 V	11.59 A	48.2 V	12.2 A	23.33%
	30%	507 W	40.4 V	12.56 A	48.2 V	13.22 A	25.28%
CS3U-395MB-AG		395 W	40.6 V	9.73 A	48.4 V	10.25 A	19.69%
	5%	415 W	40.6 V	10.22 A	48.4 V	10.76 A	20.69%
Bifacial	10%	435 W	40.6 V	10.70 A	48.4 V	11.28 A	21.69%
Gain**	20%	474 W	40.6 V	11.68 A	48.4 V	12.3 A	23.63%
	30%	514 W	40.6 V	12.65 A	48.4 V	13.33 A	25.63%
CS3U-400MB-AG		400 W	40.8 V	9.81 A	48.6 V	10.33 A	19.94%
	5%	420 W	40.8 V	10.30 A	48.6 V	10.85 A	20.94%
Bifacial	10%	440 W	40.8 V	10.79 A	48.6 V	11.36 A	21.94%
Gain**	20%	480 W	40.8 V	11.77 A	48.6 V	12.40 A	23.93%
	30%	520 W	40.8 V	12.75 A	48.6 V	13.43 A	25.92%

* Under Standard Test Conditions (STC) of irradiance of 1000 W/m², spectrum AM 1.5 and cell temperature of 25°C.
** Bifacial Gain: The additional gain from the back side compared to the power of the front side at the standard test condition. It depends on mounting (structure, height, tilt angle etc.) and albedo of the ground.

ELECTRICAL DATA | NMOT*

	Nominal Max. Power (Pmax)	Opt. Operating Voltage (Vmp)	Opt. Operating Current (Imp)	Open Circuit Voltage (Voc)	Short Circuit Current (Isc)
CS3U-375MB-AG	280 W	37.2 V	7.54 A	44.8 V	8.01 A
CS3U-380MB-AG	284 W	37.4 V	7.60 A	45.0 V	8.07 A
CS3U-385MB-AG	288 W	37.6 V	7.66 A	45.1 V	8.14 A
CS3U-390MB-AG	292 W	37.7 V	7.72 A	45.3 V	8.2 A
CS3U-395MB-AG	295 W	37.9 V	7.78 A	45.5 V	8.26 A
CS3U-400MB-AG	299 W	38.1 V	7.84 A	45.7 V	8.33 A

* Under Nominal Module Operating Temperature (NMOT), irradiance of 800 W/m², spectrum AM 1.5, ambient temperature 20°C, wind speed 1 m/s.

MECHANICAL DATA

Specification	Data
Cell Type	Mono-crystalline
Cell Arrangement	144 [2X (12 X6)]
Dimensions	2022 × 992 × 30 mm (79.6 × 39.1 × 1.18 in)
Weight	25.7 kg (56.7 lbs)
Front / Back Glass	2.0 mm heat strengthened glass
Frame	Anodized aluminium alloy
J-Box	IP68, 3 diodes
Cable	4.0 mm² (IEC), 12 AWG (UL)
Cable Length (Including Connector)	Portrait: 400 mm (15.7 in) (+) / 280 mm (11.0 in) (-); landscape: 1400 mm (55.1 in); leap-frog connection: 1670 mm (65.7 in)*
Connector	T4 series or H4 UTX or MC4-EVO2
Per Pallet	35 pieces
Per Container (40' HQ)	770 pieces or 595 pieces (only for US and Canada)

* For detailed information, please contact your local Canadian Solar sales and technical representatives.

ELECTRICAL DATA

Operating Temperature	-40°C ~ +85°C
Max. System Voltage	1500 V (IEC/UL) or 1000 V (IEC/UL)
Module Fire Performance	TYPE 3 / Type 13 (UL 1703) or CLASS A (IEC61730)
Max. Series Fuse Rating	25 A
Application Classification	Class A
Power Tolerance	0 ~ + 5 W
Power Bifaciality*	70 %

* Power Bifaciality = Pmax$_{rear}$ / Pmax$_{front}$, both Pmax$_{rear}$ and Pmax$_{front}$ are tested under STC, Bifaciality Tolerance: ± 5 %

* The specifications and key features contained in this datasheet may deviate slightly from our actual products due to the on-going innovation and product enhancement. Canadian Solar Inc. reserves the right to make necessary adjustment to the information described herein at any time without further notice.
Please be kindly advised that PV modules should be handled and installed by qualified people who have professional skills and please carefully read the safety and installation instructions before using our PV modules.

TEMPERATURE CHARACTERISTICS

Specification	Data
Temperature Coefficient (Pmax)	-0.36 % / °C
Temperature Coefficient (Voc)	-0.29 % / °C
Temperature Coefficient (Isc)	0.05 % / °C
Nominal Module Operating Temperature	41 ± 3°C

PARTNER SECTION

Figure B.8: Data sheet: Canadian Solar mono c-Si bifacial

BiHiKu

SUPER HIGH POWER BIFACIAL POLY PERC MODULE

390 W ~ 415 W

UP TO 30% MORE POWER FROM THE BACK SIDE

CS3W-390|395|400|405|410|415PB-AG

FRONT   BACK

MORE POWER

EXTRA POWER — Up to 30% more power from the back side

— 24 % higher front side power than conventional modules

41°C — Low NMOT: 41 ± 3 °C
Low temperature coefficient (Pmax): -0.36 % / °C

— Better shading tolerance

MORE RELIABLE

— Lower internal current, lower hot spot temperature

— Minimizes micro-crack impacts

— Heavy snow load up to 5400 Pa, wind load up to 3600 Pa *

30 years — **linear power output warranty***

12 years — **enhanced product warranty on materials and workmanship***

*According to the applicable Canadian Solar Limited Warranty Statement.

MANAGEMENT SYSTEM CERTIFICATES*

ISO 9001:2015 / Quality management system
ISO 14001:2015 / Standards for environmental management system
OHSAS 18001:2007 / International standards for occupational health & safety

PRODUCT CERTIFICATES*

IEC 61215 / IEC 61730: VDE / CE / MCS / INMETRO
UL 1703 / IEC 61215 performance: CEC listed (US) / FSEC (US Florida)
UL 1703: CSA / IEC 61701 ED2: VDE / IEC 62716: VDE / IEC 60068-2-68: SGS
Take-e-way

* As there are different certification requirements in different markets, please contact your local Canadian Solar sales representative for the specific certificates applicable to the products in the region in which the products are to be used.

CANADIAN SOLAR INC. is committed to providing high quality solar products, solar system solutions and services to customers around the world. No. 1 module supplier for quality and performance/price ratio in IHS Module Customer Insight Survey. As a leading PV project developer and manufacturer of solar modules with over 40 GW deployed around the world since 2001.
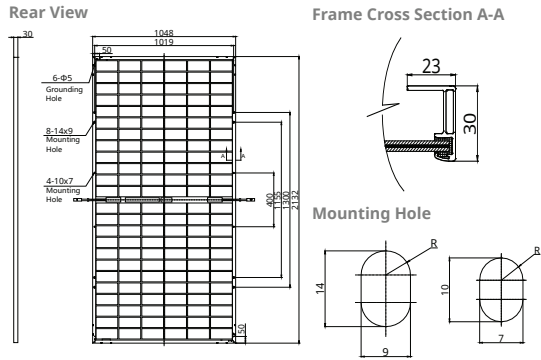
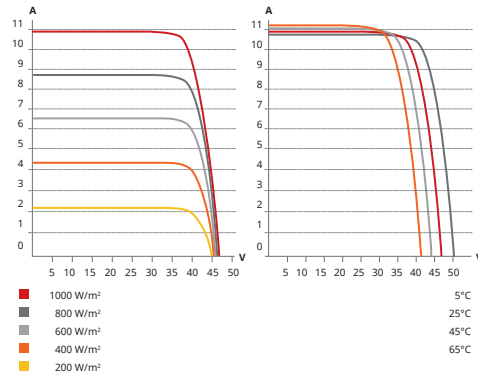* For detail information, please refer to Installation Manual.

CANADIAN SOLAR INC.
545 Speedvale Avenue West, Guelph, Ontario N1K 1E6, Canada, www.canadiansolar.com, support@canadiansolar.com

Figure B.9: Data sheet: Canadian Solar poly c-Si bifacial

ENGINEERING DRAWING (mm)

Rear View

Frame Cross Section A-A

Mounting Hole

CS3W-400PB-AG / I-V CURVES

■ 1000 W/m²	■ 5°C
■ 800 W/m²	■ 25°C
■ 600 W/m²	■ 45°C
■ 400 W/m²	■ 65°C
■ 200 W/m²	

ELECTRICAL DATA | STC*

		Nominal Max. Power (Pmax)	Opt. Operating Voltage (Vmp)	Opt. Operating Current (Imp)	Open Circuit Voltage (Voc)	Short Circuit Current (Isc)	Module Efficiency
CS3W-390PB-AG		390 W	38.3 V	10.19 A	46.8 V	10.74 A	17.5%
	5%	410 W	38.3 V	10.71 A	46.8 V	11.28 A	18.3%
Bifacial	10%	429 W	38.3 V	11.21 A	46.8 V	11.81 A	19.2%
Gain**	20%	468 W	38.3 V	12.23 A	46.8 V	12.89 A	20.9%
	30%	507 W	38.3 V	13.25 A	46.8 V	13.96 A	22.7%
CS3W-395PB-AG		395 W	38.5 V	10.26 A	47 V	10.82 A	17.7%
	5%	415 W	38.5 V	10.78 A	47 V	11.36 A	18.6%
Bifacial	10%	435 W	38.5 V	11.3 A	47 V	11.9 A	19.5%
Gain**	20%	474 W	38.5 V	12.31 A	47 V	12.98 A	21.2%
	30%	513 W	38.5 V	13.34 A	47 V	14.07 A	23.0%
CS3W-400PB-AG		400 W	38.7 V	10.34 A	47.2 V	10.9 A	17.9%
	5%	420 W	38.7 V	10.86 A	47.2 V	11.45 A	18.8%
Bifacial	10%	440 W	38.7 V	11.37 A	47.2 V	11.99 A	19.7%
Gain**	20%	480 W	38.7 V	12.41 A	47.2 V	13.08 A	21.5%
	30%	520 W	38.7 V	13.44 A	47.2 V	14.17 A	23.3%
CS3W-405PB-AG		405 W	38.9 V	10.42 A	47.4 V	10.98 A	18.1%
	5%	425 W	38.9 V	10.94 A	47.4 V	11.53 A	19.0%
Bifacial	10%	445 W	38.9 V	11.46 A	47.4 V	12.08 A	19.9%
Gain**	20%	486 W	38.9 V	12.5 A	47.4 V	13.18 A	21.8%
	30%	527 W	38.9 V	13.56 A	47.4 V	14.27 A	23.6%
CS3W-410PB-AG		410 W	39.1 V	10.49 A	47.6 V	11.06 A	18.3%
	5%	431 W	39.1 V	11.03 A	47.6 V	11.61 A	19.3%
Bifacial	10%	451 W	39.1 V	11.54 A	47.6 V	12.17 A	20.2%
Gain**	20%	492 W	39.1 V	12.59 A	47.6 V	13.27 A	22.0%
	30%	533 W	39.1 V	13.64 A	47.6 V	14.38 A	23.9%
CS3W-415PB-AG		415 W	39.3 V	10.56 A	47.8 V	11.14 A	18.6%
	5%	436 W	39.3 V	11.10 A	47.8 V	11.70 A	19.5%
Bifacial	10%	457 W	39.3 V	11.63 A	47.8 V	12.25 A	20.5%
Gain**	20%	498 W	39.3 V	12.67 A	47.8 V	13.37 A	22.3%
	30%	540 W	39.3 V	13.75 A	47.8 V	14.48 A	24.2%

* Under Standard Test Conditions (STC) of irradiance of 1000 W/m², spectrum AM 1.5 and cell temperature of 25°C.
** Bifacial Gain: The additional gain from the back side compared to the power of the front side at the standard test condition. It depends on mounting (structure, height, tilt angle etc.) and albedo of the ground.

ELECTRICAL DATA | NMOT*

	Nominal Max. Power (Pmax)	Opt. Operating Voltage (Vmp)	Opt. Operating Current (Imp)	Open Circuit Voltage (Voc)	Short Circuit Current (Isc)
CS3W-390PB-AG	292 W	35.8 V	8.15 A	44.1 V	8.66 A
CS3W-395PB-AG	295 W	36.0 V	8.21 A	44.3 V	8.72 A
CS3W-400PB-AG	299 W	36.2 V	8.27 A	44.5 V	8.79 A
CS3W-405PB-AG	303 W	36.3 V	8.33 A	44.7 V	8.85 A
CS3W-410PB-AG	307 W	36.5 V	8.39 A	44.8 V	8.92 A
CS3W-415PB-AG	310 W	36.7 V	8.45 A	45.0 V	8.98 A

* Under Nominal Module Operating Temperature (NMOT), irradiance of 800 W/m², spectrum AM 1.5, ambient temperature 20°C, wind speed 1 m/s.

MECHANICAL DATA

Specification	Data
Cell Type	Poly-crystalline
Cell Arrangement	144 [2 X (12 X 6)]
Dimensions	2132 × 1048 × 30 mm (83.9 × 41.3 × 1.2 in)
Weight	28.4 kg (62.6 lbs)
Front / Back Glass	2.0 mm heat strengthened glass
Frame	Anodized aluminium alloy
J-Box	IP68, 3 diodes
Cable	4.0 mm² (IEC), 12 AWG (UL)
Cable Length (Including Connector)	Portrait: 400 mm (15.7 in) (+) / 280 mm (11.0 in) (-); landscape: 1400 mm (55.1 in); leap-frog connection: 1850 mm (72.8 in)*
Connector	T4 series or H4 UTX or MC4-EVO2
Per Pallet	33 pieces
Per Container (40' HQ)	660 pieces or 561 pieces (only for US)

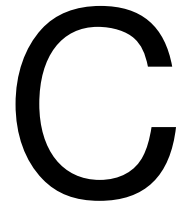* For detailed information, please contact your local Canadian Solar sales and technical representatives.

ELECTRICAL DATA

Operating Temperature	-40°C ~ +85°C
Max. System Voltage	1500 V (IEC/UL) or 1000 V (IEC/UL)
Module Fire Performance	TYPE 3 (UL 1703) or CLASS C (IEC61730)
Max. Series Fuse Rating	25 A
Application Classification	Class A
Power Tolerance	0 ~ + 10 W
Power Bifaciality*	70 %

* Power Bifaciality = Pmax_rear / Pmax_front, both Pmax_rear and Pmax_front are tested under STC, Bifaciality Tolerance: ± 5 %

* The specifications and key features contained in this datasheet may deviate slightly from our actual products due to the on-going innovation and product enhancement. Canadian Solar Inc. reserves the right to make necessary adjustment to the information described herein at any time without further notice.
Please be kindly advised that PV modules should be handled and installed by qualified people who have professional skills and please carefully read the safety and installation instructions before using our PV modules.

TEMPERATURE CHARACTERISTICS

Specification	Data
Temperature Coefficient (Pmax)	-0.36 % / °C
Temperature Coefficient (Voc)	-0.28 % / °C
Temperature Coefficient (Isc)	0.05 % / °C
Nominal Module Operating Temperature	41 ± 3°C

PARTNER SECTION

CANADIAN SOLAR INC.
545 Speedvale Avenue West, Guelph, Ontario N1K 1E6, Canada, www.canadiansolar.com, support@canadiansolar.com

May 2020. All rights reserved, PV Module Product Datasheet V5.591_EN

Figure B.10: Data sheet: Canadian Solar poly c-Si bifacial

C

Case study results

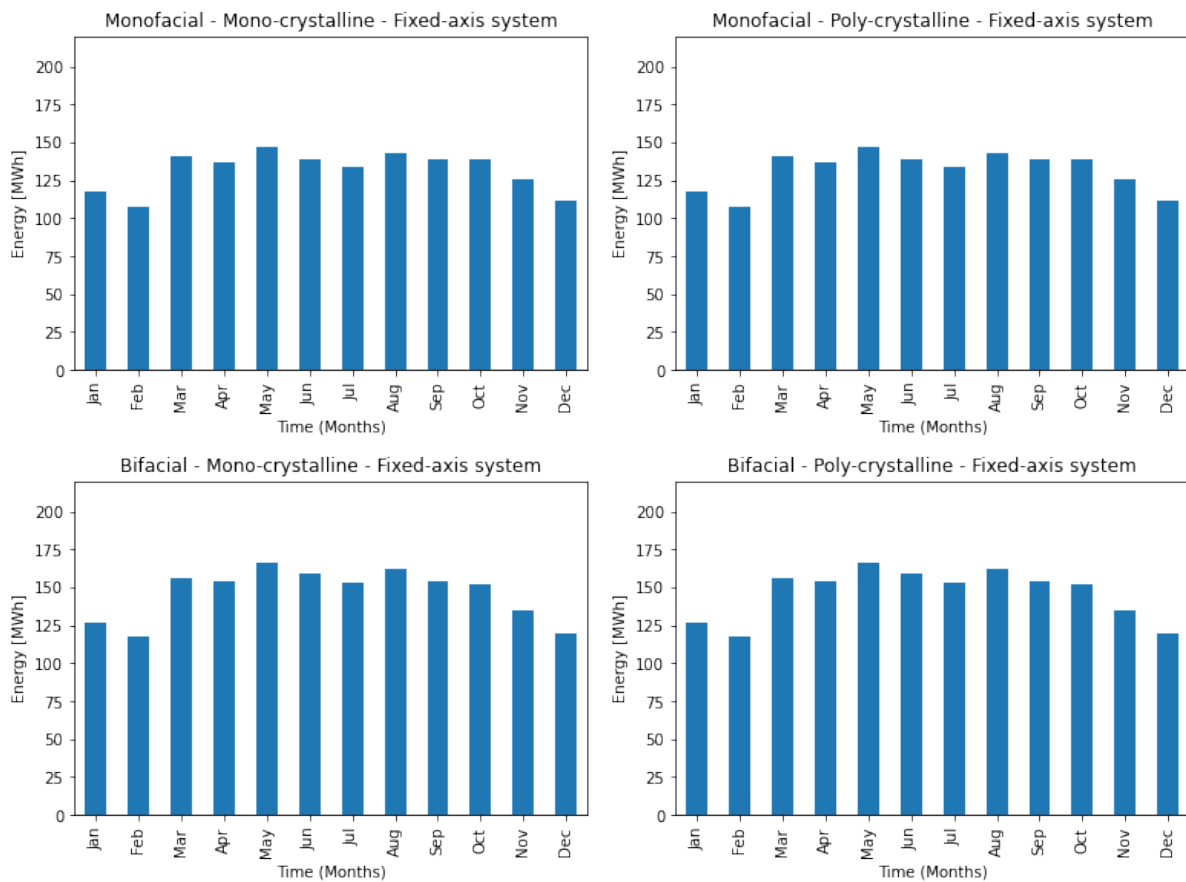## C.1. PV results: Vopak Horizon Fujairah

Figure C.1: Four different PV systems with corresponding monthly PV energy [MWh] output for a 1 MW$_p$ system in Fujairah

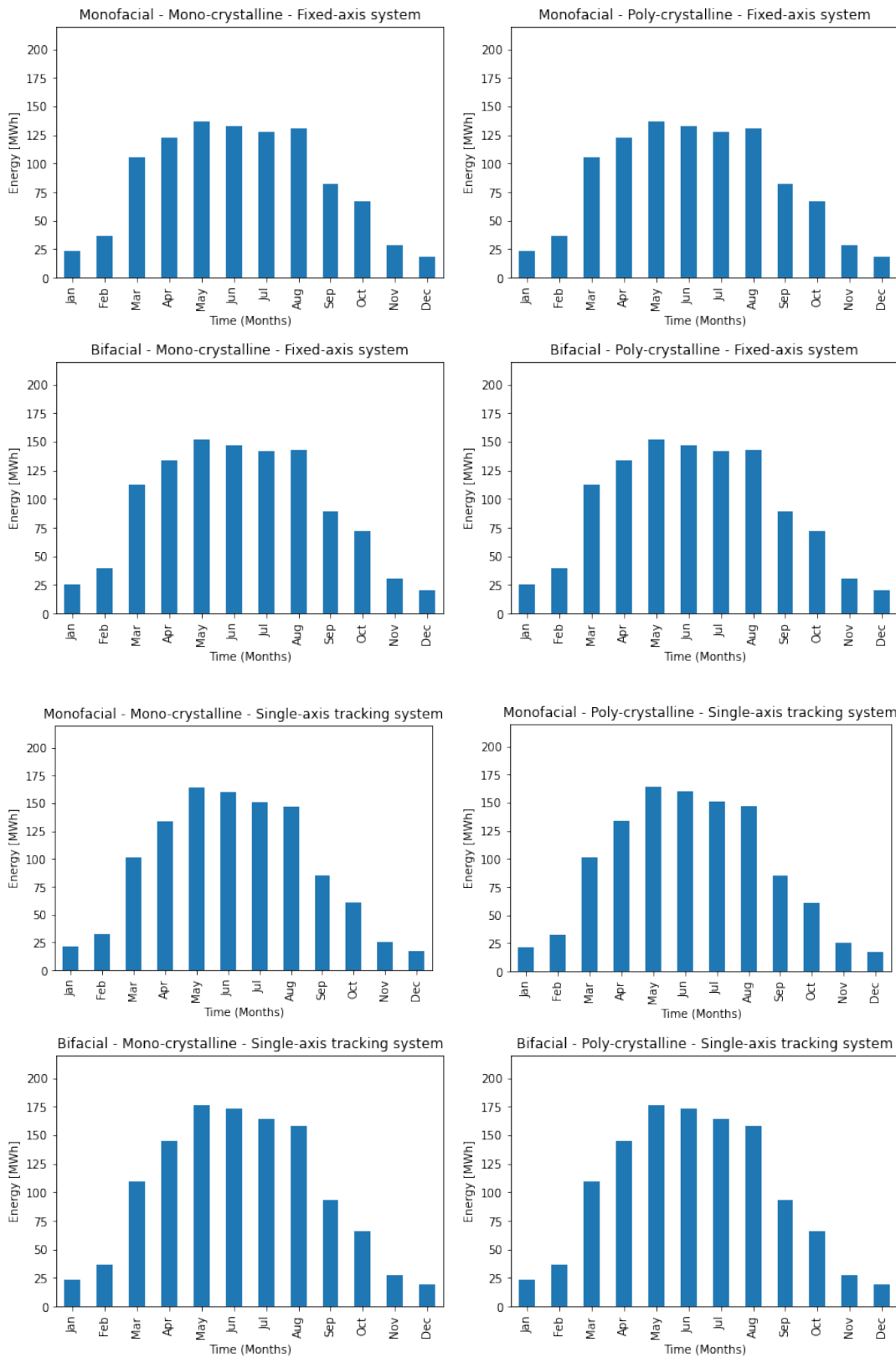## C.2. PV results: Vopak Terminal Laurenshaven

Figure C.2: Eight different PV systems with corresponding monthly PV energy [MWh] output for a 1 MW$_p$ system in Laurenshaven
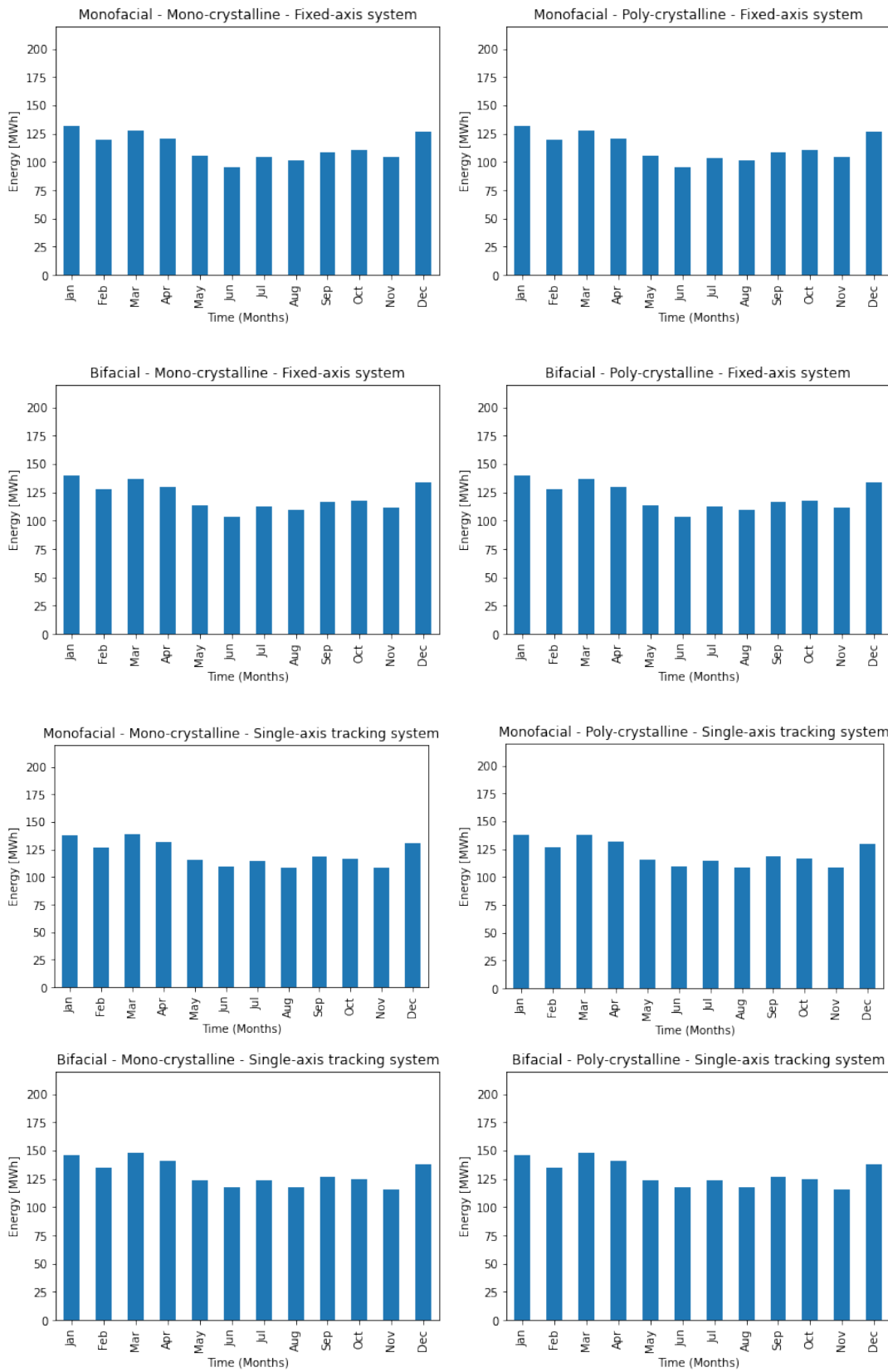
C.3. PV results: Vopak Panama

Figure C.3: Eight different PV systems with corresponding monthly PV energy [MWh] output for a 1 MW$_p$ system in Panama

C.4. Sizing results: Vopak Horizon Fujairah

(a) Energy Unmet

(b) Energy dumped

(c) System cost

(d) Feasible solutions
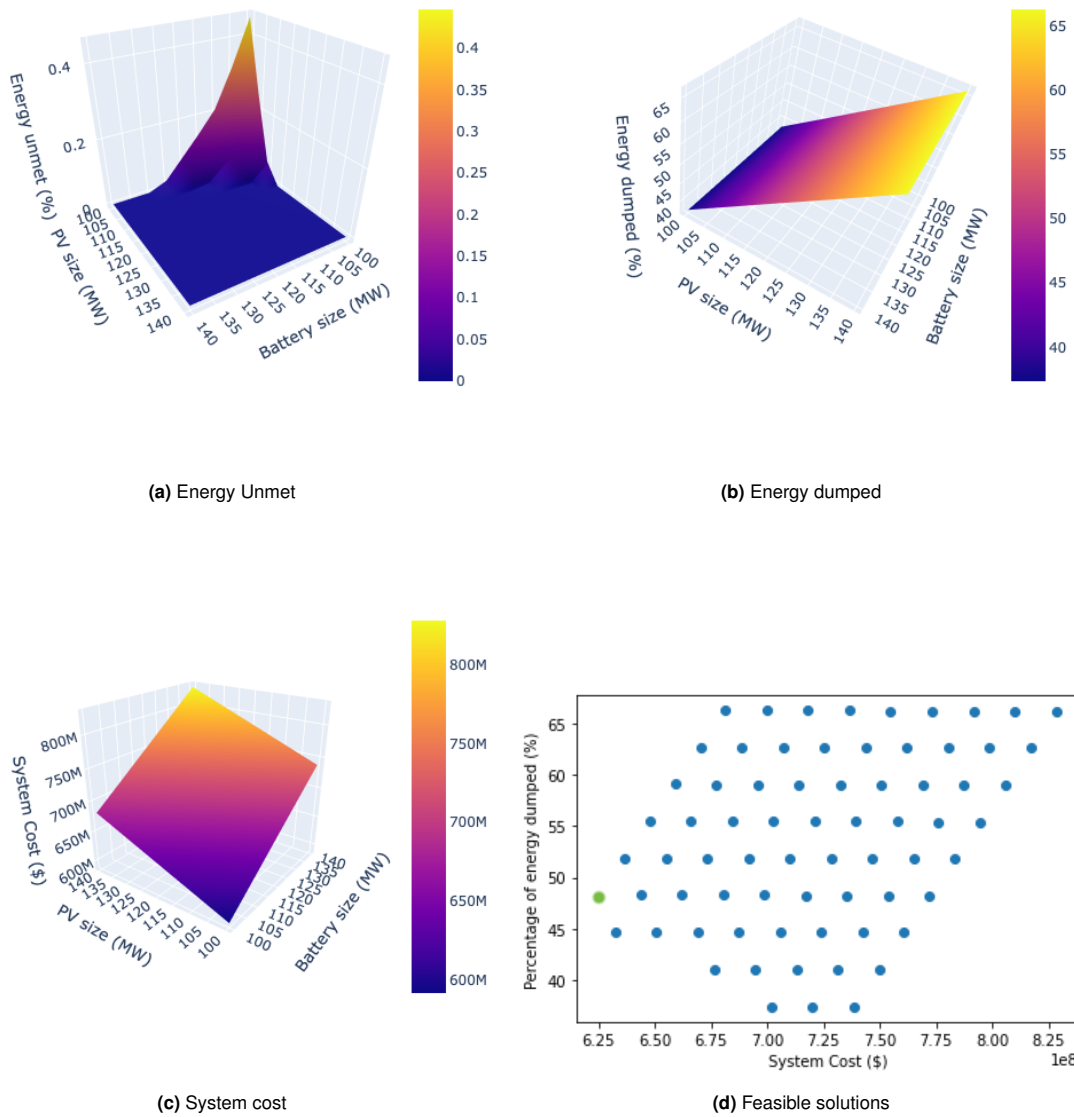
Figure C.4: The output from the sizing approach for the technology with the lowest LCOSS, the green dot is the system size selected with the lowest system cost and is able to satisfy the load for VHF

C.5. Sizing results: Vopak Terminal Laurenshaven

(a) Energy Unmet

(b) Energy dumped

(c) System cost

(d) Feasible solutions
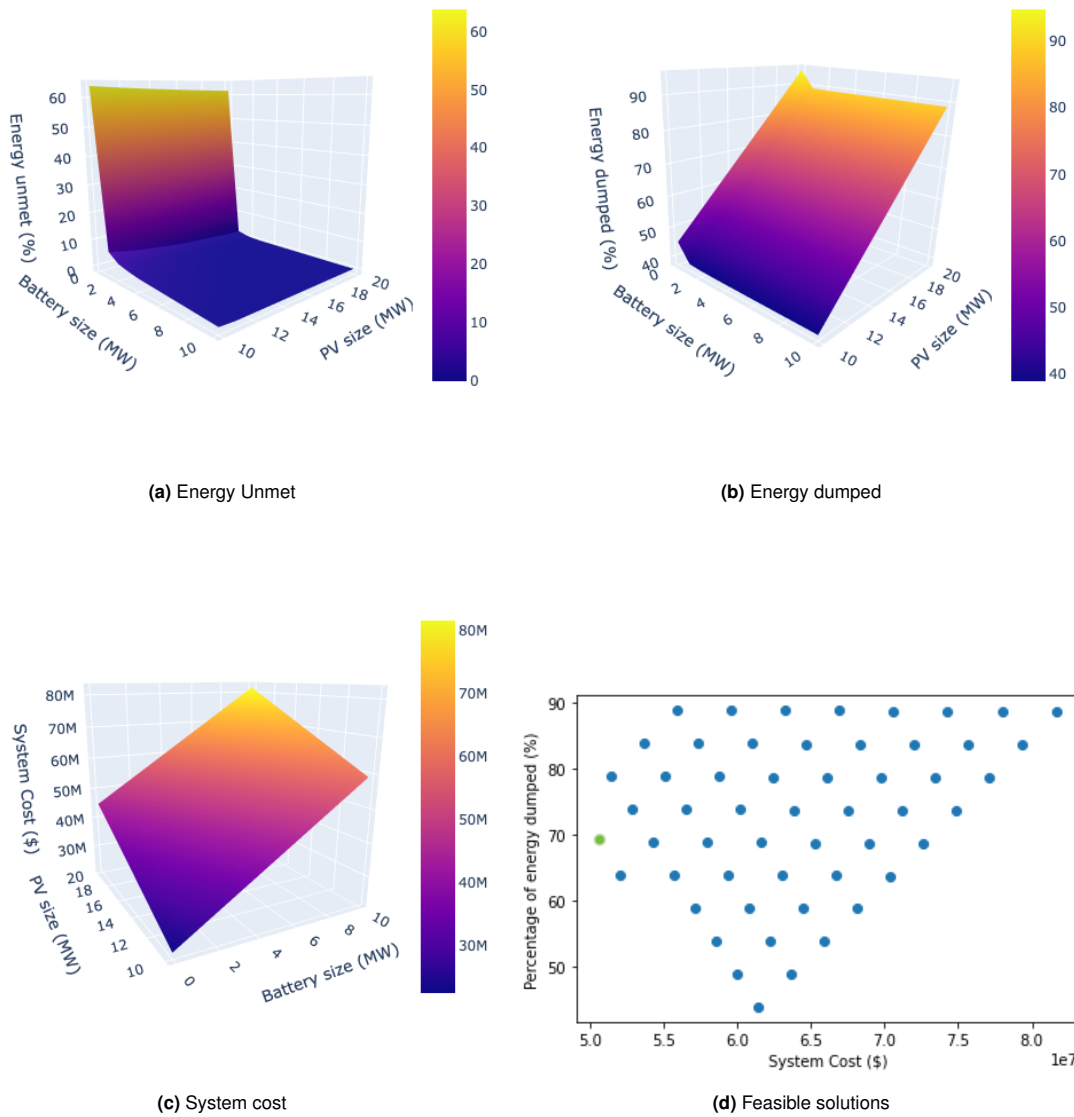
Figure C.5: The output from the sizing approach for the technology with the lowest LCOSS, the green dot is the system size selected with the lowest system cost and is able to satisfy the load for VTL

C.6. Sizing results: Vopak Panama

(a) Energy Unmet

(b) Energy dumped
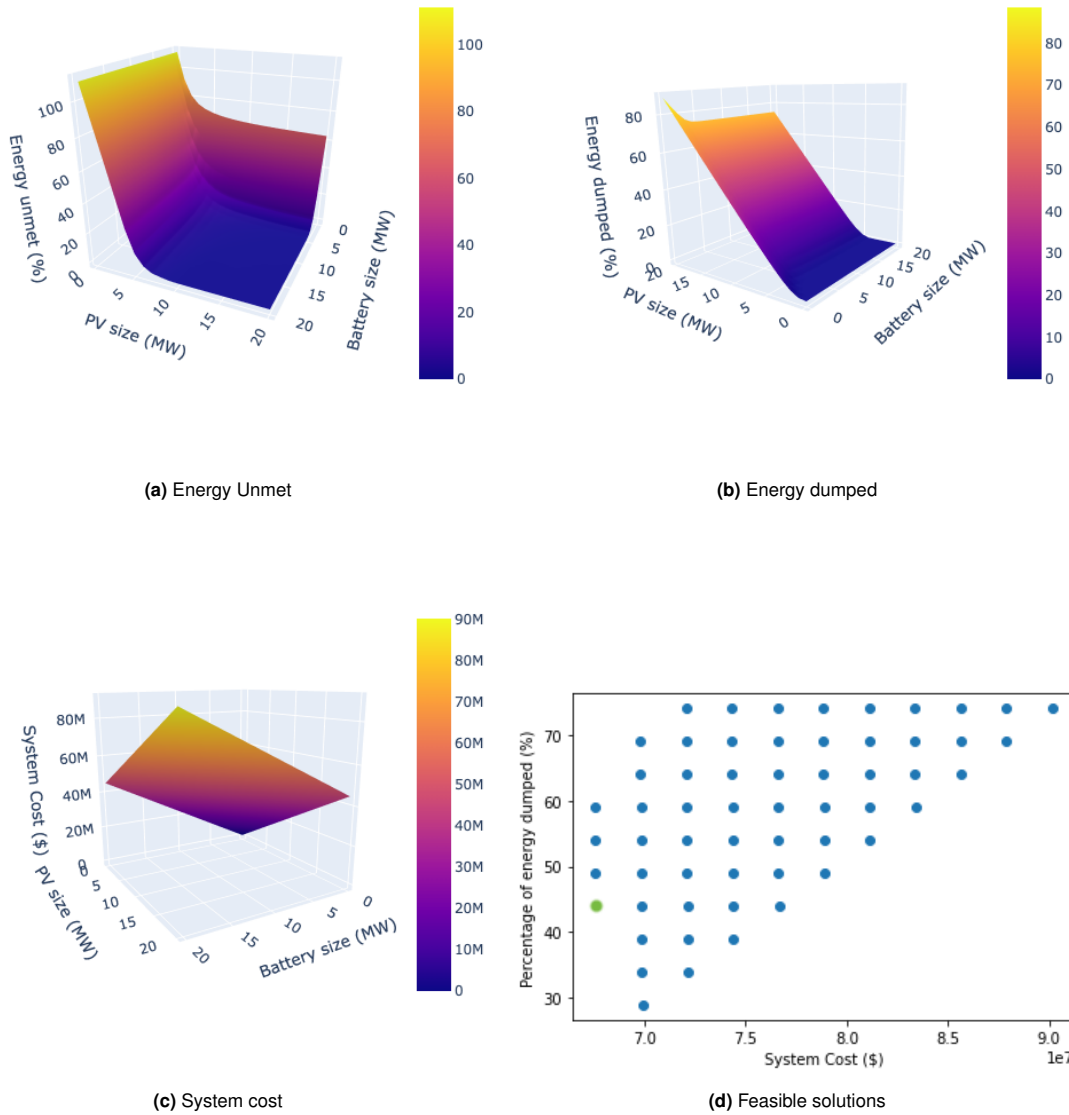

(c) System cost

(d) Feasible solutions

Figure C.6: The output from the sizing approach for the technology with the lowest LCOSS, the green dot is the system size selected with the lowest system cost and is able to satisfy the load for Vopak Panama

References

A. Mikofski, M., Darawali, R., Hamer, M., Neubert, A., & Newmiller, J. (2019). *Bifacial Performance Modeling in Large Arrays*. 2019 IEEE 46th Photovoltaic Specialists Conference (PVSC)IEEE.

Abdalla, A. H., Oseghale, C. I., Gil Posada, J. O., & Hall, P. J. (2016). Rechargeable nickel–iron batteries for large-scale energy storage. *IET Renewable Power Generation*, *10*(10), 1529–1534. https://doi.org/10.1049/iet-rpg.2016.0051

Abdin, Z., & Khalilpour, K. R. (2018). Single and polystorage technologies for renewable-based hybrid energy systems. *Polygeneration with Polystorage: For Chemical and Energy Hubs*, 77–131. https://doi.org/10.1016/B978-0-12-813306-4.00004-5

Abedin, A. H., & Rosen, M. A. (2011). *A Critical Review of Thermochemical Energy Storage Systems* (tech. rep.).

ADB. (2018). *Handbook on Battery Energy Storage System* (tech. rep.). Asian Development Bank. Manila, Philippines. https://doi.org/10.22617/TCS189791-2

Adeeb, J., Farhan, A., & Al-Salaymeh, A. (2019). Temperature effect on performance of different solar cell technologies. *Journal of Ecological Engineering*, *20*(5), 249–254. https://doi.org/10.12911/22998993/105543

Airvers. (2022). The first mass production line of the world's largest power "Ronghe No. 1" iron-chromium flow battery was completed and put into production.

Aldersey-Williams, J., & Rubert, T. (2019). Levelised cost of energy – A theoretical justification and critical assessment. *Energy Policy*, *124*, 169–179. https://doi.org/10.1016/J.ENPOL.2018.10.004

Alnaimat, F., & Rashid, Y. (2019). Thermal Energy Storage in Solar Power Plants: A Review of the Materials, Associated Limitations, and Proposed Solutions. *Energies*, *12*(21), 4164. https://doi.org/10.3390/en12214164

Alotto, P., Guarnieri, M., & Moro, F. (2014). Redox flow batteries for the storage of renewable energy: A review. https://doi.org/10.1016/j.rser.2013.08.001

Alva, G., Lin, Y., & Fang, G. (2018). An overview of thermal energy storage systems. *Energy*, *144*, 341–378. https://doi.org/10.1016/J.ENERGY.2017.12.037

Alva, G., Liu, L., Huang, X., & Fang, G. (2017). Thermal energy storage materials and systems for solar energy applications. *Renewable and Sustainable Energy Reviews*, *68*, 693–706. https://doi.org/10.1016/j.rser.2016.10.021

Ameli, N., Dessens, O., Winning, M., Cronin, J., Chenet, H., Drummond, P., Calzadilla, A., Anandarajah, G., & Grubb, M. (2021). Higher cost of finance exacerbates a climate investment trap in developing economies. https://doi.org/10.1038/s41467-021-24305-3

Andino García, H., Reyes Duke, A., & Villatoro Flores, H. (2021). Techno-economic comparison between photovoltaic systems with solar trackers and fixed structure in "el Valle de Sula", Honduras. *IOP Conference Series: Earth and Environmental Science*, *776*(1). https://doi.org/10.1088/1755-1315/776/1/012011

Apostoleris, H., Al Ghaferi, A., & Chiesa, M. (2021). What is going on with Middle Eastern solar prices, and what does it mean for the rest of us? *Progress in Photovoltaics: Research and Applications*, *29*(6), 638–648. https://doi.org/10.1002/PIP.3414

Arabkoohsar, A. (2021). Classification of energy storage systems. *Mechanical Energy Storage Technologies*, 1–12. https://doi.org/10.1016/B978-0-12-820023-0.00001-8

Ardani, K., O'shaughnessy, E., Fu, R., Mcclurg, C., Huneycutt, J., & Margolis, R. (2016). Installed Cost Benchmarks and Deployment Barriers for Residential Solar Photovoltaics with Energy Storage: Q1 2016. www.nrel.gov/publications.

Astolfi, M. (2017). Technical options for Organic Rankine Cycle systems. *Organic Rankine Cycle (ORC) Power Systems: Technologies and Applications*, 67–89. https://doi.org/10.1016/B978-0-08-100510-1.00003-X

Baharoon, D. A., Rahman, H. A., Omar, W. Z. W., & Fadhl, S. O. (2015). Historical development of concentrating solar power technologies to generate clean electricity efficiently–A review. *Renewable and Sustainable Energy Reviews*, *41*, 996–1027.

Bandyopadhyay, S., Mouli, G. R. C., Qin, Z., Elizondo, L. R., & Bauer, P. (2020). Techno-Economical Model Based Optimal Sizing of PV-Battery Systems for Microgrids. *IEEE Transactions on Sustainable Energy*, *11*(3), 1657–1668. https://doi.org/10.1109/TSTE.2019.2936129

Barbosa, C. (2020). "New Regulations for End-of-Life PV Modules.

Baumgartner, F. (2017). *Photovoltaic (PV) balance of system components: Basics, performance*. Woodhead Publishing. https://www.sciencedirect.com/science/article/pii/B9781782423362000057

Benda, V., & Černá, L. (2020). PV cells and modules – State of the art, limits and trends. *Heliyon*, *6*(12). https://doi.org/10.1016/J.HELIYON.2020.E05666

Berrada, A., Loudiyi, K., & El Mrabet, R. (2021). *Chapter 1 - Introduction to hybrid energy systems* (A. Berrada & R. El Mrabet, Eds.). Academic Press. https://doi.org/https://doi.org/10.1016/B978-0-12-821403-9.00001-9

Besarati, S. M., & Goswami, D. Y. (2017). Supercritical CO2 and other advanced power cycles for concentrating solar thermal (CST) systems. *Advances in Concentrating Solar Thermal Research and Technology*, 157–178. https://doi.org/10.1016/B978-0-08-100516-3.00008-3

Blanc, C., & Rufer, A. (2010). Understanding the Vanadium Redox Flow Batteries. *Paths to sustainable energy*. InTech. https://doi.org/10.5772/13338

Blanc, P., Espinar, B., Geuder, N., Gueymard, C., Meyer, R., Pitz-Paal, R., Reinhardt, B., Renné, D., Sengupta, M., Wald, L., & Wilbert, S. (2014). Direct normal irradiance related definitions and applications: The circumsolar issue. *Solar Energy*, 561–577. https://doi.org/https://doi.org/10.1016/j.solener.2014.10.001

Boelens, M., Koch, C., Pastoria, C., & Woodle, N. (2022). Decommissioning Trends, Circular Economy Policy Incentives, and Secondary Markets for Solar Photovoltaics.

Boersma, T. (2020). *Reforming Energy Subsidies-Initial Lessons from the United Arab Emirates* (tech. rep.). https://www.researchgate.net/publication/301549576

Bolen, M., & Libby, C. (2018). *PV Plant Decommissioning Salvage Value Conceptual Cost Estimate* (tech. rep.). www.epri.com

Breeze, P. (2018a). Large-Scale Batteries. *Power system energy storage technologies* (pp. 33–45). Elsevier. https://doi.org/10.1016/b978-0-12-812902-9.00004-3

Breeze, P. (2018b). Stirling Engines and Free Piston Engines. *Piston Engine-Based Power Plants*, 59–70. https://doi.org/10.1016/B978-0-12-812904-3.00006-9

Breeze, P. (2019). Power System Energy Storage Technologies. *Power Generation Technologies*, 219–249. https://doi.org/10.1016/B978-0-08-102631-1.00010-9

Bruch, M., & Müller, M. (2014). Calculation of the cost-effectiveness of a PV battery system. *Energy Procedia*, *46*, 262–270. https://doi.org/10.1016/J.EGYPRO.2014.01.181

Brushett, F. R., Aziz, M. J., & Rodby, K. E. (2020). On Lifetime and Cost of Redox-Active Organics for Aqueous Flow Batteries. https://doi.org/10.1021/acsenergylett.0c00140

Buchmann, I. (2016). *Batteries in a Portable World - A Handbook on Rechargeable Batteries for Non-Engineers* (4th).

Burke, A., Miller, M., Zhao, H., Org, E., & Zhao, H. (2012). *UC Davis Research Reports Title Fast Charging Tests (up to 6C) of Lithium Titanate Cells and Modules: Electrical and Thermal Response Fast charging tests (up to 6C) of lithium titanate cells and modules: electrical and thermal response* (tech. rep.). www.its.ucdavis.edu

Caraballo, A., Galán-Casado, S., Caballero, Á., & Serena, S. (2021). Molten Salts for Sensible Thermal Energy Storage: A Review and an Energy Performance Analysis. *Energies*, *14*(4), 1197. https://doi.org/10.3390/en14041197

Castillo, L. R. (2014). *Techno-economic Analysis of Combined Hybrid Concentrating Solar and Photovoltaic Power Plants: a case study for optimizing solar energy integration into the South African electricity grid* (tech. rep.). KTH School of Industrial Engineering and Management.

CEER. (2017). Report on Power Losses. https://www.ceer.eu/documents/104400/-/-/6f455336-d8c8-aa6f-

Chakraborty, S., Sadhu, P. K., & Pal, N. (2015). Technical mapping of solar <scp>PV</scp> for <scp>ISM</scp> -an approach toward green campus. *Energy Science & Engineering*, *3*(3), 196–206. https://doi.org/10.1002/ese3.65

Cole, W., Frazier, A. W., & Augustine, C. (2021). *Cost Projections for Utility-Scale Battery Storage: 2021 Update* (tech. rep.). www.nrel.gov/publications.

Curtis, T., Heath, G., Walker, A., Desai, J., Settle, E., & Barbosa, C. (2021). Best Practices at the End of the Photovoltaic System Performance Period. https://www.nrel.gov/docs/fy21osti/78678.pdf.

Dambhare, M. V., Butey, B., & Moharil, S. V. (2021). Solar photovoltaic technology: A review of different types of solar cells and its future trends. *Journal of Physics: Conference Series*, *1913*(1). https://doi.org/10.1088/1742-6596/1913/1/012053

Das, A. B. (2014). Middle East Solar Industry Association: A Guide to Solar Power Generation in the United Arab Emirates Solar for Students.

Dash, P., & Gupta, N. C. (2015). Effect of Temperature on Power Output from Different Commercially available Photovoltaic Modules. *Int. Journal of Engineering Research and Applications*. https://www.researchgate.net/publication/279497414_Effect_of_Temperature_on_Power_Output_from_Different_Commercially_available_Photovoltaic_Modules

Deline, C., Ayala Peláez, S., Marion, B., Sekulic, B., Woodhouse, M., & Stein, J. (2019). Bifacial PV System Performance: Separating Fact from Fiction.

Dobos, A. P. (2014). *PVWatts Version 5 Manual* (tech. rep.). http://developer.nrel.gov

Dobos, E. (2005). Albedo. https://doi.org/10.1201/NOE0849338304.ch15

DOE. (n.d.). 2030 Solar Cost Targets. https://www.energy.gov/eere/solar/articles/2030-solar-cost-targets

DOE. (2020). 2020 Grid Energy Storage Technology Cost and Performance Assessment. *Technical Report - U.S. Department of Energy*.

DOE. (2021). Energy Efficiency & Renewable Energy. https://www.energy.gov/eere/solar/

DOE. (2022). Perovskite Solar Cells. https://www.energy.gov/eere/solar/perovskite-solar-cells

EASE. (2016). *Energy Storage Technology Description* (tech. rep.). European Associaton for Storage of Energy. www.ease-storage.eu

Elestor. (2022). *Elestor: electricity storage at an unrivalled cost level Content* (tech. rep.).

Falcone, P. K. (1986). A handbook for solar central receiver design.

Feldman, D., Ramasamy, V., Fu, R., Ramdas, A., Desai, J., & Margolis, R. (2020). *U.S. Solar Photovoltaic System and Energy Storage Cost Benchmark: Q1 2020* (tech. rep.). www.nrel.gov/publications.

Ferrari, J. (2021). Energy storage and conversion. *Electric utility resource planning* (pp. 73–107). Elsevier. https://doi.org/10.1016/b978-0-12-819873-5.00003-4

Fiedler, F., & Matas, J. C. (2022). Techno-Economic Analysis of Grid-Connected PV Battery Solutions for Holiday Homes in Sweden. https://doi.org/10.3390/en15082838

Flueckiger, S. M., & Garimella, S. V. (2014). Latent heat augmentation of thermocline energy storage for concentrating solar power – A system-level assessment. *Applied Energy*, *116*, 278–287. https://doi.org/10.1016/j.apenergy.2013.11.059

Fraunhofer ISE. (2021). Photovoltaics Report. https://www.ise.fraunhofer.de/content/dam/ise/de/documents/publications/studies/Photovoltaics-Report.pdf

Galione, P., Pérez-Segarra, C., Rodríguez, I., Oliva, A., & Rigola, J. (2015). Multi-layered solid-PCM thermocline thermal storage concept for CSP plants. Numerical analysis and perspectives. *Applied Energy*, *142*, 337–351. https://doi.org/10.1016/j.apenergy.2014.12.084

Gil, A., Medrano, M., Martorell, I., Lázaro, A., Dolado, P., Zalba, B., & Cabeza, L. F. (2010). State of the art on high temperature thermal energy storage for power generation. Part 1—Concepts, materials and modellization. *Renewable and Sustainable Energy Reviews*, *14*(1), 31–55. https://doi.org/10.1016/J.RSER.2009.07.035

Gladysz, G. M., & Chawla, K. K. (2015). Applications. *Voids in Materials*, 131–156. https://doi.org/10.1016/B978-0-444-56367-5.00007-5

Glatzmaier, G. (2011). *Summary Report for Concentrating Solar Power Thermal Storage Workshop: New Concepts and Materials for Thermal Energy Storage and Heat-Transfer Fluids, May 20, 2011* (tech. rep.). http://www.osti.gov/bridge

Greentech Media. (2018). What Does 100 Gigawatts per Year of Solar Look Like? https://www.greentechmedia.com/squared/the-lead/what-100-gigawatts-of-solar-per-year-looks-like

Gupta, M., Kumar, B., Wankhade, M., Choudhary, M., Singh, A., Tiwari, A., Soni, N., Shrivastava, N., & Bisen. (2016). Azimuth-Altitude Dual Axis Solar Tracker, 26–30.

Han, X., Garrison, J., & Hug, G. (2022). Techno-economic analysis of PV-battery systems in Switzerland. *Renewable and Sustainable Energy Reviews*, *158*, 112028. https://doi.org/10.1016/J.RSER.2021.112028

Hansen, C., & Stein, J. S. (2012). Effect of Time Scale on Analysis of PV System Performance PVSENSOR-A comprehensive evaluation of irradiance sensors View project Voltage Regulation and Protection Assurance using DER Advanced Grid Functions View project. https://doi.org/10.13140/2.1.1150.3368

Hasan Shah, A., Hassan, A., Shakeel Laghari, M., & Alraeesi, A. (2020). The Influence of Cleaning Frequency of Photovoltaic Modules on Power Losses in the Desert Climate. *MDPI*. https://doi.org/10.3390/su12229750

Hesse, H. C., Schimpe, M., Kucevic, D., & Jossen, A. (2017). Lithium-ion battery storage for the grid - A review of stationary battery storage system design tailored for applications in modern power grids. https://doi.org/10.3390/en10122107

Hildebrandt A F, & Vant-Hull, L. L. (1977). Power with heliostats. *Science*, *197*. https://doi.org/10.1126/science.197.4309.1139

Ho, C. K. (2017). Advances in central receivers for concentrating solar applications. *Solar Energy*, 38–56. https://doi.org/https://doi.org/10.1016/j.solener.2017.03.048

Holmgren, W. F., Hansen, C. W., & Mikofski, M. A. (2018). pvlib python: a python package for modeling solar energy systems. *Journal of Open Source Software*, *3*(29), 884. https://doi.org/10.21105/JOSS.00884

Hugo, Y., Kout, W., & Dalessi, G. (2016). The hydrogen bromine flow batery for a large-scale integration of variable renewable electricity: State-of-the-art review. *Elestor*.

Hunter, S. R., Smith, D. B., Polizos, G., Schaeffer, D. A., Lee, D. F., & Datskos, P. G. (2014). Low cost anti-soiling coatings for CSP collector mirrors and heliostats. *High and Low Concentrator Systems for Solar Energy Applications IX*, *9175*, 91750J. https://doi.org/10.1117/12.2061845

IE. (2010). *Guidelines for PV power measurement in industry*. Institute of Energy: Publications Office.

IEA. (2014). Technology Roadmap - Solar Thermal Electricity 2014. https://www.iea.org/reports/technology-roadmap-solar-thermal-electricity-2014

IEA. (2022). Special Report on Solar PV Global Supply Chains. www.iea.org/t&c/

IRENA. (2017). *ELECTRICITY STORAGE AND RENEWABLES: COSTS AND MARKETS TO 2030 ELECTRICITY STORAGE AND RENEWABLES: COSTS AND MARKETS TO 2030*. International Renewable Energy Agency. www.irena.org

IRENA. (2021). *Renewable Power Generation Costs 2020*. www.irena.org

IRENA, The World Bank, & CIF. (2020). *CONCENTRATING SOLAR POWER CLEAN POWER ON DEMAND 24/7* (tech. rep.). www.worldbank.org

Iron Edison. (2016). *Nickel Iron Battery: Industrial-series for Renewable Energy & Backup Power applications* (tech. rep.).

Isabella, O. (2021). Finding the Optimal Tilt Angle. *PV3x Solar Energy Engineering: Photovoltaic Systems*. https://www.youtube.com/watch?v=WFqL9kDsjuc

Islam, M. T., Huda, N., Abdullah, A. B., & Saidur, R. (2018). A comprehensive review of state-of-the-art concentrating solar power (CSP) technologies: Current status and research trends. *Renewable and Sustainable Energy Reviews*, *91*, 987–1018. https://doi.org/https://doi.org/10.1016/j.rser.2018.04.097

JenaBatteries. (2020). Datasheet JenaBatteries.

Jordan, D. C., Kurtz, S. R., VanSant, K., & Newmiller, J. (2016). Compendium of photovoltaic degradation rates. *Progress in Photovoltaics: Research and Applications*, *24*(7), 978–989. https://doi.org/10.1002/PIP.2744/FULL

Kalaiselvam, S., & Parameshwaran, R. (2014a). Latent Thermal Energy Storage. *Thermal Energy Storage Technologies for Sustainability*, 83–126. https://doi.org/10.1016/B978-0-12-417291-3.00005-0

Kalaiselvam, S., & Parameshwaran, R. (2014b). Sensible Thermal Energy Storage. *Thermal Energy Storage Technologies for Sustainability*, 65–81. https://doi.org/10.1016/B978-0-12-417291-3.00004-9

Killer, M., Farrokhseresht, M., & Paterakis, N. G. (2020). Implementation of large-scale Li-ion battery energy storage systems within the EMEA region. https://doi.org/10.1016/j.apenergy.2019.114166

Kim, J., Suharto, Y., & Daim, T. U. (2017). Evaluation of Electrical Energy Storage (EES) technologies for renewable energy: A case from the US Pacific Northwest. *Journal of Energy Storage*, *11*, 25–54. https://doi.org/10.1016/J.EST.2017.01.003

King, D. L., Boyson, W. E., & Kratochvill, J. A. (2004). *SANDIA REPORT Photovoltaic Array Performance Model* (tech. rep.). http://www.ntis.gov/help/ordermethods.asp?loc=7-4-0#online

Kolbeck, H. (2022). Decommissioning solar energy systems.

Kolhe, M. (2009). Techno-economic optimum sizing of a stand-alone solar photovoltaic system. *IEEE Transactions on Energy Conversion*, *24*(2), 511–519. https://doi.org/10.1109/TEC.2008.2001455

Kosmadakis, I. E., Elmasides, C., Eleftheriou, D., & Tsagarakis, K. P. (2019). A techno-economic analysis of a pv-battery system in Greece. *Energies*, *12*(7). https://doi.org/10.3390/en12071357

Kuravi, S., Trahan, J., Goswami, D. Y., Rahman, M. M., & Stefanakos, E. K. (2013). Thermal energy storage technologies and systems for concentrating solar power plants. *Progress in Energy and Combustion Science*, *39*(4), 285–319. https://doi.org/10.1016/j.pecs.2013.02.001

Lane, C. (2022). What is a solar tracker and is it worth the investment? *SolarReviews*.

LevelTen Energy. (2022). European renewable PPA prices up 11% q/q and 51% y/y. https://renewablesnow.com/news/european-renewable-ppa-prices-up-11-qq-and-51-yy-levelten-energy-801495/

Lim, T. M., Ulaganathan, M., & Yan, Q. (2015). Advances in membrane and stack design of redox flow batteries (RFBs) for medium- and large-scale energy storage. *Advances in Batteries for Medium and Large-Scale Energy Storage: Types and Applications*, 477–507. https://doi.org/10.1016/B978-1-78242-013-2.00014-5

Lin, G., Chong, P., Yarlagadda, V., Nguyen, T., Wycisk, R. J., Pintauro, P. N., Bates, M., Mukerjee, S., Tucker, M. C., & Weber, A. Z. (2016). Advanced Hydrogen-Bromine Flow Batteries with Improved Efficiency, Durability and Cost. *Journal of The Electrochemical Society*, *163*(1), A5049–A5056. https://doi.org/10.1149/2.0071601jes

Liu, M., Steven Tay, N. H., Bell, S., Belusko, M., Jacob, R., Will, G., Saman, W., & Bruno, F. (2016). Review on concentrating solar power plants and new developments in high temperature thermal energy storage technologies. *Renewable and Sustainable Energy Reviews*, *53*, 1411–1432. https://doi.org/10.1016/J.RSER.2015.09.026

Lorenzo, E., Narvarte, L., & Muñoz, J. (2011). *Tracking and back-tracking* (tech. rep.). http://www.acciona-ener-

Maatallah, T., El Alimi, S., & Nassrallah, S. B. (2011). Performance modeling and investigation of fixed, single and dual-axis tracking photovoltaic panel in Monastir city, Tunisia. *Renewable and Sustainable Energy Reviews*, *15*(8), 4053–4066. https://doi.org/10.1016/J.RSER.2011.07.037

Marion, B., Adelstein, J., Boyle, K., Hayden, H., Hammond, B., Fletcher, T., Canada, B., Narang, D., Shugar, D., Wenger, H., Kimber, A., Mitchell, L., Rich, G., & Townsend, T. (2005). Performance Parameters for Grid-Connected PV Systems. www.task2.org.

Marion, B., Macalpine, S., Deline, C., Asgharzadeh, A., Toor, F., Riley, D., Stein, J., & Hansen, C. (2017). *A Practical Irradiance Model for Bifacial PV Modules Preprint A Practical Irradiance Model for Bifacial PV Modules* (tech. rep.). http://www.osti.gov/scitech

Merchán, R. P., Santos, M. J., Medina, A., & Hernández, A. (2022). High temperature central tower plants for concentrated solar power: 2021 overview. *Renewable and Sustainable Energy Reviews*.

Messadi, A., & Timoumi, Y. (2018). Improvement of the Solar Rankine Cycle Applying to the Solar Power Station: Solar II. *Innovative Energy & Research*, *07*(02). https://doi.org/10.4172/2576-1463.1000198

Meteoblue. (2022). Simulated historical climate & weather data. https://www.meteoblue.com/en/weather/historyclimate/climatemodelled/9.230N-79.490E

Meteonorm. (2014). Meteotest.

Metz, A., Fischer, M., & Trube, J. (2017a). Crystalline Silicon Technology - Current Status and Outlook. *International Technology Roadmap for Photovoltaics (ITRPV)*. https://etip-pv.eu/publications/etip-pv-publications/download/international-technology-roadmap-for-photovoltaics

Metz, A., Fischer, M., & Trube, J. (2017b). *International Technology Roadmap for Photovoltaics (ITRPV) 8th edition* (tech. rep.). PV Manufacturing in Europe Conference. Brussels.

Mexis, I., & Todeschini, G. (2020). Battery energy storage systems in the united kingdom: A review of current state-of-the-art and future applications. https://doi.org/10.3390/en13143616

Mongird, K., Viswanathan, V., Balducci, P., Alam, J., Fotedar, V., Koritarov, V., & Hadjerioua, B. (2020). An evaluation of energy storage cost and performance characteristics. https://doi.org/10.3390/en13133307

Montes, M. J., Abbas, R., Muñoz, M., Muñoz-Antón, J., & Martínez-Val, J. M. (2017). Advances in the linear Fresnel single-tube receivers: Hybrid loops with non-evacuated and evacuated receivers. *Energy Conversion and Management*, *149*, 318–333. https://doi.org/https://doi.org/10.1016/j.enconman.2017.07.031

Moya, E. Z. (2021). Chapter 7 - Parabolic-trough concentrating solar power (CSP) systems. *Concentrating solar power technology* (Second Edition, pp. 219–266). Woodhead Publishing. https://doi.org/https://doi.org/10.1533/9780857096173.2.197

MPUC. (2018). Solar and Wind Decommissioning Working Group Report and Recommendations.

Mulder, F. M., Weninger, B. M. H., Middelkoop, J., Ooms, F. G. B., & Schreuders, H. (2017). Efficient electricity storage with a battolyser, an integrated Ni–Fe battery and electrolyser. *Energy & Environmental Science*, *10*(3), 756–764. https://doi.org/10.1039/C6EE02923J

Müller-Steinhagen, H., & Trieb, F. (2004). *Concentrating solar power* (tech. rep.). Stuttgart.

Namovicz, C. (2013). Assessing the Economic Value of New Utility-Scale Renewable Generation Projects.

Narayan, N., Chamseddine, A., Vega-Garita, V., Qin, Z., Popovic-Gerber, J., Bauer, P., & Zeman, M. (2019). Exploring the boundaries of Solar Home Systems (SHS) for off-grid electrification: Optimal SHS sizing for the multi-tier framework for household electricity access. *Applied Energy*, *240*, 907–917. https://doi.org/10.1016/j.apenergy.2019.02.053

Nazzal, Y., Barbulescu, A., Howari, F., Yousef, A., Al-Taani, A. A., Al Aydaroos, F., & Naseem, M. (2019). New insights on sand dust storm from historical records, UAE. *Arabian Journal of Geosciences*, *12*(13). https://doi.org/10.1007/s12517-019-4555-1

Nekeman, O. (2014). Exploration into methods of how to solve a Python problem? *Journal of 't Paviljoen*, *8*. https://doi.org/10.1007/s40279-013-0103-4

Niclas, D. (2015). Solar energy storage: part 6 - Flow Battery: features and types.

Nkuriyingoma, O., Özdemir, E., & Sezen, S. (2022). Techno-economic analysis of a PV system with a battery energy storage system for small households: A case study in Rwanda. *Frontiers in Energy Research*, *10*. https://doi.org/10.3389/fenrg.2022.957564

NREL. (2022). Best Research-Cell Efficiency Chart. https://www.nrel.gov/pv/cell-efficiency.html

NREL, Feldman, D., Ramasamy, V., Fu, R., Ramdas, A., Desai, J., & Margolis, R. (2020). *U.S. Solar Photovoltaic System and Energy Storage Cost Benchmark: Q1 2020* (tech. rep.). www.nrel.gov/publications.

Patel, P. (2021). Sodium-Ion Batteries Poised to Pick Off Large-Scale Lithium-Ion Applications.

Perez, R., Seals, R., Ineichen, P., Stewart, R., & Menicucci, D. (1987). A new simplified version of the perez diffuse irradiance model for tilted surfaces. *Solar Energy*, *39*(3), 221–231. https://doi.org/10.1016/S0038-092X(87)80031-2

Persson, F. (2020). *Energy Storage for Stationary Applications-A Comparative, Techno-Economical Investigation* (tech. rep.).

Platzer, W. J., Mills, D., & Gardner, W. (2021). Chapter 6 - Linear Fresnel Collector (LFC) solar thermal technology. *Concentrating solar power technology* (Second Edition, pp. 165–217). https://doi.org/https://doi.org/10.1016/B978-0-12-819970-1.00006-2

PNNL. (2022). Energy Storage Cost and Performance Database. https://www.pnnl.gov/ESGC-cost-performance

PNNL, Mongird, K., Fotedar, V., Viswanathan, V., Koritarov, V., Balducci, P., Hadjerioua, B., & Alam, J. (2019). Energy Storage Technology and Cost Characterization Report.

Pramanik, P. K. D., Sinhababu, N., Mukherjee, B., Padmanaban, S., Maity, A., Upadhyaya, B. K., Holm-Nielsen, J. B., & Choudhury, P. (2019). Power Consumption Analysis, Measurement, Management, and Issues: A State-of-the-Art Review of Smartphone Battery and Energy Usage. https://doi.org/10.1109/ACCESS.2019.2958684

PVGIS. (2022). https://re.jrc.ec.europa.eu/pvg_tools/en/

Python. (2021). https://docs.python.org/3/reference/

Revankar, S. T. (2019). Chemical Energy Storage. *Storage and Hybridization of Nuclear Energy: Techno-economic Integration of Renewable and Nuclear Energy*, 177–227. https://doi.org/10.1016/B978-0-12-813975-2.00006-5

Rezk, H., Mukhametzyanov, I. Z., Abdelkareem, M. A., Salameh, T., Sayed, E. T., Maghrabie, H. M., Radwan, A., Wilberforce, T., Elsaid, K., & Olabi, A. (2022). Multi-criteria decision making for

different concentrated solar thermal power technologies. *Sustainable Energy Technologies and Assessments*, *52*, 102118. https://doi.org/10.1016/J.SETA.2022.102118

Rödl & Partner. (2020). Bifacial PV . . . and who is Albedo? https://www.roedl.com/insights/renewable-energy/2019-05/bifacial-pv-and-who-is-albedo

Rodríguez-Gallegos, C. D., Bieri, M., Gandhi, O., Singh, J. P., Reindl, T., & Panda, S. K. (2018). Monofacial vs bifacial Si-based PV modules: Which one is more cost-effective? *Solar Energy*, *176*, 412–438. https://doi.org/10.1016/J.SOLENER.2018.10.012

Romero, M., Gonzalez-Aguilar, J., & Zarza, E. (2015). Concentrating solar thermal power. *Energy efficiency and renewable energy handbook* (pp. 1261–1370). CRC press.

SAM. (2020). System Advisor Model (version 2.29). https://sam.nrel.gov/

Sandia Laboratories. (2015). *Budgeting for Solar PV Plant O&M: Practices & Pricing* (tech. rep.).

Schiel, W., & Keck, T. (2021). Chapter 9 - Parabolic dish concentrating solar power systems. *Concentrating solar power technology* (Second Edition, pp. 311–355). Woodhead Publishing. https://doi.org/https://doi.org/10.1016/B978-0-12-819970-1.00007-4

Schopfer, S., Tiefenbeck, V., & Staake, T. (2018). Economic assessment of photovoltaic battery systems based on household load profiles. https://doi.org/10.1016/j.apenergy.2018.03.185

Shahriar, A., Hasnath, S., & Islam, M. A. (2020). Effects of Operating Temperature on the Performance of c-Si, a-Si:H, CIGS, and CdTe/CdS Based Solar Cells. *EDU Journal of Computer and Electrical Engineering*, *1*(1), 31–37. https://doi.org/10.46603/ejcee.v1i1.21

Sharma, S., Jain, K. K., Sharma, A., et al. (2015). Solar cells: in research and applications—a review. *Materials Sciences and Applications*, *6*(12), 1145.

Smets, A., Jäger, K., Isabella, O., van Swaaij, R., & Zeman, M. (2016). *Solar Energy: The physics and engineering of photovoltaic conversion, technologies and systems*. UIT Cambridge Limited.

Smith, B. L., Woodhouse, M., Horowitz, K. A. W., Silverman, T. J., Zuboy, J., & Margolis, R. M. (2020). *Photovoltaic (PV) Module Technologies: 2020 Benchmark Costs and Technology Evolution Framework Results* (tech. rep.). www.nrel.gov/publications.

Snowden, S. (2020). Double-Sided Solar Panels That Track The Sun Could Produce 35% More Energy. *Forbes*.

Statista. (2020). Average industrial electricity prices in Panama. https://www.statista.com/statistics/1175005/price-industrial-electricity-panama/

Stein, W. H., & Buck, R. (2017). Advanced power cycles for concentrated solar power. *Solar Energy*, *152*, 91–105. https://doi.org/10.1016/J.SOLENER.2017.04.054

Steinmann, W.-D., & Eck, M. (2006). Buffer storage for direct steam generation. *Solar Energy*, *80*(10), 1277–1282. https://doi.org/10.1016/j.solener.2005.05.013

Stine, W. B., & Geyer, M. (2001). 12 - Power Cycles for Electricity Generation. *Power from the Sun*, *1*.

Sun, C., Zhang, H., & Chemsuschem. (2021). Review of the Development of First-Generation Redox Flow Batteries: Iron-Chromium System. *ChemSusChem*, *2022*, 202101798–202101799. https://doi.org/10.1002/cssc.202101798

Sun, W., Hong, Y., & Wang, Y. (2016). Operation Optimization of Steam Accumulators as Thermal Energy Storage and Buffer Units. *Energies*, *10*(1), 17. https://doi.org/10.3390/en10010017

Tapia-Ruiz, N., Armstrong, A. R., Alptekin, H., Amores, M. A., Au, H., Barker, J., Boston, R., Brant, W. R., Brittain, J. M., Chen, Y., Chhowalla, M., Choi, Y. S., Costa, S. I., Ribadeneyra, M. C., Cussen, S. A., Cussen, E. J., David, W. I., Desai, A. V., Dickson, S. A., . . . Younesi, R. (2021). 2021 roadmap for sodium-ion batteries. *Journal of Physics: Energy*, *3*(3), 031503. https://doi.org/10.1088/2515-7655/AC01EF

Taraba, M., Adamec, J., Danko, M., Drgona, P., & Urica, T. (2019). Properties measurement of the thin film solar panels under adverse weather conditions. *Transportation Research Procedia*, 535–540. https://doi.org/https://doi.org/10.1016/j.trpro.2019.07.077

Taslimi, M., Ahmadi, P., Ashjaee, M., & Rosen, M. A. (2021). Design and mixed integer linear programming optimization of a solar/battery based Conex for remote areas and various climate zones. *Sustainable Energy Technologies and Assessments*, *45*, 101104. https://doi.org/10.1016/J.SETA.2021.101104

Taylor, N. G., & Jäger-Waldau, A. (2018). Low Carbon Energy Observatory Photovoltaics Technology Development Report 2018. https://doi.org/10.2760/373667

TNO. (2022). Perovskite-based solar cells. https://www.tno.nl/en/focus-areas/energy-transition/roadmaps/renewable-electricity/solar-energy/pv/perovskite-solar-cells/

Trading Economics. (2022a). 20 million indicators from 196 countries. https://tradingeconomics.com/

Trading Economics. (2022b). Netherlands - Electricity prices: Non-household, medium size consumers - 2022 Data 2023 Forecast 2010-2021 Historical. https://tradingeconomics.com/netherlands/electricity-prices-non-household-medium-size-consumers-eurostat-data.html

Ud-Din Khan, S., Wazeer, I., Almutairi, Z., & Alanazi, M. (2022). Techno-economic analysis of solar photovoltaic powered electrical energy storage (EES) system. *Alexandria Engineering Journal*, *61*(9), 6739–6753. https://doi.org/10.1016/J.AEJ.2021.12.025

Vant-Hull, L. L. (2021). Chapter 8 - Central tower concentrating solar power systems. *Concentrating solar power technology* (Second Edition, pp. 267–310). Woodhead Publishing. https://doi.org/https://doi.org/10.1016/B978-0-12-819970-1.00019-0

Visiongain. (2019). *Concentrated Solar Power (CSP) Market Report 2019-2029* (tech. rep.).

Viswanathan, V., Mongird, K., Franks, R., Li, X., Sprenkle, V., & Baxter, R. (2022). 2022 Grid Energy Storage Technology Cost and Performance Assessment.

Vopak. (2022). *Internal Information, data, presentation*.

Weber, A. Z., Mench, M. M., Meyers, J. P., Ross, P. N., Gostick, J. T., & Liu, Q. (2011). Redox flow batteries: a review. *Journal of Applied Electrochemistry*, *41*(10), 1137–1164. https://doi.org/10.1007/s10800-011-0348-2

Weimar, N. D. (2020). Tilted single Axis Tracker. https://sinovoltaics.com/learning-center/csp/tilted-single-axis-tracker/

Wilson, G. M., Al-Jassim, M., Metzger, W. K., Glunz, S. W., Verlinden, P., Xiong, G., Mansfield, L. M., Stanbery, B. J., Zhu, K., Yan, Y., Berry, J. J., Ptak, A. J., Dimroth, F., Kayes, B. M., Tamboli, A. C., Peibst, R., Catchpole, K., Reese, M. O., Klinga, C. S., . . . Sulas-Kern, D. B. (2020). The 2020 photovoltaic technologies roadmap. https://doi.org/10.1088/1361-6463/ab9c6a

World Bank Group. (2022). Global Solar Atlas. https://globalsolaratlas.info/download/world

World Data. (2021). Average income around the world. https://www.worlddata.info/average-income.php

Wu, F.-B., Yang, B., & Ye, J.-L. (2019). Technologies of energy storage systems. *Grid-scale Energy Storage Systems and Applications*, 17–56. https://doi.org/10.1016/B978-0-12-815292-8.00002-2

Xin, Q. (2013). Optimization techniques in diesel engine system design. *Diesel Engine System Design*, 203–296. https://doi.org/10.1533/9780857090836.1.203

Xu, X., Vignarooban, K., Xu, B., Hsu, K., & Kannan, A. M. (2016). Prospects and problems of concentrating solar power technologies for power generation in the desert regions. *Renewable and Sustainable Energy Reviews*, *53*, 1106–1131. https://doi.org/https://doi.org/10.1016/j.rser.2015.09.015

Xu, Y., Pei, J., Cui, L., Liu, P., & Ma, T. (2022). The Levelized Cost of Storage of Electrochemical Energy Storage Technologies in China. *Frontiers in Energy Research*, *10*. https://doi.org/10.3389/fenrg.2022.873800

Yoon, Y. (2021). How Can We Use Carbon Dioxide to Feed Rechargeable Batteries?

Zeng, Y. K., Zhao, T. S., An, L., Zhou, X. L., & Wei, L. (2015). A comparative study of all-vanadium and iron-chromium redox flow batteries for large-scale energy storage. *Journal of Power Sources*, *300*, 438–443. https://doi.org/10.1016/j.jpowsour.2015.09.100

Zeng, Y. K., Zhou, X. L., An, L., Wei, L., & Zhao, T. S. (2016). A high-performance flow-field structured iron-chromium redox flow battery. *Journal of Power Sources*, *324*, 738–744. https://doi.org/10.1016/j.jpowsour.2016.05.138

Zhu, G. (2017). New adaptive method to optimize the secondary reflector of linear Fresnel collectors. *Solar Energy*, *144*, 117–126. https://doi.org/10.1016/J.SOLENER.2017.01.005

Zimmerman, A. (2009). *Nickel-Hydrogen Batteries: Principles and Practice*. American Institute of Aeronautics; Astronautics, Inc. https://doi.org/10.2514/4.989209